Solid Fuel Blend Pyrolysis-Combustion Behavior and Fluidized Bed Hydrodynamics

Gaurav Agarwal

Dissertation submitted
to the faculty of the Virginia Polytechnic Institute and State University
in partial fulfillment of the requirements for the degree of

Doctor of Philosophy

in

Mechanical Engineering

Brian Lattimer

Srinath Ekkad

Uri Vandsburger

Francine Battaglia

Gerald Luttrell

September 25, 2013

Blacksburg, VA

Keywords: Decomposition modeling; Coal-biomass co-pyrolysis; Coal-biomass co-combustion; Fuel blend performance; Fluidization hydrodynamics; Solid circulation

Solid Fuel Blend Pyrolysis-Combustion Behavior and Fluidized Bed Hydrodynamics

Gaurav Agarwal

ABSTRACT

As a carbon neutral and renewable source of energy, biomass carries a high potential to help sustain the future energy demand. The co-firing of coal and biomass mixtures is an alternative fuel route for the existing coal based reactors. The main challenges associated with co-firing involves proper understanding of the co-firing behavior of blended coal-biomass fuels, and proper understanding of advanced gasification systems used for converting such blended fuels to energy.

The pyrolysis and combustion behavior of coal-biomass mixtures was quantified by devising laboratory experiments and mathematical models. The pyrolysis-combustion behavior of blended fuels was quantified on the basis of their physicochemical, kinetic, energetic and evolved gas behavior during pyrolysis/combustion. The energetic behavior of fuels was quantified by applying mathematical models onto the experimental data to obtain heat of pyrolysis and heat of combustion. Fuel performance models were developed to compare the pyrolysis and combustion performance of non-blended and blended fuels. The effect of blended fuel briquetting was also analyzed to find solutions related to coal and biomass co-firing by developing a bench scale fuel combustion setup. The collected data was analyzed to identify the effects of fuel blending and briquetting on fuel combustion performance, ignitability, flammability and evolved pollutant gases.

A further effort was made in this research to develop the understanding of fluidized bed hydrodynamics. A lab scale cold-flow fluidized bed setup was developed and novel non-intrusive techniques were applied to quantify the hydrodynamics behavior. Particle Image Velocimetry and Digital Image Analysis algorithms were used to investigate the evolution of multiple inlet gas jets located at its distributor base. Results were used to develop a comprehensive grid-zone phenomenological model and determine hydrodynamics parameters such as jet particle entrainment velocities and void fraction among others. The results were further used to study the effect of fluidization velocity, particle diameter, particle density, distributor orifice diameter and orifice pitch on the solid circulation in fluidized beds.

Table of Contents

LIST OF FIGURES

LIST OF TABLES

1. OVERVIEW

Questions about the long-term availability of traditional fossil fuels, their geopolitical availability, and the tightening environmental restrictions have resuscitated the need to explore renewable and clean sources of energy to alleviate the concerns of ever increasing energy demand. Biomass is regarded as a carbon neutral and renewable source of energy, and carries high potential for sustainable development in the future [1]. Biomass feedstocks can be converted to source of liquid (bio-oil), gaseous (bio-gas) and solid (bio-char) form of fuels. The versatility of the forms of energy generated from biomass conversion, through the use of various technologies, makes it a strong candidate for satisfying the energy needs for diverse applications and industries. Conversion of biomass feedstock to gaseous, liquid and solid-char forms also solves the issues related to storage, transportation and feedstock rotting.

Biomass represents a carbon neutral source of energy because the amount of carbon dioxide produced during the combustion of such fuels is absorbed during the photosynthesis process of the involved plants, like energy crops [2-6]. Thus, biomass-based energy can significantly contribute to the fulfillment of objectives of Kyoto agreement and other international treaties towards reducing the green house gas emissions [2, 6, 7].

Biomass feedstocks include agricultural and other lignocellulosic (e.g., forestry) waste, waste oils, algae, energy crops, byproducts of other bio-based industries (e.g., glycerol from biodiesel), and other organic wastes [1, 3, 8]. The availability of such resources in all countries opens up the opportunities for simultaneous development of agriculture and bio-energy industries, especially in developing agriculture based economies. The presence of exclusive, different and multiple resources of such feedstocks in a region pose a challenge to develop technologies that can handle versatile fuels. According to a recent study, only about 40% of the potential biomass energy is utilized in the world [6]. The global biomass potential is estimated to be between 33-1135 EJ/year for the years 1990-2060 [9, 10], with the current global energy demand being 470 EJ/year. It has been established that in the US alone, the amount of biomass that can be harvested without much changes in land use is equivalent to the energy content of 3.8 billion barrels of oil per year, with US consumption being 7 billion barrels/year [6, 11, 12]. Hence, proper knowledge and investigation of feedstock to fuel conversion processes is necessary to exploit the full potential of the biomass resource.

With biomass currently providing 14% of world's total energy production [1], much of its potential amount is wasted by inefficient technologies [1, 5, 11]. To exploit the full potential of biomass energy, modern technologies and an improved understanding of biomass conversion process to bio-fuels must be developed. For this reason, a systematic methodology should be developed for the complete understanding of different biomass fuels undergoing fuel conversion processes. Based on its characterization, optimal coal-biomass mixture feedstocks can be prepared for operation with current coal based reactors/gasifiers to provide an alternative, renewable and clean source of energy with relatively low capital investments.

The sections below briefly discuss different biomass fuel sources, the fuel conversion processes, fuel conversion technologies, possibilities of biomass co-pyrolysis with coal, and some challenges associated with these issues.

1.1 Biomass composition

Feedstocks for existing gasifier/reactor plants primarily include coal, biomass, and their mixtures [13]. Present technologies have the capability to harness energy from any type of coal, although the expensive lower ash content coals are preferred from performance, environmental and operational point of view.

The performance of existing gasification technologies is sensitive to the coal properties used for its operation. Further inclusion of biomass in their operation requires extensive knowledge about the properties, structure, composition and thermal behavior of such fuels. Biomass feedstocks have high volatile matter and are reactive at lower temperatures than coals. Biomass particles are less dense and carry much higher aspect ratios than coal particles. From the Van Krevelen diagram shown in **Figure 1**, it can be seen that the chemical composition of biomass is substantially different than coal, and unlike coal this composition varies widely among different sources of biomass feedstocks [5, 14, 15]. Biomass feedstocks contain higher hydrogen and oxygen content, which is consistent with higher volatile matter and moisture contents in comparison to the coal samples. The nitrogen and sulfur content are generally low [16], thereby abating the NOx and SOx emissions. Apart from these, biomass feedstocks contain a significant amount of alkali compounds in their raw form, which affect the kinetics of pyrolysis reactions and the operation of gasifiers [6, 17-20].

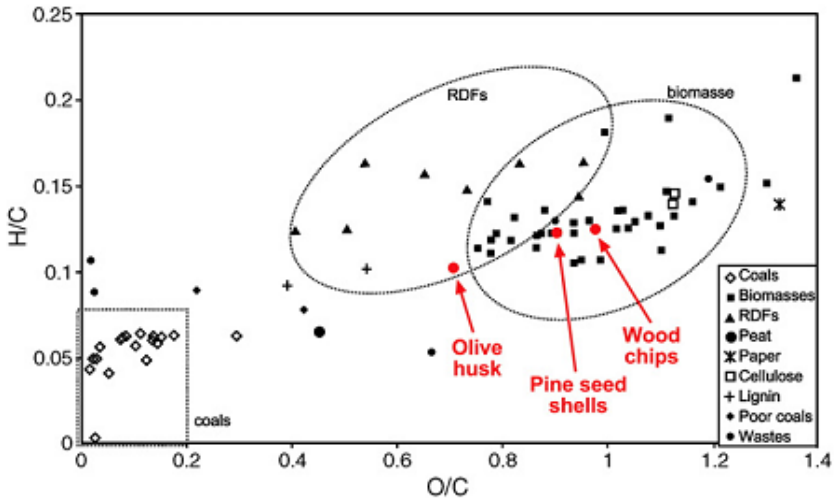

Figure 1: Van Krevelen diagram for different fuels. [5]

Despite the wide variability of the elemental composition with its various feedstocks, biomass as a lignocellulosic material mainly consists of three major constituents, cellulose (30-60%), hemicellulose (20-35%) and lignin (15-30%) [1, 6]. The pyrolysis of biomass yields additive evolved gas patterns, deliver additive kinetics, and display additive thermo-gravimetric behavior as those from the additive weight based ratio of biomass constituents. The deviations found, if any, are reported due to the presence of inorganic salts causing catalysis of the primary reactions [2, 19, 21-35]. Similarly, coal-biomass mixtures demonstrated additive gravimetric behavior of the ratio of individual coal and biomass samples [19, 36-47], while the additive behavior on the energetic aspect has not been verified. Hence, the complete understanding of individual biomass constituents is imperative to the successful prediction of pyrolysis behavior of biomass and coal-biomass blends.

Cellulose, $(C_6H_{12}O_5)_n$, is the main component of plant cell walls and is a linear polymer of D-glucose with β-1,4 linkages. Hemicellulose (polysaccharides) is a branched polymer of five and six carbon sugars, and binds the cellulose microfibrils of the cell walls. Together, cellulose and hemicelluloses content of biomass is termed as holocellulose, and they decompose in a similar way with dehydration at low temperatures and de-polymerization at higher temperatures. Lignin is the strengthening component of the plant cell wall and is a randomly constructed polymer of methoxy or hydroxyl substituted propyl phenol units [1, 6]. Hemicellulose is least thermally stable component, followed by cellulose and then lignin. Lignin is responsible for higher fraction of char and aromatic products formed during pyrolysis. The study of pyrolysis

characteristics of these constituents is necessary to achieve higher yields of desired products and predict secondary reactions.

1.2 Bio-fuel conversion processes

The two main methods for converting biomass feedstock to bio-fuels are biochemical conversion and thermochemical conversion.

Biochemical processes convert the solid fuel to liquid or gaseous fuels through the enzymatic activity of microorganisms. The two main methods of biochemical conversion include fermentation of starch and cellulose matter, and anaerobic digestion of lignocellulosic biomass by bacteria. While the fermentation process produces liquid fuel (ethanol), the anaerobic digestion leads to the production of biogas (mainly methane) [3, 6]. Further discussion on biochemical process is conducted elsewhere [3].

The main methods for achieving the thermochemical conversion of biomass include combustion, pyrolysis, gasification and torrefaction. As shown in **Figure 2** and **Figure 3**, based on the desired end product and other requirements, one of these methods can be used to produce solid, liquid or gaseous fuels. These methods are briefly discussed below.

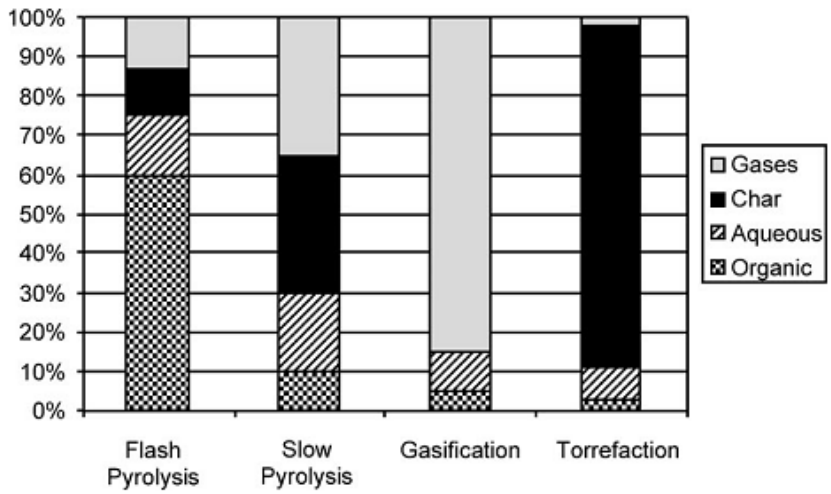

Figure 2: End-product composition from different thermochemical treatment methods [3]

1.2.1 Combustion

Direct combustion of biomass is the most widely practiced thermochemical process. The end product of biomass combustion is heat which must be immediately used for generating electricity or combined heat and power operations (CHP), as shown in **Figure 3** [7].

However, the overall efficiency of heat generation from combustion is typically very low with 15% for small plants to up to 30% for larger and new plants. Moreover, the technology is more restricted for the usage of biomass due to the fuel's low heating value, flame instability due to high reactivity, operational problems from presence of inorganic salts (fouling, slagging, and corrosion), environmental, and economic problems [2, 7, 48].

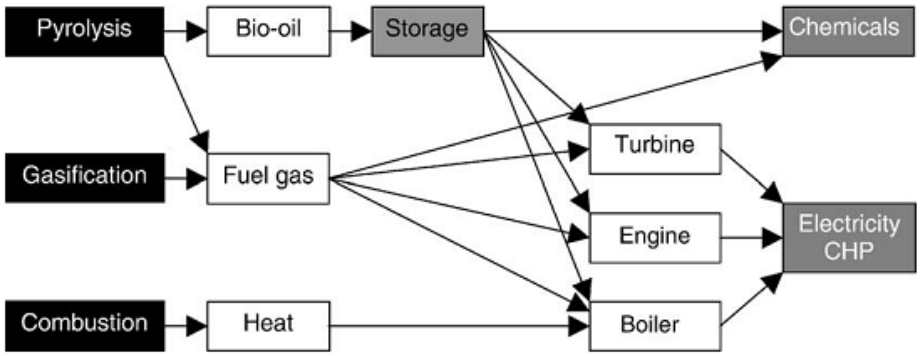

Figure 3: Products from biomass thermochemical conversion and their applications [7]

1.2.2 Pyrolysis

Pyrolysis is the thermal decomposition of complex organic substances into smaller molecules in complete absence of air/oxygen. Pyrolysis is the primary step in combustion and gasification processes. The advantages of pyrolysis over combustion include the usage of low heating value biomass feedstocks, and converting them into liquid or gaseous transportation worthy fuels. The remaining solid char can be further used to generate heat for the plant operation.

The proportion of products formed is dependent on feedstock, reaction temperature regime, residence time, heat transfer rate and other factors [1, 3]. Low process temperature and high residence time promote the formation of char, while high process temperature and high residence time promote formation of gas. Moderate temperature and short residence time favors the production of bio-oils, and thus requires higher heating rates [1, 7]. Cracking of liquid bio-oil

retains specific high quality chemicals, whereas the efficient combustion of bio-oil or bio-gas can lead to the generation of heat or power [3, 6, 7].

As shown in **Figure 2**, flash (fast) pyrolysis is used to produce large quantities of bio-oils and is workable for any kind of biomass. Flash pyrolysis must be completed within a matter of seconds at a medium temperature (508°C) [3]. Exposing the biomass to lower temperatures favor the formation of char, thus signifying the role of reaction kinetics and heat transfer. One of the methods to achieve this goal is to use small particles in fluidized beds because of its high heat transfer rates (600-700 W/m^2K) in comparison to a static bed (~10 W/m^2K), or fixed bed with forced circulation (50-100 W/m^2-K) [1].

1.2.3 Gasification

The pyrolysis of biomass is selectively followed by gasification through total or partial oxidation of primary products (volatiles and char). The treatment temperature for gasification is higher than pyrolysis (750°C in comparison to 500°C for fast pyrolysis), with extra heat coming from the partial combustion of biomass [3].

The gasification process yields more than 80% of gas in its products, which can either be converted to syngas ($CO + H_2$) through further water-shift secondary reaction, or can be directly used as a fuel for CHP cycles [3]. Gas quality obtained from gasification is usually poor with the particular presence of tar as the most significant problem for its direct usage in turbines [7]. However, significant progress has been made in this regard for removal of tar by thermal or catalytic cracking [7, 49].

1.2.4 Torrefaction

Torrefaction is the pyrolysis process of biomass feedstock at lower temperature (200-320°C) and high residence time. As shown in **Figure 2**, the primary final product of torrefaction process is char (torrefied biomass). Torrefied char is a higher quality solid fuel than the original feedstock, and can be further used for combustion or gasification purposes. The char formed from the torrefaction process is resilient to natural biological rotting (unlike original biomass feedstock) and can be further processed into dense briquettes or pellets which are easier to store and transport.

1.3 Pyrolysis and Gasification Technologies

This section briefly discusses the important pyrolysis technologies widely used and researched around the world. Based on their flow geometries, operating regimes, types of fuels used and other parameters, there are three main technology variants; namely, moving bed, entrained flow, and fluidized bed technologies.

1.3.1 Moving bed

In moving bed gasifiers, the gases (air + steam) flow slowly in the upward direction. The fuel feed is pushed upward along the gases (co-current) or downward in opposite direction to the gas flow (counter-current), as shown in **Figure 4**. Both technologies are only suitable for solid fuels (coal or biomass or both 5-80 mm size particles). It has also been claimed that coals with as high as 35% ash percent can be processed using this technology [13].

Both technologies have been implemented in the industries and suffer from the problem of tar removal, but the counter-current technology is less favorable than co-current technology [13]. This is partially due to the fact that the upper capacity of a single unit counter-current flow gasifier is limited to 2.5 MWe, thus requiring multiple units for economic viability [7].

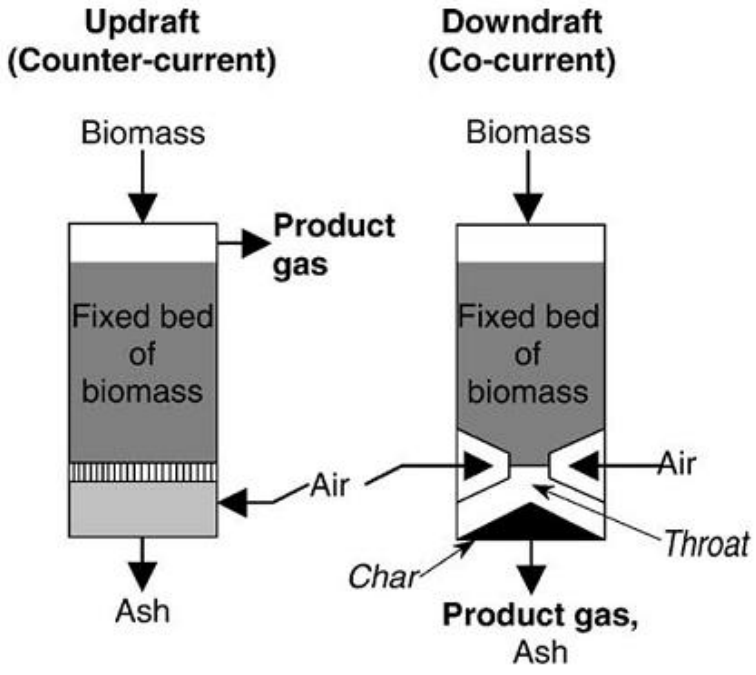

Figure 4: Counter current and Co-current fixed bed gasifiers [7]

1.3.2 Entrained flow

In entrained flow gasifiers, the gases (air/oxygen + steam) move co-currently at high speed along with solid or liquid fuel at high temperature (1200-1800°C) and high pressure (2-8 MPa). Entrained flow gasifiers are most commonly used for coal gasification, which can be injected as dry feed (with carrier gas) or wet feed (water slurry) in pulverized form. Low ash coals are preferred because of the decrease in gas efficiency and increase in slag production for high ash coals. However, there is also a requirement of minimum ash content in order to minimize the heat loss from walls due to its automatic slag coating [13].

The operation of entrained flow gasifiers at high temperatures ensures high carbon conversion. The resultant syngas is thus free of tars and relatively cleaner than gas obtained by fixed beds. However, there are issues related with the high temperature operation. These include requirement of significant gas cooling from sophisticated heat exchangers to below ash softening temperatures, and usage of expensive refractory materials. The operation of entrained flow gasifiers at high temperature and high pressure also shortens the life-cycle of critical components, such as refractory, to below the minimum requirement of 2-3 years [13].

1.3.3 Fluidized bed

In fluidized bed gasifiers, the fuel particles are suspended in the gas flow and undergo mixing while gasification. The turbulent fuel-gas mixture acts as a fluid and increased gas-solid contact enhances the rates of heat transfer, mass transfer and reaction processes. Fluidized bed gasifiers have been proven reliable with a variety of feedstocks, including coal, biomass, and mixtures [7], but only reactive coals such as lignite or brown coals are preferred due to the lower operating temperatures of the gasifier [13]. Fluidized beds are more appropriate for synthesis of bio-oil from flash pyrolysis due to short residence times, high heat transfer and fast separation of vapor and char [1].

As shown in **Figure 5**, there are two main types of fluidized bed reactors, namely the bubbling bed and the circulating bed reactors. In circulating beds, fine particles generated by the reactor are collected and fed back into the fluidized bed system. Although this results in higher carbon conversion ratio and higher efficiencies, it also associates with operational challenges and complex hydrodynamics [7]. The low carbon conversion in bubbling beds can be solved by an addition of char combustor [13]. For biomass feedstock, the proven power capacity for

circulating beds is up to 100 MWhr in comparison to 25 MWhr for bubbling beds. The bubbling bed reactors are of lower capacity due to their requirement of larger bed diameters in comparison to circulating beds [7].

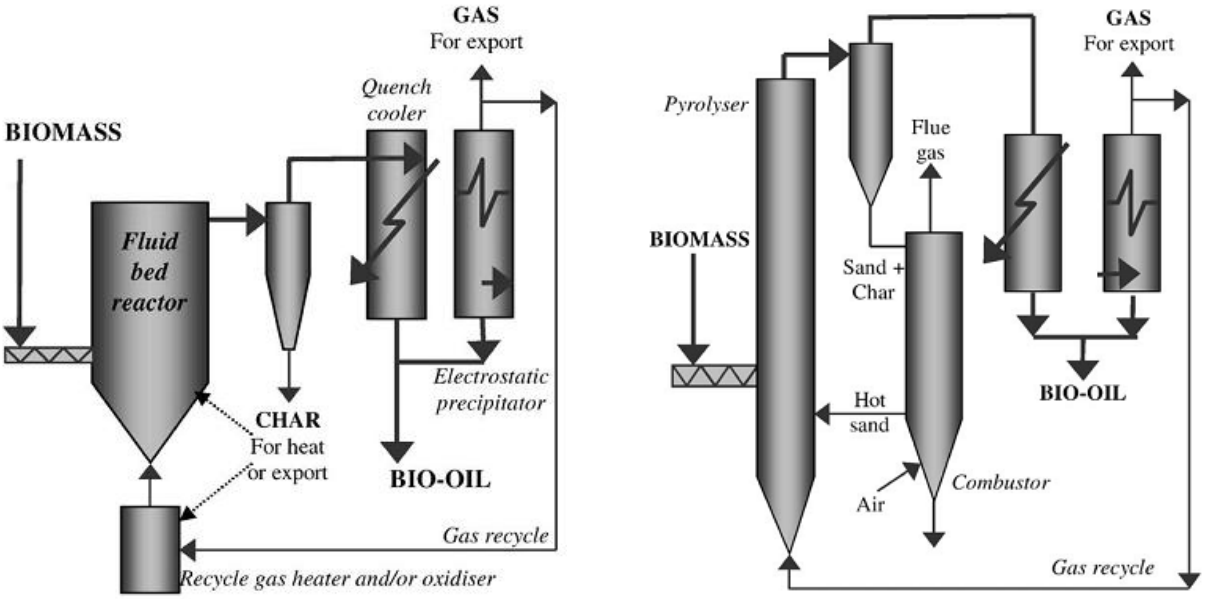

Figure 5: Fluidized bed reactors (a) Bubbling (b) Circulating [7]

As shown in **Figure 6**, a recent study has shown preferable market attractiveness to circulating and bubbling fluidized bed gasifiers in comparison to other technologies, for the conversion of biomass feedstocks [7, 50]. From technological point of view, fluidized bed have advantage over fixed bed and entrained flow for a variety of reasons. Fluidized beds are preferred over entrained flow gasifiers because of the better understanding of reactor dynamics (mature technology) and its mild operating conditions leading to economical and simpler designs. In comparison to lower heat transfer rates in fixed beds (50-100 W/m^2K), the fluidized bed reactors have high heat transfer rates (600-700 W/m^2K). This consequently allows the production of bio-oil from flash pyrolysis [1]. Thus, the fluidized bed technology is considered as prime technology for converting biomass to bio-oil or bio-char [7, 50].

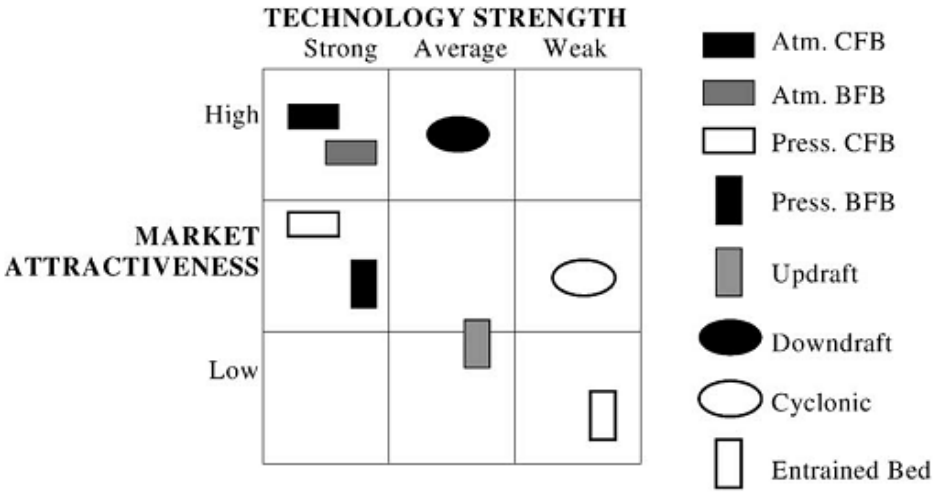

Figure 6: Comparison of biomass gasification technologies [7]

1.4 Biomass-coal co-firing and future prospects

The co-firing of coal and biomass mixture samples is an alternative fuel route for the existing coal based reactors. Biomass can be introduced in its raw, bio-char, bio-oil or bio-gas form, which improves the economics and performance of gasifiers/reactors. It has been shown that besides having a positive impact on the reduction of SOx and NOx pollutants, the co-firing also helps in reducing the emissions of greenhouse gases [5]. The detailed discussion on biomass-coal co-firing in reactors, the advantages, and issues associated are reported elsewhere [51-55]. Energetics, kinetics, and evolved gas analysis of coal-biomass co-pyrolysis will be discussed later in the respective sections.

Recently, the focus has been shifted to the development of tools to predict the behavior of reactors/gasifiers to support the coal-biomass gasification process based on the new Integrated Gasification Combined Cycle (IGCC). **Figure 7** shows the block diagram of a coal based IGCC power plant [13]. IGCC power plants are designed to be highly efficient and environmentally compatible generators of heat and electricity. In fact, the emissions from IGCC plants are well below the requirements from current environmental standards [13]. IGCC plants are primarily developed for clean-coal gasification and power generation. However, biomass can either be fed alongside coal as a supplement fuel, or the product gas from separate biomass gasification can be used to produce heat and electricity for a Biomass-fired IGCC (BIGCC) [6]. IGCC cycles provide an opportunity to effectively remove the SOx and NOx emissions by removing the

contaminants from syngas [56-58]. IGCC cycles also open up the scope of technology improvement in syngas based gas turbines, which have the potential to achieve higher efficiencies [6].

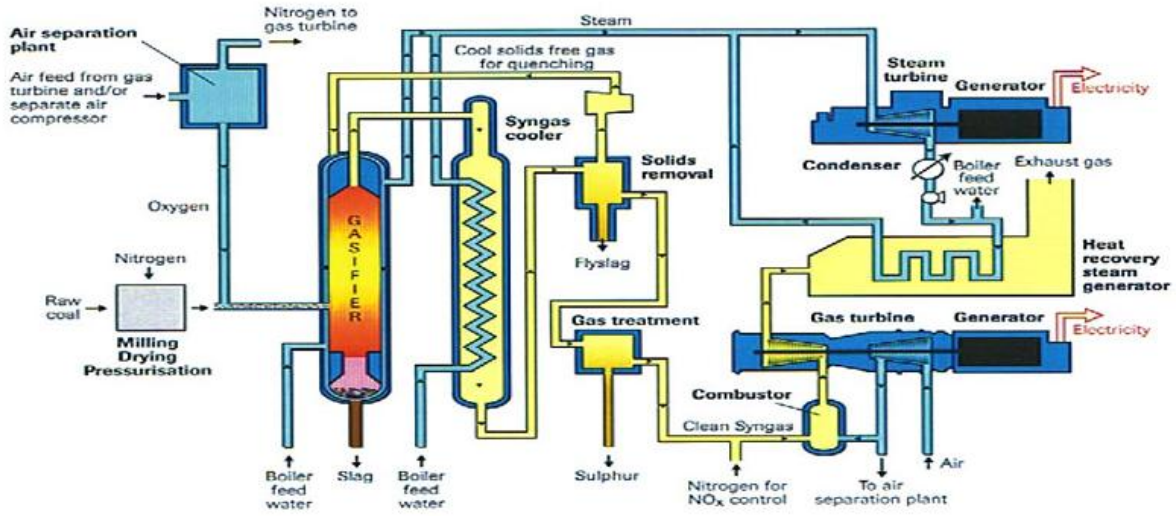

Figure 7: Key components of IGCC cycle [13]

As shown in **Figure 7**, gasification is the key element of the IGCC cycle. However, scaling up of laboratory based gasifiers has historically created reliability issues with the pilot-scale gasifiers. Hence, more research is needed to understand the complex hydrodynamics, heat transfer and reaction processes occurring inside a gasifier. Further research is also required to develop efficient and advanced gas turbines capable of working together with the syngas generated from the gasification plants.

1.5 Closure

The advantages of using biomass along with fluidized bed reactors gives plenty of incentives to multiply the research interest in the technology. The major advantage of using biomass is that any kind of feedstock, including agricultural wastes, forest residues, byproducts of food industry and bio-refineries, or organic municipal wastes can be converted into clean and renewable source of energy by thermochemical processes. The higher reactivity of biomass fuel, in comparison to coal, results in pyrolysis occurring at lower temperatures which leads to reduced extents of heat loss, emissions and operation problems. However, as discussed in previous sections more

research is needed to understand the biomass and coal-biomass co-pyrolysis and co-combustion behavior.

As the key component of IGCC plants, the gasifier plays a major role in enhancing the performance and reducing emissions from coal-biomass gasification. Hence, an effort is also needed to understand the hydrodynamics, heat transfer and reaction processes occurring during the pyrolysis process. This will eventually lead to better prospects for biomass gasification to penetrate in the current and future energy markets.

2. RESEARCH FOCUS

Significant efforts have been directed in the literature towards realizing coal-biomass co-firing from the existing scaled-up plants [13, 59]. However, performing coal-biomass co-firing on a coal-based reactor still remains a challenging task in terms of predicting and improving the reactor performance. This is primarily due to the intricate pyrolysis-combustion behavior of fuel mixtures and the changes in the reactor thermo-hydrodynamics due to the introduction of such diverse fuels. In the current study, the pyrolysis and combustion behavior of such coal-biomass fuel blends was quantified by laboratory scale experiments to better predict and improve scaled-up reactor performance.

An organized methodology is required to qualitatively and quantitatively understand the pyrolysis and combustion behavior of coal-biomass fuel blends. There are certain aspects in which the behavior of such fuels undergoing pyrolysis-combustion can be quantified. In the current research, it was identified that to better predict the blend performance in a reactor, the blend pyrolysis-combustion behavior must be understood in terms of its physicochemical changes, kinetic parameters, evolved gas aspects and associated pyrolysis-combustion energetics. Based on these main aspects of analysis, a fuel pyrolysis and combustion performance model must be developed to compare the performance of different fuel blends.

Figure 8 shows the proposed roadmap for a project undertaken for predicting and improving the performance of a scaled-up reactor. In the current project, the coal-biomass blend behavior was understood in terms of it physicochemical, kinetics, energetics and evolved gas behavior while undergoing pyrolysis-combustion. Based upon this understanding, fuel performance parameters were developed to compare the pyrolysis and combustion performance of blends versus non-blended (constituent) fuels. The fuel pyrolysis-combustion behavior analysis in these aspects would further the understanding of a lab scale reactor setup. The performance of different fuels and blends can then be verified on such a lab scale reactor.

Along with understanding and predicting the behavior of fuel blends, the effort must also be put into improving the pyrolysis-combustion performance of such fuel blends. In this respect, usage of briquettes instead of pulverized fuels is attractive because briquettes not only increase the density of the fuel allowing for a higher energy content fuel to be delivered to the reactor, but also improves the fuel handling, storage, fuel injection and issues related to fuel degradation over time. In this research, coal-biomass blended fuel briquettes were analyzed for their combustion

performance and pollutant emission gas yields. This performance of blended fuel briquettes was then compared to those of pulverized coal-biomass fuel blends to suggest improvements in the operation of a lab-scale reactor.

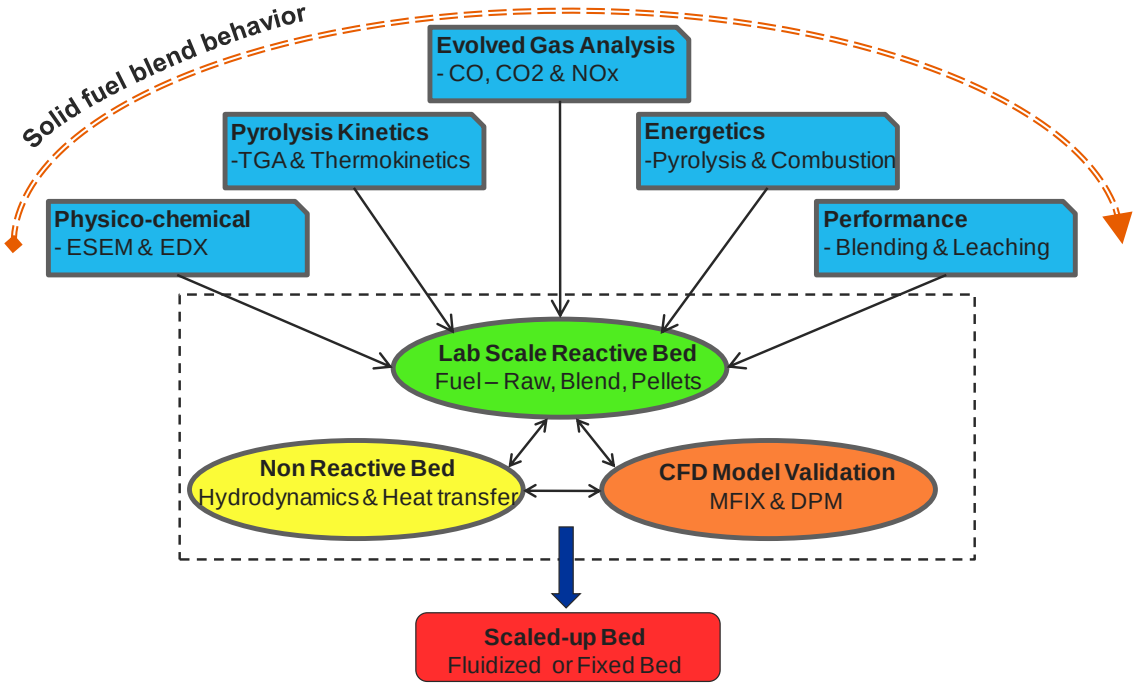

Figure 8: Project roadmap

To properly predict and improve the performance of a scaled-up reactor, the understanding of fuel blend performance behavior from a lab scale reactive setup alone is not sufficient. As shown in **Figure 8**, such a comprehensive study must also be tackled from two more aspects. Firstly, it is important to understand the thermo-hydrodynamics of a lab scale reactor. This analysis should be performed to better understand the mixing behavior of fuel particles inside an advanced gasification unit. The optimal conditions must then be determined for high particle circulation and heat transfer to better extract the combustion performance from fuel blends. Secondly, it is important to develop and validate detailed numerical models to predict reactor thermo-hydrodynamics and kinetics of lab scale setups. These tools in the future will help us to better predict and improve the performance of scale-up plant.

In the current study, some aspects of these last two mentioned points were analyzed. The hydrodynamics of an advanced gasification unit, namely fluidized bed, was quantified by developing a cold-flow lab scale fluidized bed setup. The cold flow setups are essential in determining the behavior of scaled-up reactors because the heat transfer and hydrodynamics measurements can be made in the absence of interference from chemical reactions. A range of preferred operating conditions of a fluidized bed setup were determined to obtain high solid circulation with lower power input into the bed.

In particular, a proper understanding of the grid-zone region of the fluidized bed was developed. The grid-zone region is the zone in the fluidized bed where gases interact with the reacting fuel, in-turn providing high chemical reaction rates. The experimental data collected from fluidized bed was provided to numerical simulation groups at Virginia Tech for further development and validation of comprehensive numerical models.

The tasks completed in the current study for predicting and improving the blend performance in reactors were undertaken in the following chronological order:

i. Development of lab-scale cold-flow advanced gasification system, namely fluidized bed. Grid zone behavior model development and solid circulation calculation.
ii. Physicochemical behavior quantification for pulverized fuel blends and determining blend char interaction during co-pyrolysis.
iii. Kinetic model development for fuel blend pyrolysis and Arrhenius parameter calculation.
iv. Pyrolysis and combustion energetics model development for fuels. Validation of energetics models and prediction of energetic parameters (heat of pyrolysis, heat of gasification and heat of combustion) for fuel blends from blend constituent data.
v. Development of fuel pyrolysis and combustion performance models. Comparison of performance of fuel blends with constituent fuels.
vi. Development of a lab scale combustion setup to compare the combustion performance of briquetted fuel blends and pulverized fuel blends. Suggestions for improvements in reactor operating conditions for high combustion performance and lower pollutant gas emissions.

3. FLUIDIZED BED HYDRODYNAMICS[1,2]

3.1 Literature review

Fluidized beds commonly consist of multiple jets of oxygen containing gas located at the bottom of the bed. The region above the distributor base and below the jet height is known as the grid-zone. The jets are used to fluidize particulate media as well as support the combustion and gasification of solid fuel in grid-zone. The importance of these jets is reflected by their ability to act as a reacting medium and to control the reactors that produce syngas from gasification of fuels such as coal and biomass. These jets entrain gas and particles from the emulsion thereby enhancing the gas-particle mixing. Thus, the entrainment process helps to promote heat transfer, mass transfer and chemical reaction rates for a fluidized bed reactor. For proper performance estimation, the patterns and extent of gas-particle mixing must be determined for a reactor. Failure to predict these factors may lead to problems such as particle agglomeration, temperature hot spots and partial de-fluidization.

Various mathematical and empirical models for particle entrainment rate have been suggested in the literature. In the research conducted by Thorley *et al*. [60], the forces acting on particles in the jet spout were balanced to estimate the particle velocity profile. Lefroy [61] suggested an alternative approach to predict the solid circulation rate by solving mass and momentum equations for bed voidage and particle velocities in the jet spout. This approach was further supplemented by various works in the literature [62-66]. Van Deemter [67] developed the counter-current flow model for gas-solid fluidized beds to propose the bubble induced particle mixing and solid circulation. This was further extended by Baeyens *et al*. [68] and van Deemter [69] into comprehensive models and empirical equations to estimate the model parameters, particle velocities, circulation flux, bed turnover time, gas back mixing, residence time,

[1] A significant part of this chapter is published in *Influence of multiple gas inlet jets on fluidized bed hydrodynamics using Particle Image Velocimetry and Digital Image Analysis*, Gaurav Agarwal, Brian Lattimer, Srinath Ekkad, Uri Vandsburger, *Powder Technology*, Volume 214, Issue 1, November 2011, Pages 122-134, *Used with permission of Elsevier, 2013*

[2] A significant part of this chapter is published in *Experimental Study on Solid Circulation in a Multiple Jet Fluidized Bed*, Gaurav Agarwal, Brian Lattimer, Srinath Ekkad, Uri Vandsburger, *AICHE Journal*, Volume 58, Issue 10, December 2011, Pages 3003-3015, *Used with permission of John Wiley & Sons, 2013*

segregation and defluidization. Merry [70] developed a particle entrainment model based on particle stream function and validated it experimentally using a liquid-solid fluidized bed. Donsi *et al*. [71] developed a mathematical model based on the turbulent jet theory [72] to describe the observed jet characteristics in a two-dimensional bed. This was further extended by Massimilla [73] to a more detailed model which included mode of discharge, jetting regions, penetration depths, expansion angle, entrainment, bubble size and transport models.

Various experimental studies have been performed to provide the empirical input parameters for these mathematical models, as well as to provide data for model validation [62, 74, 75]. The most important parameters to quantify the particle entrainment rate are particle velocities, void fraction values, jet diameter and jet penetration length. Several intrusive and non intrusive techniques have been applied to quantify one or more of these parameters in experimental fluidized beds setups [60, 63, 70, 71, 76-100]. Most of these experimental studies have been conducted using single jet spouted beds. Also, reports on the influence of multiple jet systems on solid circulation are still sparse in the literature.

The motivation behind this study was to understand the effect of distributor orifice diameter, orifice pitch, particle types and operating conditions on the solid circulation dynamics of a multiple jet system fluidized bed. PIV and DIA have recently been used on a single jet system to analyze the solid circulation behavior [99]. However, its application onto multiple jet systems has not been reported in the literature. In this study, a two-dimensional bed was used to analyze the solid circulation phenomena, including jet entrainment, on a multiple jet system. Published works on this aspect of the research are found in reference [101] and [102].

3.2 Experimental setup

A complete description of the experimental setup, test cases involved and analysis procedure is given in reference [101] and [102]. A brief discussion of these topics is given below.

Figure 9 contains a schematic of the two-dimensional fluidized bed setup used to investigate the grid-zone dynamics. The bed was 0.76 m high and 0.25 m wide with a depth of 12.7 mm. The bed walls were made of high optical clarity glass. The bed was illuminated homogeneously using two halogen lamps of 500 W each. A Flowsense MKII (4 Megapixel) PIV camera was used to take double frame digital images of the bed. Air supply was controlled through a 500 SLPM ALICAT mass flow. The air was channeled through a humidifier in order

to avoid electrostatic effects in the bed. Air was then fed into the plenum chamber and injected into the bed through a perforated plate distributor.

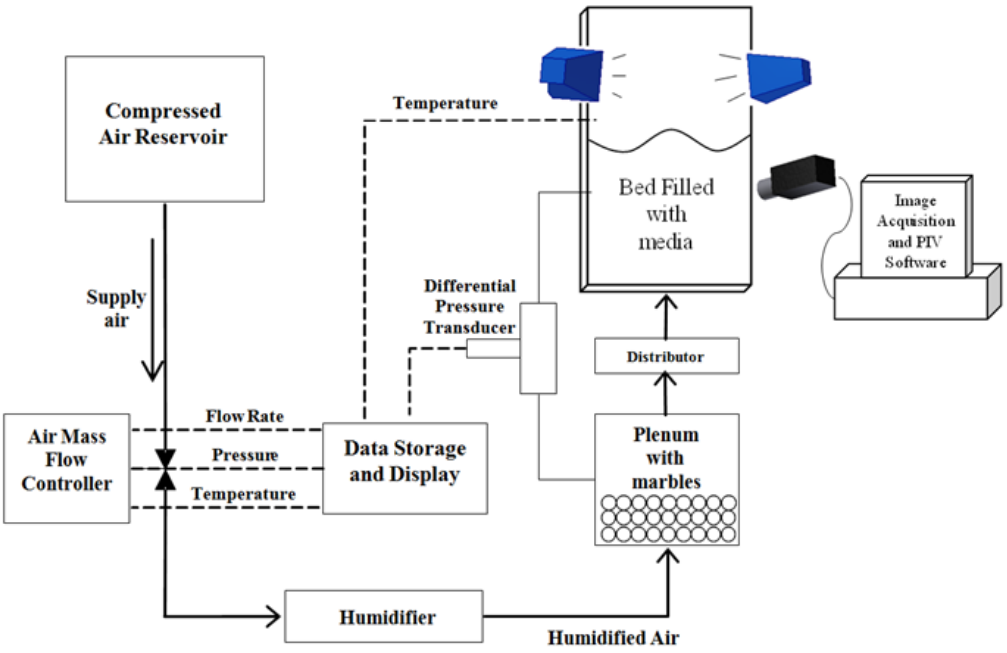

Figure 9: Schematic of experimental setup

3.2.1 Test cases

Three types of particles were selected to provide a diameter range of 550 µm to 750 µm and density range of 1079 kg/m^3 to 2500 kg/m^3. As listed in **Table 1**, this resulted in particles with Geldart B and D classification. Each type of particle was examined using five different types of perforated distributor plates. As listed in **Table 2**, effects of orifice diameter and orifice pitch were evaluated in this study. The solid circulation analysis was conducted for A1, A2 and B1 distributor plates, while jet length and jet diameter analysis was conducted for all five distributor plates.

Table 1: Physical properties of tested fluidized bed media

Particle	d_p (µm)	ρ_p (kg/m^3)	U_{mf} (m/s)	Geldart Group
Glass	550	2500	0.22	B
Glass	750	2500	0.35	D
Ceramic	550	1079	0.20	B

Table 2: Description of perforated distributor plates

Distributor Type	d_o (mm)	N (Number of Holes)	P (m)
A1	2	9	0.028
A2	2	5	0.056
A3	2	3	0.084
B1	3	4	0.063
B2	3	2	0.127

3.2.2 Pressure drop analysis

The differential pressure drop was analyzed to calculate the minimum fluidization velocity ($U_{mf,2D}$) for each combination of particle type and distributor type in the two-dimensional bed. These velocities are listed in **Table 3** and compared with minimum fluidization velocities ($U_{mf,3D}$) calculated for respective particles in a cylindrical fluidized bed setup [103].

Table 3: Comparison of experimental minimum fluidization velocities measured for cylindrical and two-dimensional bed test runs. Term in bracket indicates $U_{mf,2D}/U_{mf,3D}$ for the corresponding particle type.

Distributor Type	Glass 550 µm particles (m/s)	Glass 750 µm particles (m/s)	Ceramic 550 µm particles (m/s)
3D Bed [a]	0.22	0.35	0.20
A1 [b]	0.23 [1.0]	0.34 [1.0]	0.23 [1.1]
A2 [b]	0.21 [0.9]	0.28 [0.8]	0.17 [0.9]
A3 [b]	0.16 [0.7]	0.16 [0.5]	0.13 [0.7]
B1 [b]	0.23 [1.0]	0.34 [1.0]	0.18 [0.9]
B2 [b]	0.16 [0.7]	0.23 [0.7]	0.15 [0.8]

[a] $U_{mf,3D}$ (m/s), [b] $U_{mf,2D}$ (m/s)

3.2.3 PIV

PIV is a non-intrusive optical technique used to quantify velocity field information of seeding particles suspended in a fluid through measurement of particle displacement over a known time interval. Due to dense media prohibiting laser passage in the bed, a conventional PIV technique cannot be used to obtain gas or particle velocities. However, PIV can be used to quantify particle velocities near the front wall. Hence, the bed was homogenously illuminated using halogen lights and bed media was used as seeding particles to quantify its velocity field. The camera was located at a distance of 1.0 m from the front wall which enabled a field-of-view covering the full width and expanded height of the bed. Magnification factor of this setup ensures that each particle occupies approximately 3-4 pixels on a CCD frame of the 4 Mpx PIV camera.

Measurement at each flow rate included 25 double frame images taken at a trigger rate of 7.4 Hz. This resulted in measuring the flow field over 3.38 s. Time delay between each pair of double frame images was 1 ms. An adaptive correlation technique was applied where the interrogation area (IA) for each reading was iteratively reduced from 128x128 pixels to 32x32 pixels in 2 steps. The relative overlap of 25% and the peak validation of 1.2 were applied for PIV analysis.

3.2.4 DIA

A digital image can be defined as a finite two-dimensional function (intensity) of discrete spatial coordinates (pixels). 12 bit images were captured in these experiments, ranging the pixel intensity level from 0 (for dark regions) to 4095 (for bright regions) for a window of 2048 x 2048 pixels.

The main purpose for using DIA in this research was to detect the edges of different regions within the grid-zone. A Prewitt high pass filter was applied to the image mean for edge identification. Prewitt filter excels in estimating horizontal and vertical gradients and in general responded better than other high pass filters like Roberts and Sobel.

3.3 Analysis procedure

3.3.1 Grid-zone model description

The grid-zone region of fluidized bed is shown in **Figure 10** to be divided into three sub zones: particle moving zone, dead zone and jetting zone [76, 101, 104, 105]. The procedure to measure the grid-zone parameters is described in Section 3.2 of reference [101].

Jet profiles can be classified into three systems: isolated, transitional and interacting, based on whether the respective moving zones of jets are interacting with the adjacent moving zones [101, 106]. Jet systems were defined to be isolated if the moving zone of the adjacent jets did not mix with each other, as seen in **Figure 11(a)**. In a similar way, interacting jet systems were observed when all the jets in the system have moving zones that intermix with adjacent ones, as seen in **Figure 11(b)**. In transitional jet systems, some jets behaved as isolated while others had moving zones that intermix with adjacent ones. The occurrence of these three systems was dependent on fluidization velocity, pitch of orifice and particle properties.

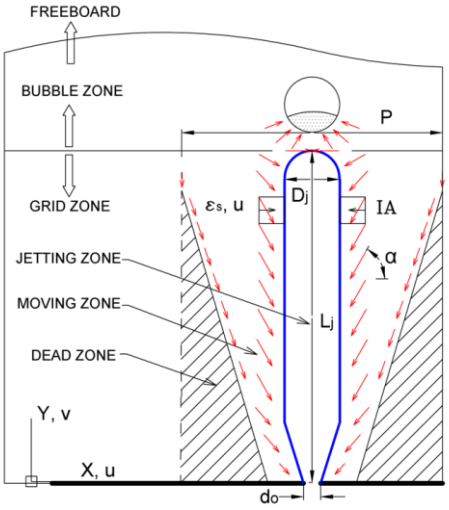

Figure 10: Phenomenological model for jets in two-dimensional beds

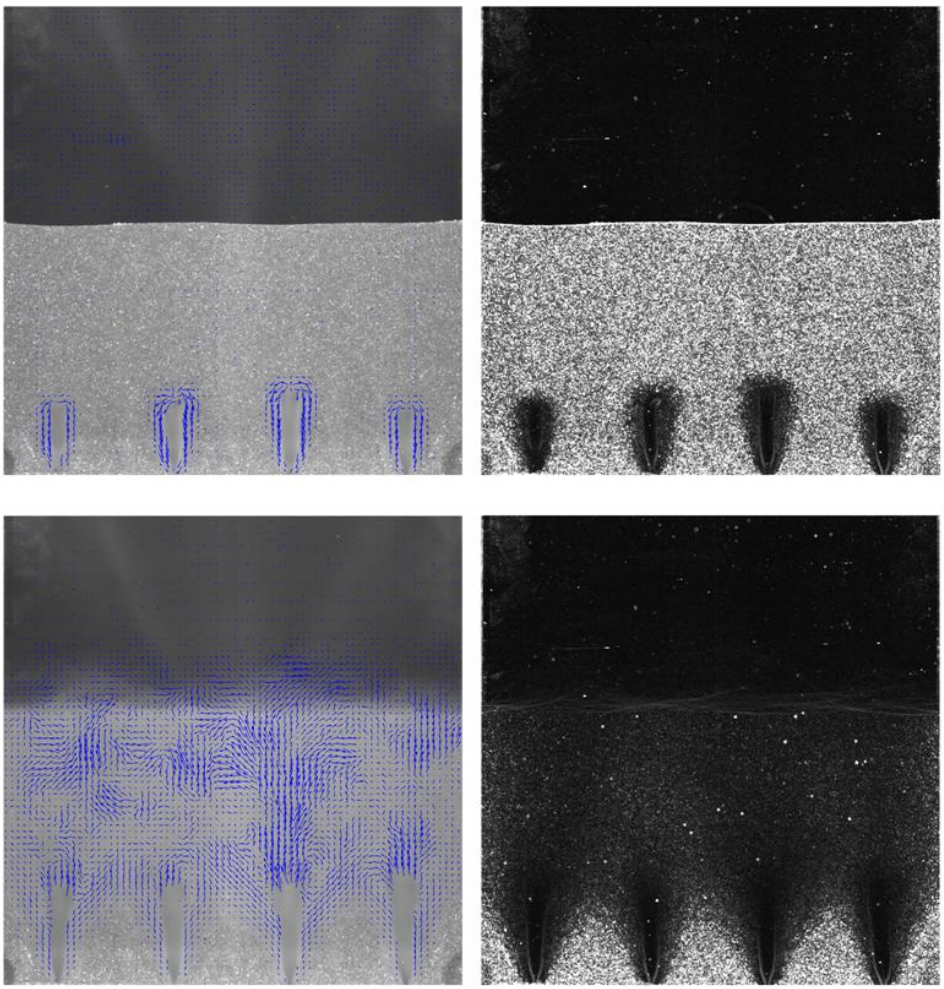

Figure 11: PIV data on mean image of acquired images, and Prewitt filter data. Type B1 distributor with glass 550 μm particles (a) $U_f / U_{mf,2D}$ = 1.12, isolated system and (b) $U_f / U_{mf,2D}$ = 1.46, interacting system.

3.3.2 Solid volume fraction

The time average intensity analysis of these images can be used to determine the solid volume fraction in a two-dimensional bed [95, 96, 98, 107, 108]. The complete description of calculating solid volume fraction from time averaged intensity maps has been described in 'Solid volume fraction analysis procedure' section in reference [102].

3.3.3 Particle entrainment and solid circulation

The jet boundary was determined to be linearly expanding from the orifice to the maximum diameter, as shown in **Figure 10**. Above this, the jet diameter remains constant until the bubble

generates at jet tip [101]. Particle velocity vectors $\vec{u}$ and $\vec{v}$ of each interrogation area (IA) were multiplied with their respective ε_s and particle density, ρ_p, to calculate horizontal and vertical particle mass fluxes ($\dot{m}_x''$ and $\dot{m}_y''$) respectively. The horizontal particle mass flux, $\dot{m}_x''$, calculated along the jet boundary was multiplied with the jet surface area to obtain the particle entrainment rate for individual jets, $\dot{m}_{x,j}$. The jet surface area was calculated assuming the jet structure to be of a semicircular cross-section along the front wall. The jet diameter was always found to be less than the thickness of the bed [101]. The expansion angle for each jet was calculated [101] to accurately determine the jet boundary and estimate the proposed jet surface area. The particle entrainment values were added for each jet to get the total solid circulation rate of the bed, $\dot{m}_{x,tot}$, at a set air flow rate.

3.4 Results and Discussion

3.4.1 Jet diameter and length

As shown in **Figure 12(a)**, the maximum jet diameter was found to depend only on d_o and U_o, similar to the studies of Merry *et al.* [109] and Rees *et al.* [104]. In order to compare the dependency of the experimental D_j on operating conditions, a correlation was developed and compared with the correlations of Merry *et. al.* [109] and Rees *et. al*. [104]. Assuming that the contribution from gravitational constant, g, remains the same, the correlation developed from the method of least-squares is:

$$D_j = 0.283 d_o^{0.71} U_o^{0.31} g^{-0.2} \quad (1)$$

95% of data lies within ±20% of the estimated correlation value. Rees *et al.* experimentally determined that $D_j \propto d_o^{n1}$ and $D_j \propto U_o^{n2}$, where $0.28 \leq n1 \leq 1.40$ and $0.36 \leq n2 \leq 0.48$. The power of d_o in Eqn. (1) is within the range recommended by Rees *et. al*. For the power of U_o, the value in Eqn. (1) was found to be slightly lower than the values proposed in correlations of Merry *et. al*. [109] and Rees *et. al*. [104]. The overall multiplication factor of 0.283 in Eqn. (1) is lower than similar factors listed in correlations of Merry *et. al.* [109] and Rees *et. al* [104]. The complete results for this topic are present in reference [101].

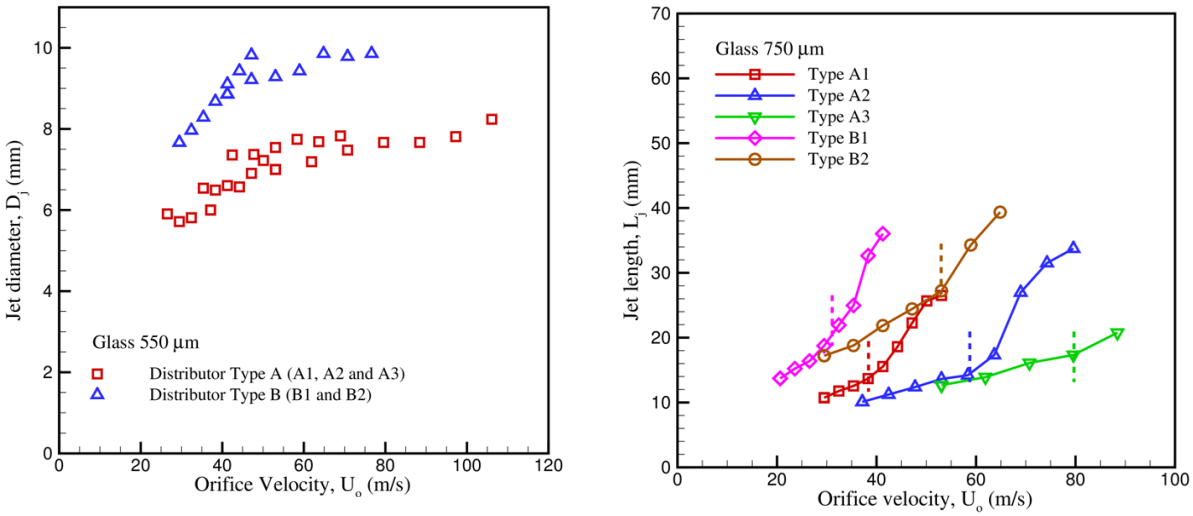

Figure 12: Jetting zone parameters (a) Jet diameter (b) Jet length

A plot of the jet penetration length, L_j, for glass 750 µm particles is provided in **Figure 12(b)** for all distributor plates. From this plot, the following trends were observed for L_j:

a) Jet length increased with an increase in jet orifice velocity. This rate of increase in jet length increased at higher orifice velocities.

b) Comparing results from distributor Types A1 and B1, which have the exactly same orifice velocities, revealed an increase in jet length for increased orifice diameter.

c) Increase in orifice pitch among the experiments with the same distributor Types (A or B) showed a decrease in jet length only at high orifice velocities. At lower orifice velocities, this difference was not significant.

d) An increase in media diameter, d_p, from 550 μm to 750 μm for test cases with glass particles resulted in a decrease of jet length. However, this also changed the particle classification from Geldart B to D.

e) Decreasing ρ_p from the test case of glass 550 µm to ceramic 550 µm resulted in an increase in jet length.

An important point taken from these observations was the change in the jet length behavior at high orifice velocities. After a certain increase in orifice velocity, the rate of increase in jet length increases and the dependence on the orifice pitch becomes apparent. Muller *et al.* [110] also observed a similar behavior for the jets in a cylindrical bed and proposed that this change occurs at a superficial velocity of $0.8\times U_{mf}$ flowing through the bed. To confirm this

observation, the minimum fluidization velocity ($U_{mf,2D}$) was calculated for each combination of particle type and distributor type in the two-dimensional bed. The orifice velocities corresponding to this $U_{mf,2D}$ were termed as $U_{o,mf,2D}$ and are plotted as dashed lines in **Figure 12(b)**. The presence of these lines corresponds to the location where the jet length changes its behavior. It was therefore concluded that the jets change their behavior at the minimum fluidization velocity of the particles calculated with a particular distributor plate. Thus for velocities above minimum fluidization, the ratio of volume of air percolating from the jet to the volume of air injected into the fluidized bed system would be lower than the same ratio calculated at velocities below minimum fluidization.

As a result, the fluidization regime for the jet length was divided into two orifice velocity ranges:

Range A: ($U_o \leq U_{o,mf,2D}$) Range where the jet length increases with orifice velocity at a lower rate than Range B and is unaffected by change in orifice pitch.

$$\frac{L_j}{d_o} = 0.68\left(\frac{U_o^2}{gd_o}\right)^{0.28}\left(\frac{U_{mf}^2}{gd_o}\right)^{-0.54} \tag{2}$$

Range B: ($U_o > U_{o,mf,2D}$) Range where the jet length increases with U_o at a higher rate than Range A and an increase in orifice pitch decreases jet length.

$$\frac{L_j}{d_o} = 0.44\left(\frac{U_o^2}{gd_o}\right)^{0.43}\left(\frac{U_{mf}^2}{gd_o}\right)^{-0.54}\left(\frac{d_o^2}{A_o}\right)^{-0.20} \tag{3}$$

These correlations indicate that L_j is directly proportional to d_o and U_o but is inversely proportional to U_{mf}. Furthermore, consistent with the data, the power dependence of U_o is higher for Range B, $L_j \propto U_o^{0.86}$, than Range A, $L_j \propto U_o^{0.56}$. The effect of particle type is included in the correlations through the values of U_{mf}. With $L_j \propto U_{mf}^{-1.08}$ for both Eqn. (2) and (3), the effect of particle type remains constant for the two correlations as expected. Inverse dependencies on U_{mf} account for lower jet lengths in systems those are difficult to fluidize. Eqn. (3) gives $L_j \propto A_o^{-0.20}$ suggesting that L_j decreases for higher orifice pitch for Range B. The comparison of the

developed correlations with experimental data and literature correlations is presented in Section 4.3.3.2 of reference [101].

3.4.2 Solid volume fraction

The time-averaged I_{cor} value for each IA was converted to the mean solid volume fraction, ε_s, along the thickness of the bed using the following correlation.

$$\varepsilon_s = \left(AI_{cor} \right)^B \tag{4}$$

The term AI_{cor} represents the area fraction occupied by illuminated particles on the front wall of the fluidized bed. The basis for the assumption came from the studies conducted by Heffels *et al*. [111] and Boerefjin *et al*. [108] , in which they concluded that the backscattered light reflected from the particle suspensions is an indication of the total reflecting surface area of the particles. A similar conclusion was made by Poletto *et al*. [107] using image analysis on a water fluidized bed of $3d_p$ bed thickness. The parameter *B* was introduced in Eqn. (4) to convert this area fraction to mean solid volume fraction, ε_s, along the thickness of the bed. This was followed by the work of Link *et al*. [95, 96].

Figure 13(a) contains the plot of bulk solid fraction, $\varepsilon_{s,b}$, along with time-averaged and expanded bed dimension averaged corrected intensity, I_{cor}. A least-square fit to the $\varepsilon_{s,b}$ data using the Eq. (4) is also plotted for the corresponding fluidization velocity test case. The constants *A* and *B* values were found close to the values reported by Link *et al*. [95], with constant *B* value being close to 1.42 for all three particles types and constant *A* varying around 1.0 with some dependence on particle type and size.

The absolute error in total bed mass calculated using the solid fraction model, Eqn. (4), against the actual mass of particles fluidized in the bed was found to be less than 15% for all nine test cases at varying fluidization velocities. **Figure 13(c)** contains the void fraction map $\left(\varepsilon_f = 1 - \varepsilon_s \right)$, calculated using Eqn. (4), for the instantaneous image shown in **Figure 13(b)**. Further validation of solid fraction model is shown elsewhere [102].

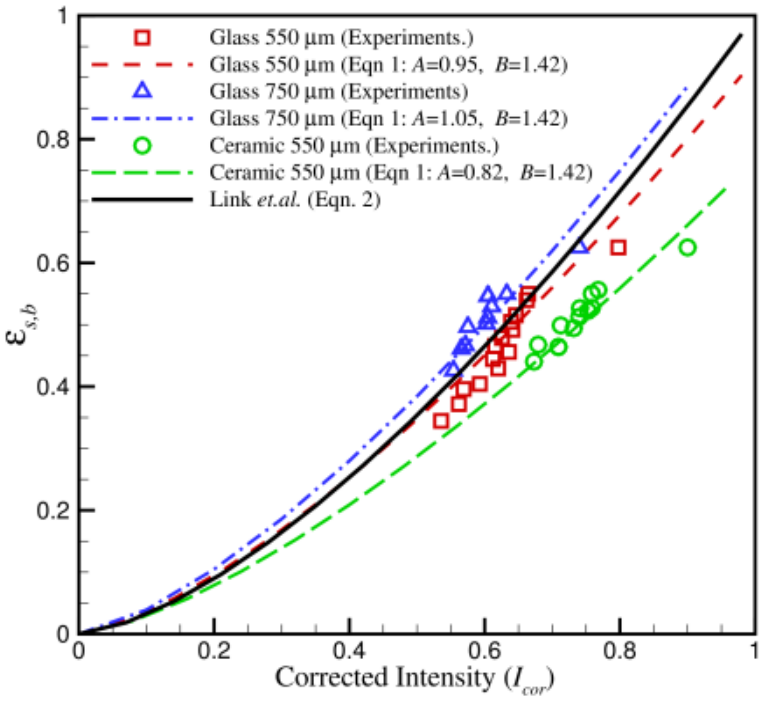

(a)

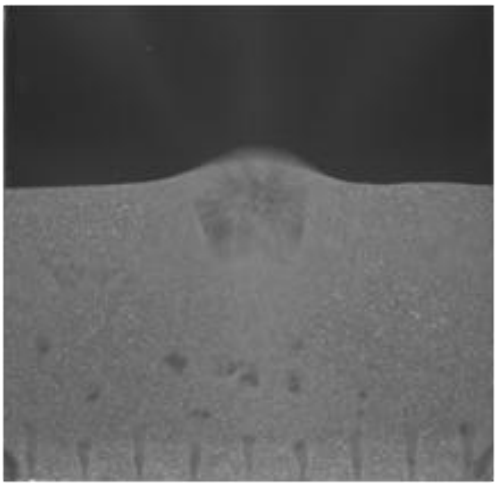

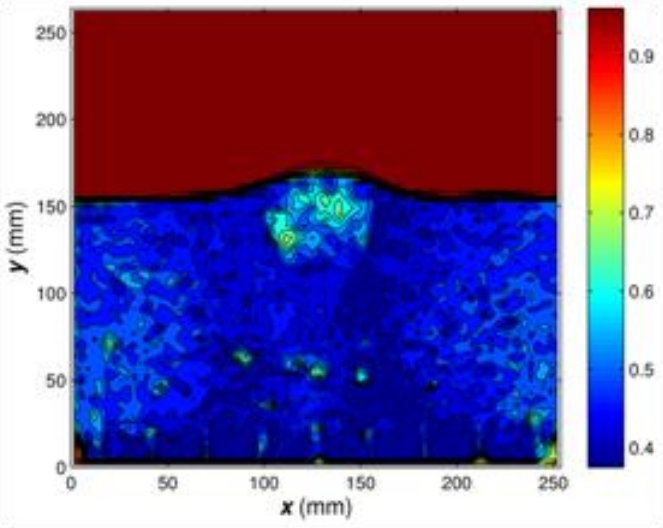

(b) (c)

Figure 13: Solid volume fraction results (a) Comparison of ε_s correlation (Eq. 4) $\varepsilon_{s,b}$ values for all test cases. (b) Instantaneous image of glass µm particles using A1 distributor plate (c) Void fraction map for (b)

3.4.3 Particle entrainment and solid circulation

This section reviews the effect of variations in fluidization velocity, particle properties and distributor types on solid circulation and particle entrainment rates.

3.4.3.1 Fluidization velocity

Figure 14(a) provides a plot of solid circulation rate for three particle types using the Type A1 distributor. Solid circulation was found to increase linearly with an increase in fluidization velocity until the jet systems transitioned from isolated to interacting jets. For the interacting jet systems, the rate of increase of solid circulation suddenly decreased in comparison to isolated jet systems. Although the linear increase of solid circulation with fluidization velocity has been observed in previous studies [79, 80, 87, 88], the sudden change in the rate of solid circulation has not been reported in the literature due to the lack of multiple jet studies. The relative leveling of solid circulation rate with fluidization velocity indicates that an optimum operating condition may exist for the applications that require high solid circulation for lower air input flow rate.

The accuracy of these solid circulation rate values were evaluated by comparing them with an alternate method presented by van Deemter [67]. The calculated solid circulation rates from van Deemter [67] method are plotted in **Figure 14(a)** along with an uncertainty of ±18.2%. These rates are close in comparison to the values calculated in the current study, with ±14.9% uncertainty.

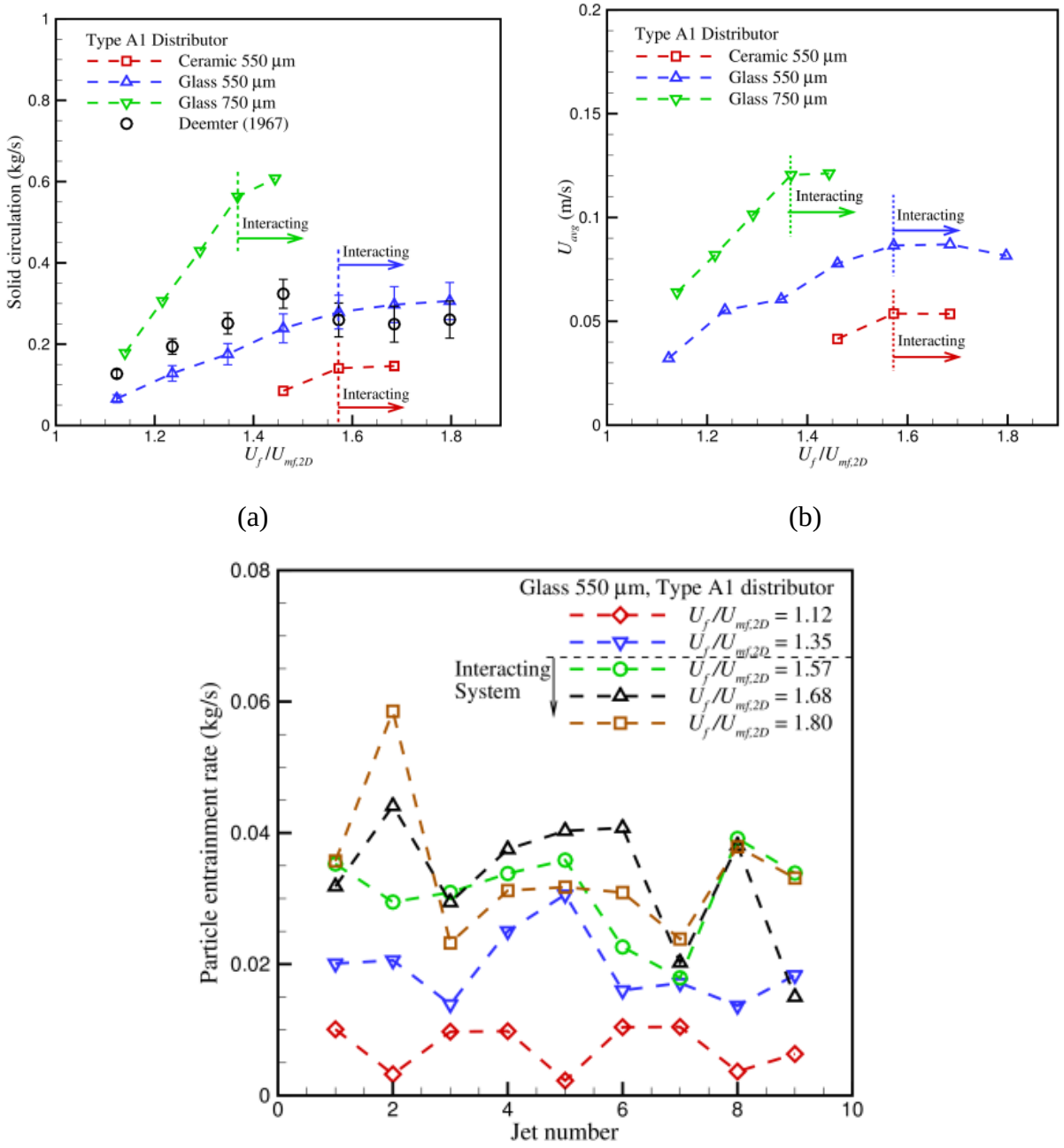

Figure 14: (a) Solid circulation rate versus U_f / $U_{mf,2D}$ (b) : Average entrainment velocity, U_{avg}, versus U_f / $U_{mf,2D}$ (c) Particle entrainment rate for individual jets in Distributor A1, from left to right

It was found that the major factor contributing to the leveling of solid circulation rate, calculated by the current experimental scheme, was the leveling of the horizontal particle entrainment velocity, $\vec{u}$, for the interacting jet systems. **Figure 14(b)** contains a plot of average entrainment velocities, U_{avg}, for the three test cases mentioned in **Figure 14(a)**.

Figure 14(c) provides the particle entrainment rate for each of nine individual jets with glass 550 μm particles and Type A1 distributor. It was observed that the particle entrainment in each jet is not same at a particular U_f. This difference in particle entrainment is primarily attributed to differences in jet lengths, L_j, and U_{avg} for each jet. Jet diameter, D_j, and ε_s values along the jet periphery did not differ considerably for each jet . **Figure 14(c)** demonstrates that the particle entrainment for a particular orifice does not necessarily increase with an increase in U_f. This phenomena was particularly evident for the interacting jet systems (U_f /$U_{mf,2D}$ = 1.57–1.80). However, as noted in **Figure 14(a)**, a net increase in solid circulation with U_f is always observed.

3.4.3.2 Particle properties

Figure 15(a) contains a comparison of volumetric circulation rate for glass 550 μm and ceramic 550 μm particles using Type A1 distributor. The volumetric circulation rate was calculated by dividing the solid circulation rate with the respective particle density. As observed from the plot, the circulation rate of ceramic 550 μm particles was 14-17% higher than glass 550 μm particles at U_f /$U_{mf,2D}$ > 1.57. For a relatively high difference in the particle density, the difference in volumetric circulation rate is small.

Figure 15(b) contains the comparison for solid circulation rate of the two glass particle types using Type B1 distributor. As observed, the solid circulation rate for glass 750 μm particles exceeded that of the glass 550 μm particles. A similar trend was seen in **Figure 14(a)** when both particles were tested with the Type A1 distributor.

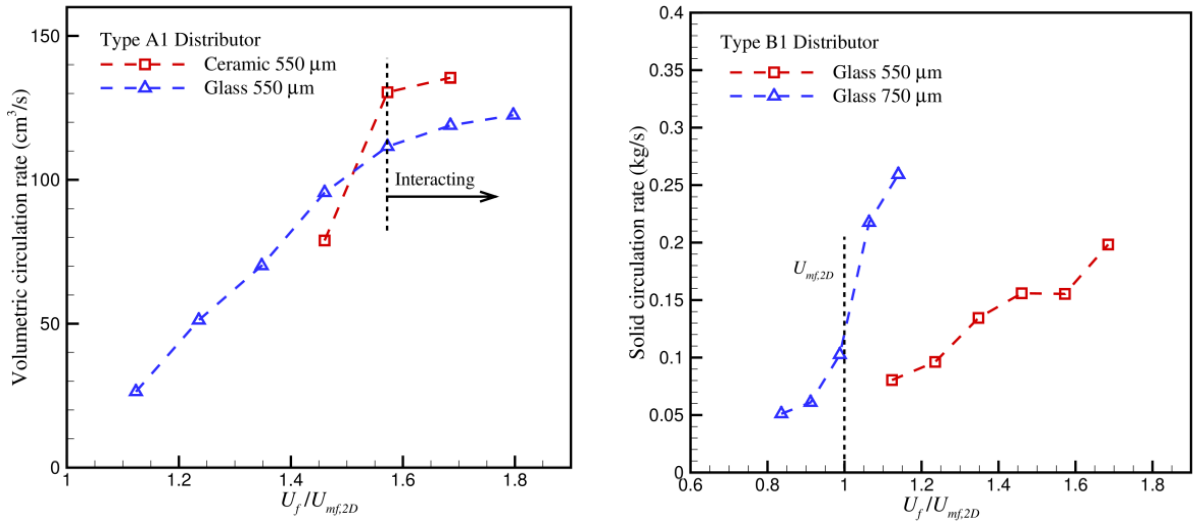

Figure 15: Effect of particle properties (a) Volumetric circulation rate versus U_f / $U_{mf,2D}$ (b) Solid circulation rate versus U_f / $U_{mf,2D}$ for glass 550 µm and glass 750 µm particles

3.4.3.3 Distributor configuration

Figure 16(a) shows the solid circulation rate for A1 and A2 distributors versus U_f /$U_{mf,2D}$. The solid circulation rate of Type A2 distributor was slightly higher, if not equal, to the data for Type A1. Due to fewer holes in Type A2 distributor, the orifice velocity, U_o, for Type A2 is calculated to be higher than Type A1 at same U_f. Hence, at the same U_o, the solid circulation rate for Type A1 distributor was found to be higher than Type A2. The solid circulation rate of Type A1 is due to higher U_{avg} velocities, high N, and L_j [101] at the same U_o. Therefore, the total solid circulation rate for the bed decreased with increase in orifice pitch, when compared at the same orifice velocity.

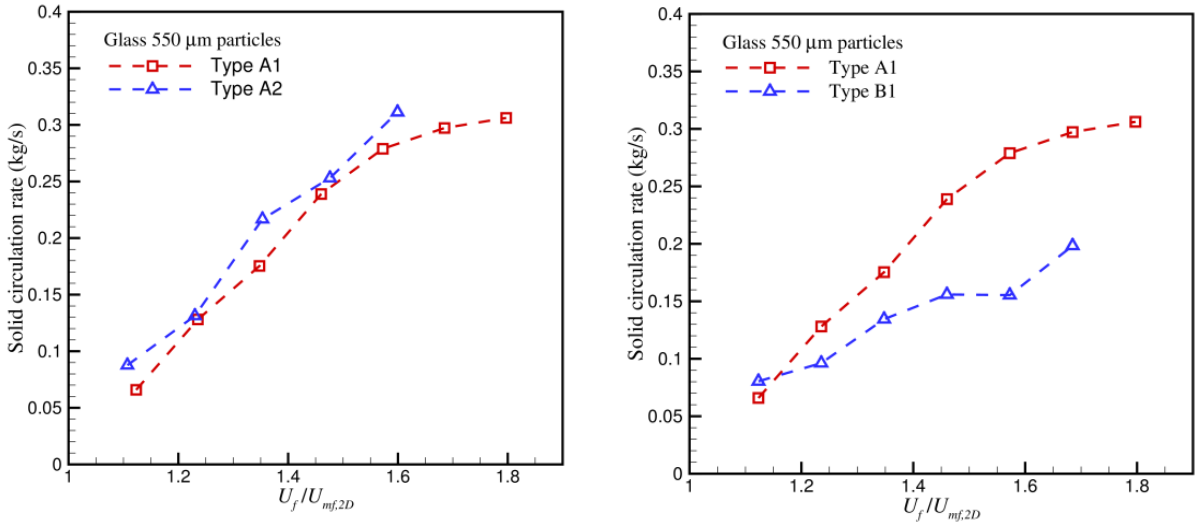

Figure 16: Solid circulation rate versus U_f / $U_{mf,2D}$ for (a) Type A1 and A2 distributor plates using glass 550 µm particles (b) Type A1 and B1 distributor plates using glass 550 µm particles

The effect of orifice diameter, d_o, on solid circulation rate was measured by testing glass 550 µm particles with distributor Types A1 and B1. **Figure 16(b)** contains the solid circulation rate data for the two test cases. As noted from **Table 3**, the $U_{mf,2D}$ for both test-cases is same. As observed, the circulation rate for Type A1 was measured to be 30-80% higher than Type B1 distributor. Hence, a distributor plate design with large number of small d_o was found to be effective at enhancing the circulation rate.

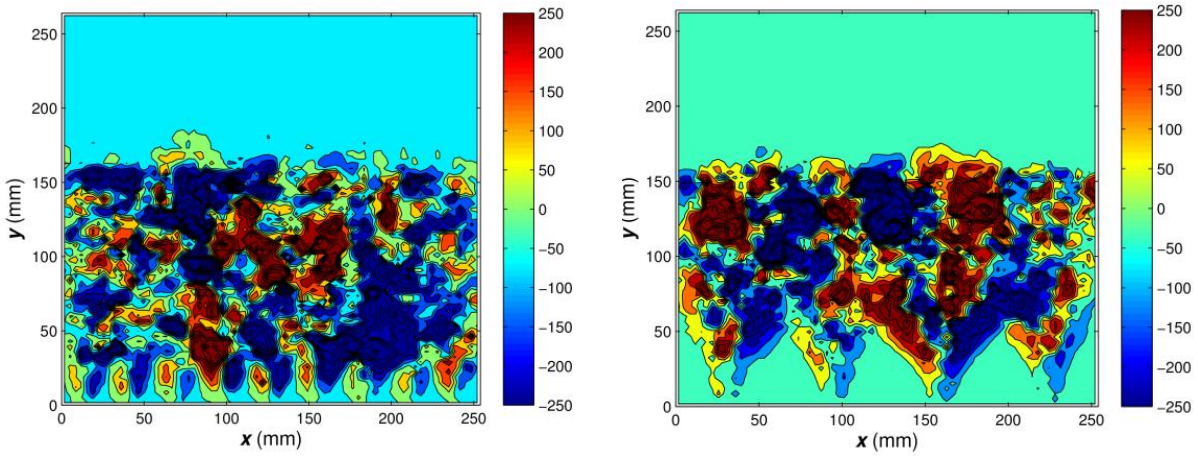

Figure 17: Comparison of $\dot{m}_x''$ maps, at $U_f/U_{mf,2D}$=1.46 using glass 550 µm particles (a) Type A1 (b) Type B1 distributor

This is also evident from the horizontal particle mass flux, $\dot{m}_x''$, maps plotted for the two distributor plates at $U_f/U_{mf,2D}$ = 1.46 using glass 550 μm particles in **Figure 17 (a)** and **(b)**. The $\dot{m}_x''$ maps show a more uniform mixing for Type A1 distributor plate. For Type B1 distributor plate, the mixing was not existent in the dead zones regions [101].

3.5 Conclusions

PIV and DIA were used in this study on a two-dimensional fluidized bed setup to investigate the evolution of multiple gas inlet jets located at the distributor base. Results were used to develop a grid-zone phenomenological model and quantify the effects of fluidization velocity, orifice diameter, orifice pitch, particle diameter, and particle density on solid circulation in fluidized beds. It was found that the most important parameters to quantify the particle entrainment rate are particle velocities, void fraction values, jet diameter and jet penetration length.

Jet diameters were found to be dependent only on orifice velocity and orifice diameter. Jet length was found to increase with an increase in orifice velocity and orifice diameter. Jet length was also found to decrease with an increase in particle density, particle diameter, and orifice pitch. It was determined from this study that jet penetration length behavior is consistently different for fluidization velocity below and above minimum fluidization. For velocities above minimum fluidization, jet lengths were found to increase more rapidly with increase in orifice velocity than for operating conditions below minimum fluidization. As a result, two separate correlations were developed to predict jet length with velocities below and above the minimum fluidization velocity.

A model was developed to estimate the solid volume fraction using digital image analysis on the results. The solid volume fraction model compared well with a similar model suggested by Link *et al.* [95, 96]. For all test cases, the mass of bed media estimated using this model was within 15% of the actual bed mass. The solid volume fraction profiles were found similar to those observed in the literature.

Solid circulation was found to increase linearly with an increase in fluidization velocity until the jet systems transitioned from isolated jets to interacting systems. For an interacting jet system, the solid circulation increased with fluidization velocity but at a much lower rate. In a multiple jet system, this phenomenon may indicate an optimum operating condition for a bed that requires high circulation rate for low air input. The accuracy of the solid circulation rate

calculated in the current experimental study was verified by the circulation rate calculated by the counter-current flow model in the literature [67-69].

The circulation rate was observed to slightly increase with the decrease in particle density from 2500 kg/m^3 to 1079 kg/m^3 at same U_f / $U_{mf,2D}$. For U_f / $U_{mf,2D}$ > 1, the solid circulation rate and entrainment velocities for glass 750 μm particles exceeded that of glass 550 μm particles.

At the same orifice velocities, a higher circulation rate was noted for distributors with smaller orifice pitch. At the same fluidization velocities and for distributors with different orifice diameters but the same orifice flow area, the circulation rate was noted to be much higher for distributors with smaller diameter orifices. Hence, for a distributor plate design, the plate with large number of small diameter orifices was found to enhance the solid circulation rate.

3.6 Nomenclature

A	Constant to convert I_{cor} to area fraction projected at front wall
A_d	Area of distributor (m^2)
B	Constant to convert projected area fraction to ε_s
D_j	Jet diameter (m)
d_o	Diameter of orifice in distributor plate (m)
d_p	Mean particle diameter (m)
fr_{neg}	Fraction of bed moving with a negative vertical velocity at a specific fluidization velocity
g	Acceleration due to gravity (m/s^2)
I_{cor}	Corrected image intensity averaged over an interrogation area
I_m	Manipulated intensity of the captured image
L_j	Jet penetration length (m)
$\dot{m}''_x$	Horizontal particle mass flux in the interrogation area; = $\rho_p \varepsilon_s \vec{u}$ (kg/m^{2}s)
$\dot{m}''_y$	Vertical particle mass flux in the interrogation area; = $\rho_p \varepsilon_s \vec{v}$ (kg/m^{2}s)
$\dot{m}_{x,j}$	Horizontal particle entrainment rate of a particular jet (kg/s)
$\dot{m}_{x,tot}$	Total solid circulation rate of the bed (kg/s); = $\sum_{j=1}^{N} \dot{m}_{x,j}$
N	Number of orifices within the distributor plate
$n1$	Empirical constant 1

$n2$	Empirical constant 2
P	Pitch of orifices within the distributor (m)
ρ_p	Density of particles (kg/m^3)
U_{avg}	Average of $\vec{u}$ calculated at jet periphery for all jets in a bed at a set air flow rate
U_f	Superficial gas velocity (m/s)
U_{mf}	Superficial gas velocity at minimum fluidization (m/s)
$U_{mf,2D}$	Experimental U_{mf} of corresponding distributor plate and particle test case (m/s)
$U_{mf,3D}$	Experimental minimum fluidization velocity measured in a cylindrical bed; = U_{mf} (m/s)
U_o	Mean orifice velocity (m/s); $=\left(U_f A_d\right)\Big/ N\left(\pi d_o^2 / 4\right)$
$\vec{u}$	Horizontal particle velocity vector in the interrogation area (m/s)
$\vec{v}$	Vertical particle velocity vector in the interrogation area (m/s)
$\left\|v_{neg,avg}\right\|$	Mean negative vertical velocity of the particles at specific fluidization velocity
x	Horizontal location along the width of fluidized bed (m)
y	Vertical location from the distributor base (m)

4. PHYSICOCHEMICAL CHARACTERIZATION

4.1 Introduction

An organized methodology is required to qualitatively and quantitatively understand the pyrolysis and combustion behavior of coal-biomass fuel blends. The blend pyrolysis-combustion behavior must be understood in terms of its physicochemical changes, kinetic parameters, evolved gas aspects and associated pyrolysis-combustion energetics. Based on these main aspects of analysis, a fuel pyrolysis and combustion performance model must be developed to compare the performance of different fuel blends. This understanding of pyrolysis-combustion behavior of fuel blends is developed in the subsequent chapters.

Accurate physicochemical characterization of blended fuel, their char and ash samples is necessary to determine the interactions between fuel constituents during pyrolysis and combustion. The understanding of physicochemical properties of fuel blends, their char and ash will assist predicting their pyrolysis-combustion performance and resolving the issues related to emissions and molten ash in a scaled-up reactor [112].

The physical properties, such as the size, shape and porosity of fuel particles are important parameters that define the fuel reactivity and residence time [113]. Similarly, chemical properties such as the composition of char material, and the distribution of carbon, hydrogen and oxygen elements directly influences the issues related to char ignition, combustion rate and flame-out related problems in combustors [114].

The differences in physicochemical properties of coal and biomass fuels needs to be quantified for proper understanding the pyrolysis-combustion behavior of fuels. Coal and biomass fuels contain organic elements (macerals) and inorganic components (minerals). The elemental composition of macerals (including C, H, O and organically bound inorganic elements) is directly dependent on the rank of the coal. Whereas the ash composition comprises of minerals and aluminosilicate glasses, which is directly related to the fuel source [114]. There are certain differences between the inorganic composition of coals and biomasses. While in coal most of the inorganic material is present as minerals, in biomasses these can exist as salts or organically bound to macerals [115]. Thus, the amount of inorganic material vaporizing in biomass samples is much higher (75% by weight) than those of coal samples (4% by weight) at high temperatures (1200°C) [115].

It has been demonstrated in many studies that the presence of the inorganic salts influence the primary reactions during the devolatilization process [17, 19, 115-117]. While most of the inorganic salts act as catalysts, many other acts as inhibitors [17]. Usage of biomass feedstocks in furnaces lead to operational problems such as slagging and fouling; however, usage of small amount (10-15%) of biomass with coal mixtures in co-firing applications does not show such negative effects [115]. Another way of reducing the influence of inorganic salts on biomass pyrolysis is to leach the feedstocks with water [25, 26, 118-121]. This process removes most of the potassium and chlorine based salts among many others, and also reduces the nitrogen-oxide content in the resultant chars. However, the combustion behavior of leached biomass has not been investigated or verified in scaled-up gasifiers/furnaces [115]. Thus, the effect of biomass water leaching and its influence on co-firing must be properly quantified from physicochemical perspective.

Traditional analysis techniques, such as proximate and ultimate analysis, can be used to estimate the elemental composition of fuels and chars. However, the inherent limitations of these techniques and the sampling and analytical errors associated may lead to misleading interpretations [114]. Thus, Alphen *et al*. [114] recommended detailed, accurate, and automated physicochemical characterization of fuel and ash properties using scanning electron microscope (SEM) techniques as a viable solution. SEM images can provide enlarged vision of fuel, char or ash samples with minor loss in precision. SEM instrument can be used with Backscattered Electron Imaging (BEI) and Energy Dispersive X-Ray Spectroscopy (EDX) stages to provide the elemental distribution of the sample.

Hence, a series of experiments were performed to quantify the effects of biomass leaching, differences in individual biomass and coal samples, and the impact of blending coal and biomass fuels from physicochemical perspective.

4.2 Experimental procedure

4.2.1 Materials and preparation

Samples used in this study included cornstover (CS) and switchgrass (SG) biomass feedstocks, as well as bituminous US eastern steam coal (EC), namely, McClure River. The proximate and ultimate analyses for these samples are provided in **Table 4** and **Table 5**, respectively.

Table 4: Proximate analysis (dry basis)

Fuel	EC	SG-Raw	CS-Raw
% Ash	10.50	2.86	5.01
% Sulfur	0.88	0.08	0.10
% Volatile	28.28	82.58	82.13
% Fixed carbon	61.22	14.56	12.86
Calorific value (kJ/kg)	32734	18873	18778
MAF calorific value (kJ/kg)	36574	19429	19769

Table 5: Ultimate analysis (dry basis)

Fuel	EC	SG-Raw	CS-Raw
% Carbon	82.26	48.81	53.27
% Hydrogen	4.75	6.32	5.67
% Nitrogen	1.56	0.35	0.62
% Sulfur	0.88	0.08	0.10
% Ash	10.50	2.86	5.01
% Oxygen	0.05	41.58	35.33

Biomass feedstocks were milled to produce finely ground samples. The finely ground biomass particles were sieved through calibrated sieves within 400-500 μm range. To examine the influence of inorganic salts, the biomass samples were tested in both untreated (Raw) and distilled water washed (Leached) states, as mentioned in the literature [25, 26, 118-121]. For this purpose, sieved biomass samples were leached at 110ºC temperature in a well stirred container for two hours before air drying them at 110ºC. All four biomass samples were dried at 110ºC in air before experimentation.

Eastern coal was received in the form of powder with the mean diameter being less than 400 μm sieve. The EC sample was received in a wet state (about 30% moisture by weight), and thus was thoroughly dried in air at 110 ºC for 4 hours before use. Two more test samples were prepared by mixing EC with leached biomass samples in the ratio of 80:20 by mass to investigate interactions between coal and salt-free biomass samples. The biomass sample weight ratio was restricted to 20% by mass as per the guidelines mentioned in the literature [37, 115]. Thus, in

total seven test samples were developed and experimented, including, EC, SG-Raw, CS-Raw, SG-Leached, CS-Leached, EC & SG-Leached mix (80:20 by mass) and EC & CS-Leached mix (80:20 by mass).

4.2.2 Instrumentation and procedure

An Environmental Scanning Electron Microscope (ESEM) was used to conduct the physicochemical characterization of the samples, while a Simultaneous Thermogravimetric Analyzer (STA) was used to produce the pyrolyzed char and char oxidized ash samples from the fuel for physicochemical analysis.

The physicochemical characterization of the solid fuels, pyrolyzed char and char oxidized ash samples was conducted using a Quanta 600 ESEM (**Figure 18**). ESEM images provided an enlarged vision of samples with a minor loss in precision, thus enabling the qualitative characterization of the microstructure of fuel, char and ash samples. Multiple images of the samples were collected at 100X, 1000X, 5000X and 10000X magnification levels.

Figure 18: Quanta 600 FEG ESEM

The ESEM instrument was further used with an Energy Dispersive X-ray Spectroscopy (EDX) stage to provide the elemental distribution at the surface of the sample. The major elements quantified on the sample surface included C, O, Si, Al, S, P, Na, Ca, K, Cl, Fe and Ti (for EC sample). Any other elements, if found in substantial amount in a sample, were also quantified. The hydrogen element was not quantified due to the limitations of the instrument. A rectangular area, spanning the maximum possible width and height of the particle at a particular magnification, was used to represent the elemental composition of the sample using EDX. The measurements were repeated for several particles of the sample, and an average composition

value was used for the analysis. The aforementioned elements were quantified on the basis of mass percentage. The tested fuel, char and ash samples were sputter coated with gold and platinum prior to the ESEM testing to enable imaging. The estimated sputter coated gold and platinum amounts were appropriately deducted from the subsequent elemental analysis of the sample.

The pyrolyzed char and char oxidized ash samples were prepared using the STA. The fuel samples were first pyrolyzed in inert nitrogen atmosphere by heating the samples at 20 K/min to 1073 K with a five minute residence time interval to prepare pyrolyzed char samples. Additional pyrolyzed char samples were further oxidized in 99.999% pure air at 1073 K for 30 minutes to prepare char oxidized ash samples. These samples were then used for physicochemical characterization in the ESEM.

4.3 Results and discussion

The physical effect of pyrolysis and char oxidation on different samples was investigated on a microscopic level using an ESEM. In addition, EDX was used to quantify the solid composition changes due to pyrolysis and char oxidation.

4.3.1 Biomass leaching

Figure 19(a) and **Figure 19(b)** shows the ESEM images of untreated (Raw) and washed (Leached) SG samples at 100X magnification, respectively. In these images, the samples can be seen sitting on top of an adhesive carbon tape. As observed from the figure, biomass particles have high aspect ratio, and the particles are roughly cylindrical and straight along the length. The particles of both samples remained straight along the length after washing and drying in air, and there were no physical differences observed at 100X magnification. Same observations were made for CS Raw and CS-Leached samples.

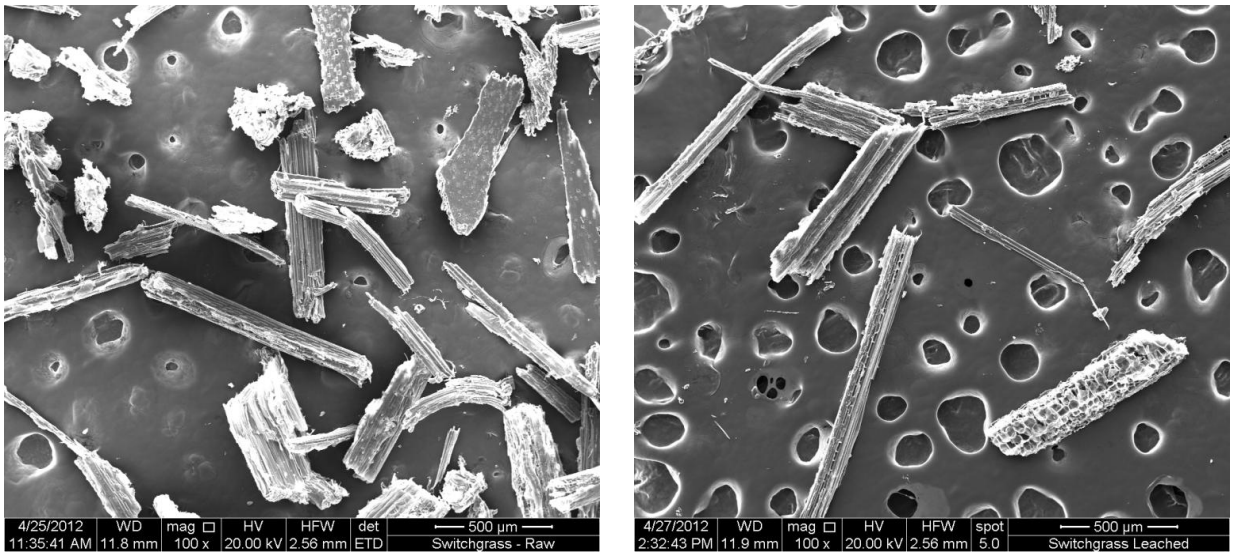

Figure 19: Switchgrass biomass at 100X magnification on top of a carbon tape (a) Raw (b) Water leached

ESEM images of raw and leached SG biomass at 1000X magnification are shown in **Figure 20(a)** and **Figure 20(b)**, respectively. Also included in the inset of **Figure 20** are the X-ray images of the particle for the Si element scan. As observed from **Figure 20(a)**, small spherical particles of inorganic K and Mg based salts are present on top of the smoother surface of raw SG particle. These K and Mg particles were washed out during the water leaching process, as observed from their absence in **Figure 20(b)**. The X-ray inset in **Figure 20(a)** shows Si and O based patches that are present in the SG particle. These patches disappear considerably during the water leaching process, as observed from **Figure 20(a)**. **Figure 21(a)** and **Figure 21(b)** shows the effect of water leaching on the major inorganic elements in SG and CS samples. As observed from **Figure 21(a)**, the Si concentration decreased by almost 42%, while the Mg and K elements were nearly eliminated on water leaching of SG. Potassium (K) was the major inorganic element found on the surface of CS particles, the concentration of which decreased by almost 68% on water leaching. However, the complete elimination of K element was not possible with just one water leaching cycle on CS sample, thus indicating higher amount of impurities in CS. A slight increase in Cl element was observed on leaching of both biomass samples, which may be attributed to the decrease in concentration of other inorganic elements.

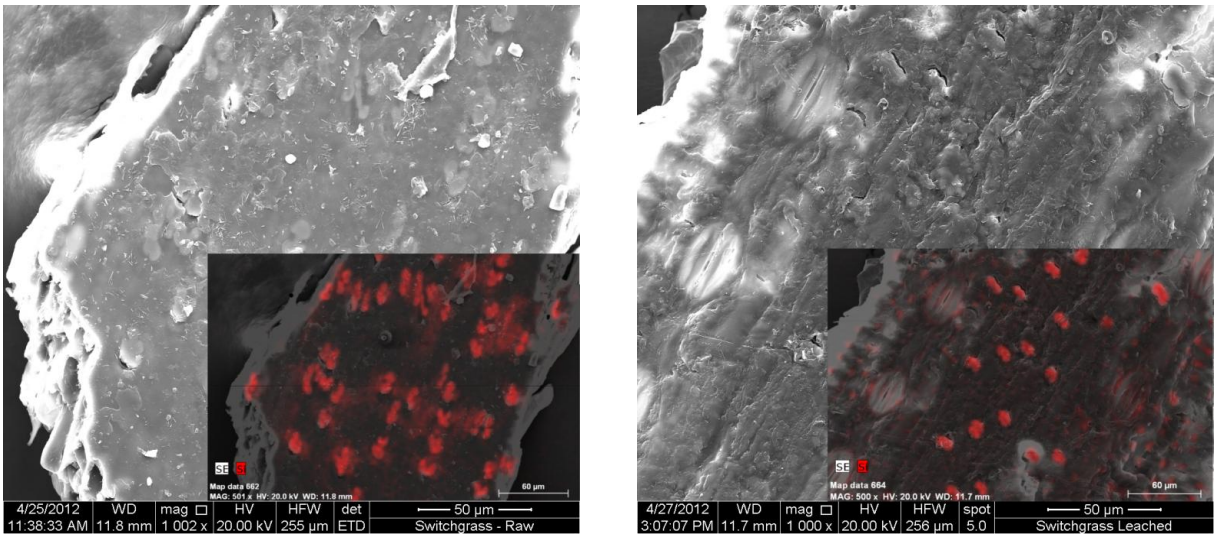

Figure 20: SG particle at 1000X magnification with Si element X-ray scan in the inset (a) SG-Raw (b) SG-Leached

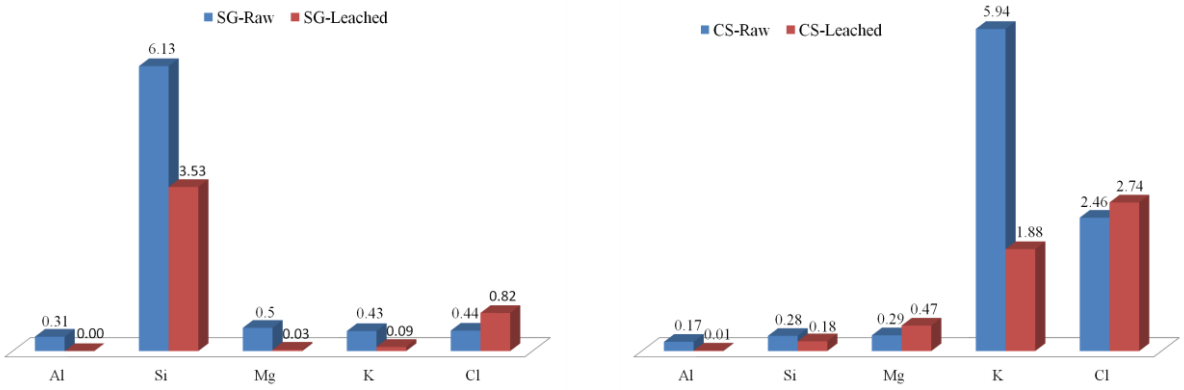

Figure 21: Effect of water leaching on major inorganic element concentrations of biomass samples (a) SG (b) CS

Table 6 shows the C%, O% and C/O percentage ratio for the raw and water leached biomass samples. As observed, the C% for biomass samples remains unchanged after water leaching. The O% of biomass samples was found to increase on water leaching (7% to 23%). Thus, water leaching caused a drop in the C/O ratio for biomass samples. The C/O ratio of CS was found to be a little higher than that for SG sample and this was primarily due to the large amount of Si-O patches found in the SG sample. This indicated that the energy density of CS sample is higher than that of SG sample, and is consistent with the MAF calorific value for the

two biomass samples reported in **Table 1**. Another point noted from the **Table 6** is regarding the accuracy of the C% (+0.9% to +2.6 % error) and O% (+0.6% to -3.8 % error) measured by the ESEM instrument compared to that measured through the ultimate analysis of Raw biomass samples provided in **Table 5**. This validates the accuracy of measurement methodology used in this analysis.

Table 6: Effect of leaching on biomass (C%, O% and C/O in mass percentage)

Sample @ 20 K/min	C %	O %	C/O
SG-Raw	49.7	42.2	1.2
SG-Leached	50.2	45.0	1.1
CS-Raw	56.1	31.6	1.8
CS-Leached	54.2	38.9	1.4

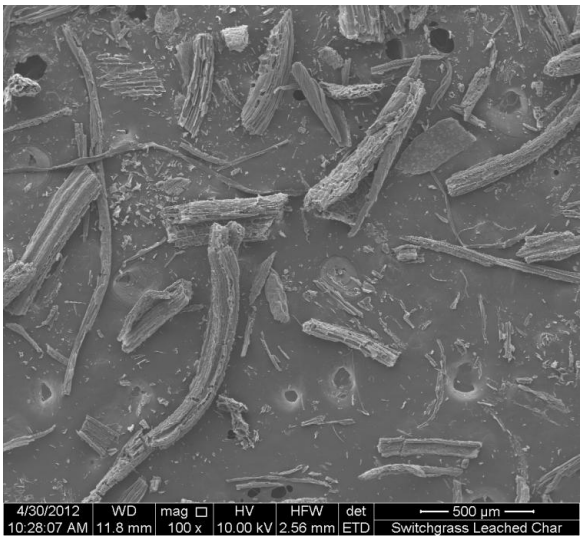

(a)

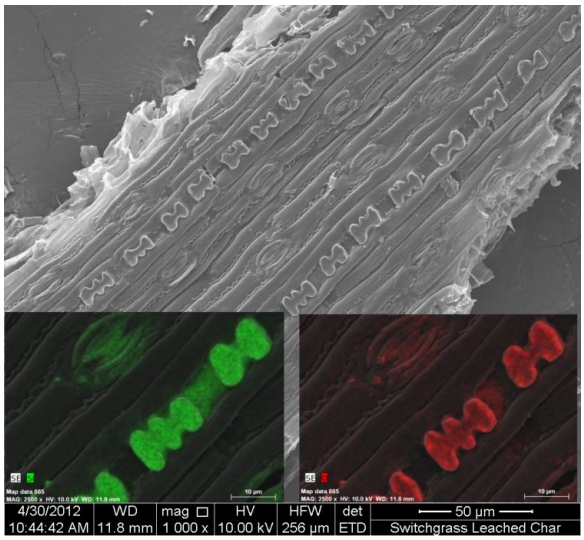

(b)

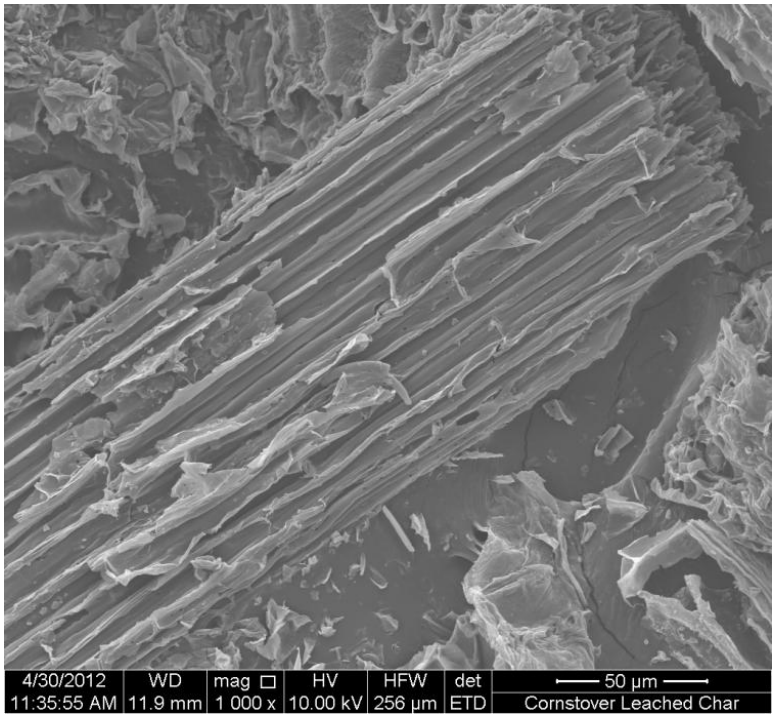

(c)

Figure 22: Pyrolyzed leached biomass samples (a) SG-Leached char at 100X magnification (b) SG-Leached char sample at 1000X magnification with Si (Green) and O (Red) element X-ray scans in the inset (c) CS-Leached char at 1000X magnification

Figure 22(a) shows the char of SG-Leached samples at 100X magnification. As observed from **Figure 22(a)**, the char particles of SG-Leached sample were found to be deformed in shape and more curved along the length than the original sample. There was also an emergence of smaller chipped char particles in **Figure 22(a)**, thus indicating a decrease in average aspect ratio of biomass particles following pyrolysis. A similar observation was made by Wornat *et al* [112] for SG samples. **Figure 22(b)** contains the 1000X magnified image for a SG-Leached char particle. The X-ray scan for Si and O elements is also included in the inset of **Figure 22(b)**. The same Si-O patches, as previously observed in **Figure 20(b)** for unpyrolyzed SG, were now more clearly visible on the surface of pyrolyzed char in **Figure 22(b)**. Thus, these patches indicated high concentration of Si and O elements in the SG-Leached sample. In comparison, the CS-Leached char particles did not show Si element patch pattern on its surface. This is consistent with **Figure 21(b)** where the Si concentration for CS samples is calculated to be substantially lower than SG samples. Instead, the char particles of CS-Leached sample show hollow zones which indicate the loss of organic matter during pyrolysis, as shown in **Figure 22(c)**.

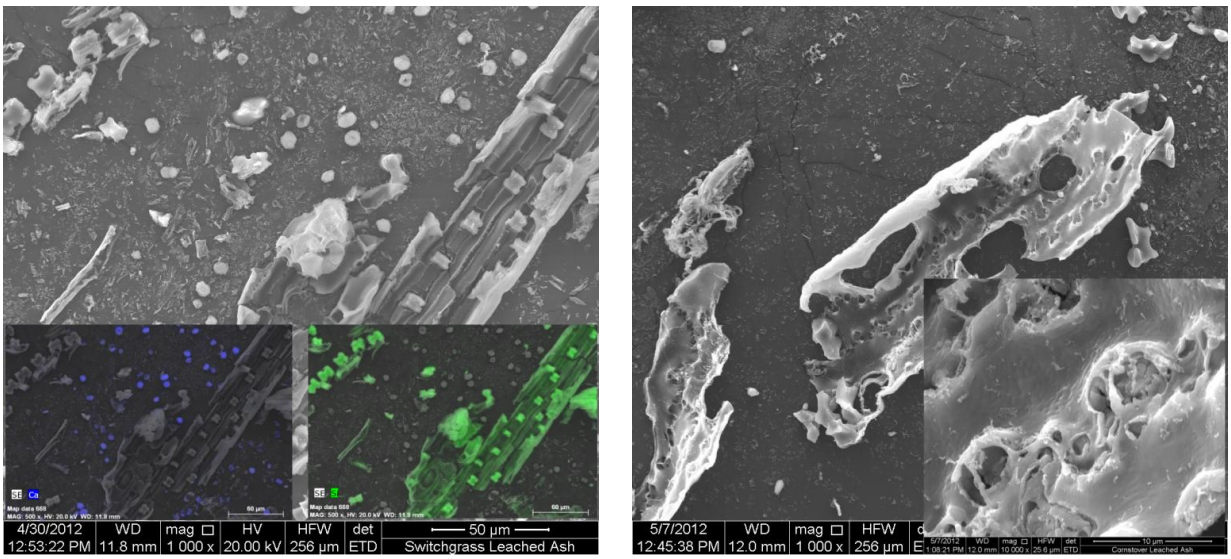

(a) (b)

Figure 23: Ash samples at 1000X magnification (a) SG-Leached ash with Ca and Si element X-ray scans in the inset (b) CS-Leached ash particle

Figure 23(a) includes the ESEM image for ash particles generated from SG-Leached sample at 1000X. The inset of **Figure 23(a)** contains the X-ray scan for Ca (Blue) and Si (Green) element. As observed from **Figure 23(a)**, the Ca spheres break off from the main organic body of SG ash sample. It is important to note that the Ca element was not visible on the surface of leach SG or its char sample. A scan for O element (not shown in the figure) indicated the spheres to likely be CaO salts. It is also observed that the Si-O patches remain organically bound to the main biomass shell even after oxidation [115], unlike the CaO spheres. In comparison, **Figure 23(b)** contains the ESEM image of for ash particles generated from CS-Leached sample at 1000X magnification. There was neither the presence of CaO particles, nor the pattern for Si-O patches on the CS ash shell. This is further evident from **Figure 24**, where the major elements in biomass ash samples are shown in their mass fraction percentages. As observed from **Figure 24**, the C, O and Si elements forms more than 90% of composition by mass in biomass ash samples. The amount of Si in SG ash is found to be approximately 62% higher than that of CS due to the presence of Si-O patches in SG. This is also indicated with a high amount of O element in the SG sample in comparison to the CS sample. However, this results in the amount of C element in the CS sample to be about 82% higher than the C content of SG sample.

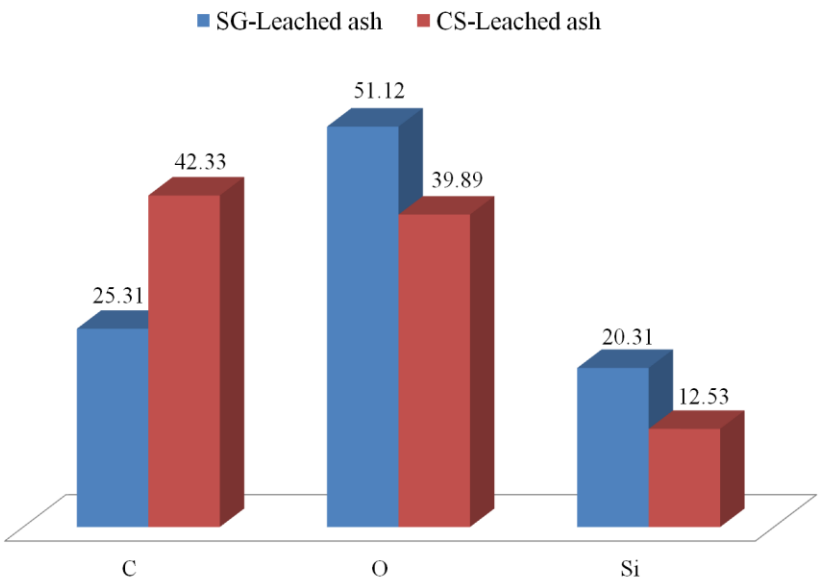

Figure 24: Major compounds in leached biomass ash samples

4.3.2 Coal and biomass comparison

Figure 25(a), **(b)** and **(c)** shows the EC, EC char and EC ash sample ESEM images at 100X magnification respectively. As seen from **Figure 25(a)**, the EC particles are more homogenous and have lower aspect ratio than the biomass particles. The EC particles, shown to be segregated in **Figure 25(a)**, fuse with adjacent particles on pyrolysis and increase in size, as shown in **Figure 25(b)**. This is in contrast to the biomass samples, where the average particle size and aspect ratio slightly decreased on pyrolysis. The EC char particles also differ from the charred biomass particles for their change in the surface morphology. A clear appearance of fissures is seen on the surface of EC char samples along with the swelling, unlike any such phenomena occurring on the biomass char particles shown in **Figure 22(b)** and **(c)**. Such phenomena was also reported by Biagini *et al*. [113], where fissures and small holes were found to appear on the swollen coal char samples due to volatiles released during the pyrolysis process. **Figure 25(c)** shows that EC ash particles are much smaller in size than EC char or unpyrolyzed EC particles; however, the EC ash particles were found to be in lumped state even after oxidation. This is in accordance to the literature where Hurt *et al*. [122] reported a significant amount of fused ash on the surface of char samples of Illinois coal, thus suggesting an advanced degree of oxidation.

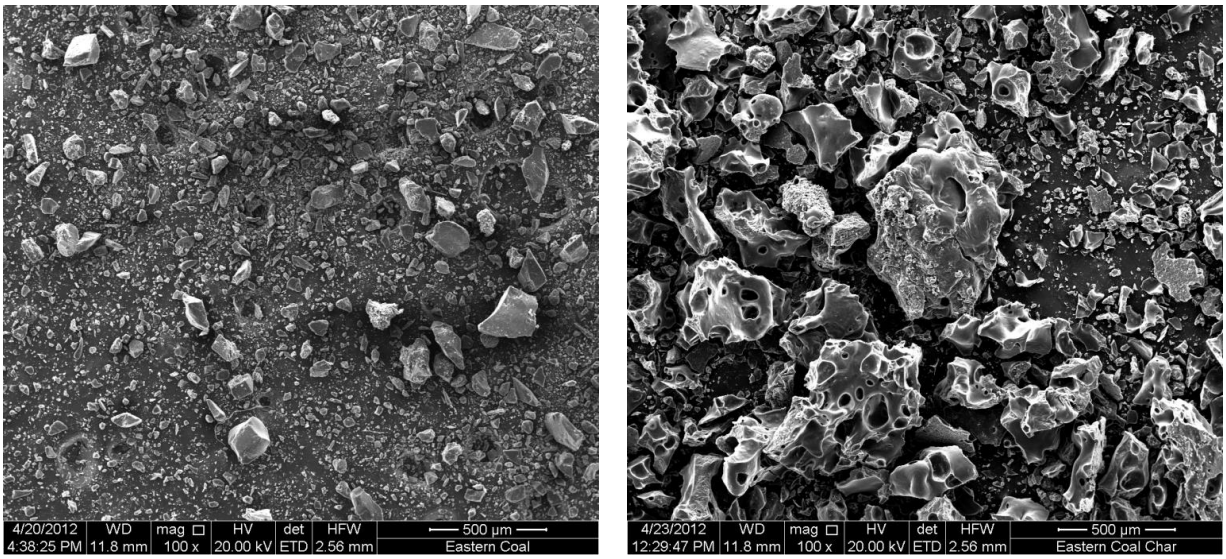

(a) (b)

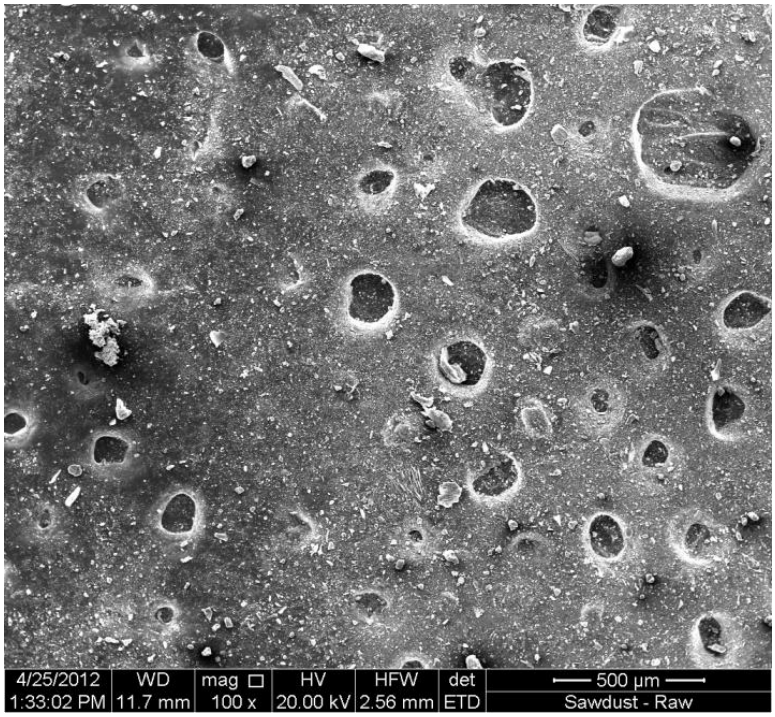

(c)

Figure 25: ESEM images for EC sample at 100X magnification (a) Un-pyrolyzed EC (b) EC char (c) EC ash

The difference in the elemental composition of coal and leached biomass samples is evident from the elemental analysis of ash compounds of these fuels, as shown in **Table 7**. As discussed in previous section and also observed from **Table 7**, the biomass ash consists of considerable amount of C, O and Si elements which keeps the ash predominantly organic. Unlike biomass samples, the coal ash is found to be predominantly inorganic with Fe (33%), Al(15%), Si(10%) forming the major oxides among other elements in smaller amounts. While the major oxides in EC ash are that of Fe, Al and Si, that of biomass ash consists of C, Si, K, Mg and Na. Also contrary to biomass, the C element percentage in the EC ash particle was found be as low as 6%, with O element percentage increasing to almost 34%, thus indicating the inorganic nature of EC ash in comparison to biomass.

Table 7: Elemental composition of EC, SG-Leached and CS-Leached ash samples

Ash %	C	O	Si	Al	Na	Mg	K	Ca	Cl	S	Fe	Ti
EC	7.80	34.11	8.79	14.30	0.73	1.10	0.00	0.48	0.00	1.03	31.11	0.28
SG-Leached	25.31	51.12	20.31	0.02	0.09	0.49	0.27	1.58	0.81	0.00	0.00	0.00
CS-Leached	42.33	39.89	12.53	0.01	0.05	0.99	1.71	1.94	0.56	0.00	0.00	0.00

Figure 26(a) shows the C/O percentage ratio of EC, SG-Leached and CS-Leached samples, as well as their char and ash samples. As observed from the **Figure 26(a)**, the C/O ratio for EC is 4-5 times higher than that of biomass samples. This indicates the high carbon density of coal in comparison to biomass, which is also evident from the differences in the calorific values reported for these samples in **Table 4**. Once pyrolyzed, the C/O ratio for the char increase for all fuels, as also observed in the literature [112, 122]. Again, the C/O ratio for EC char was found to be much higher than that of leached biomass char samples. C/O ratio for all ash samples was observed to be nearly equal. However, as discussed earlier, the C element percentage for EC ash sample is by far the lowest of all fuels indicating better burnout and its inorganic nature. This can also be observed from C element percentage for all fuels in **Figure 26(b)**.

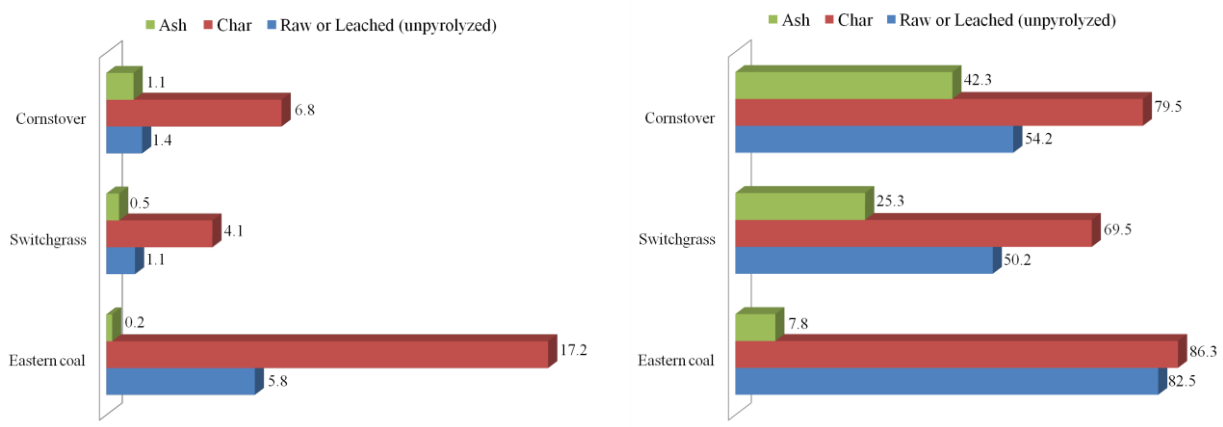

(a) (b)

Figure 26: (a) C/O ratio for EC, SG leach and CS leach samples in unpyrolyzed, char and ash states. (b) C% for EC, SG leach and CS leach samples in unpyrolyzed, char and ash states

4.3.3 Coal-biomass mixture interactions

Figure 27(a) shows the ESEM image for char generated from the pyrolysis of EC and SG Leached mixture (80:20 ratio) at 100X magnification. As observed from **Figure 27(a)**, no interaction or fusion was found between the individual fuel char generated from the mixture of two types of fuels. Both types of char samples can be identified separately with no apparent difference from their respective chars formed in their standalone runs. There was no fusion between coal and biomass particles despite fusion between coal particles.

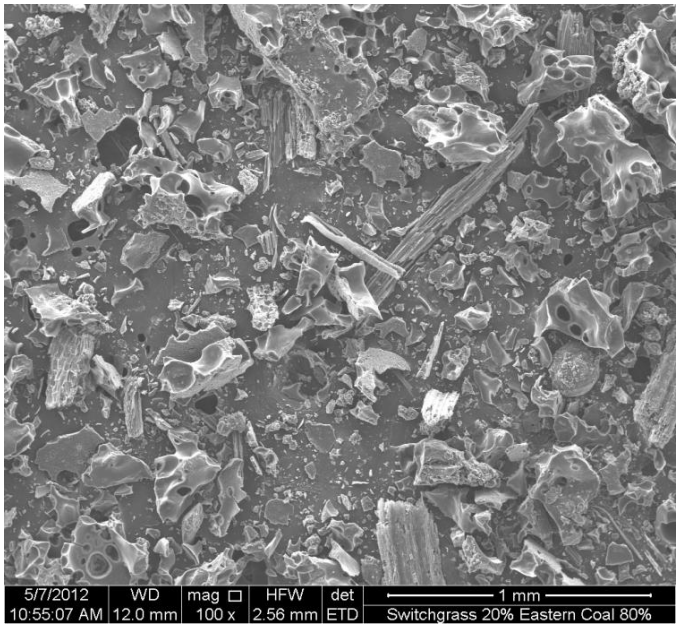

(a)

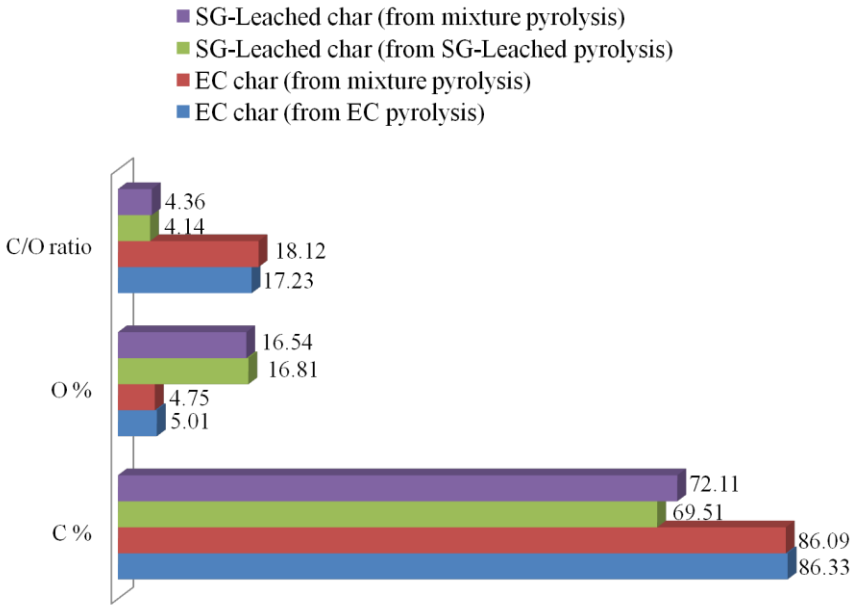

(b)

Figure 27: Effect of EC and leached SG biomass co-pyrolysis (a) SEM image of char from EC and SG-Leached mixture pyrolysis (b) C%, O% and C/O ratio of EC-char, SG-Leached char and char sample from co-pyrolysis of EC and SG-Leached sample in 80:20 mass ratio

Figure 27(b) shows the C%, O% and C/O ratio measured for EC-char sample, SG-Leached char sample and char sample formed by co-pyrolysis of EC and SG-leached sample. For the char sample from EC-SG mixture, the C%, O% and C/O ratio was separately evaluated for EC char and SG-Leached char particles found in the mixture char. From **Figure 27(b)**, the EC char sample formed from the coal-biomass mixture, and the char formed from the standalone pyrolysis of EC sample have similar C%, O%, and C/O ratio within an error margin of ±3%. In addition, the SG-Leached char samples from the mixture and standalone run have similar elemental composition within an error of ±1%. These results show that the interactions between coal and leached biomass sample on co-pyrolysis are minimal when mixed in 80:20 ratio, both from physical and chemical aspects. Similarly, no physical and chemical interactions were found for the EC and CS leached mixture co-pyrolysis test case.

4.4 Conclusions

The ESEM was used to analyze the physicochemical properties of the fuel, char and pyrolyzed ash samples. The effects of biomass water leaching on the physicochemical behavior of biomass fuels and coal-biomass fuel mixtures were also studied. A significant reduction in inorganic salts and increase in oxygen element percentage was observed due to biomass leaching, while the carbon element percentage was found to be unchanged following water leaching. Physicochemical property differences between coal and biomass samples were demonstrated in their un-pyrolyzed, char and ash phases. The physicochemical interactions between coal and leached biomass sample, following co-pyrolysis, were found to be minimal.

5. PYROLYSIS CHEMICAL KINETICS

5.1 Literature review

A thorough understanding of pyrolysis kinetics is imperative for the scaling of thermochemical conversion reactors [33]. The pyrolysis process of solid fuels is classified as heterogeneous reactions. However, it has been proven that Arrhenius kinetics satisfactorily describes the temperature dependence of the overall degradation constant for solid fuels such as biomass [123]. The debate on the applicability of Arrhenius kinetics for coal-biomass pyrolysis is out-of-scope of the present research and can be traced back elsewhere [33, 123, 124]. The current literature review discusses the coal, biomass and mixture kinetics, the tools to obtain kinetic parameters, and the dependence of kinetic parameters on operating conditions.

5.1.1 Pyrolysis process

Pyrolysis is a complex process that represents the first step for all thermochemcial conversion processes (combustion, gasification and pyrolysis). The pyrolysis process of solid fuels is briefly described below [22, 125, 126]. An excellent analysis of detailed pyrolysis process is mentioned elsewhere [127].

(i) Energy from the heat source increases the temperature of solid fuel.
(ii) Initiation of primary pyrolysis reaction leading to release of volatile matter and formation of char.
(iii) Internal convection of volatiles causing heat transfer between hot volatiles and cooler virgin fuel.
(iv) Condensation of vapors in the pores of un-pyrolyzed fuel causing formation of tar.
(v) Auto-catalytic secondary reactions between the volatile vapor, tar, and char at higher temperature.

The primary pyrolysis reactions are governed by the local solid fuel temperature. In case of biomass pyrolysis, the primary pyrolysis process results in several parallel and consecutive reactions signifying the decomposition of three major components (cellulose, hemicelluloses and lignin). The secondary reactions occur due to the interaction between solid fuel and hot vapors produced from primary reactions. The secondary reactions are generally auto-catalytic in nature. The auto-catalytic secondary reactions are difficult to predict and model because their

experimental information is difficult to obtain from standard tools. Besides, the secondary reactions are promoted due to other factors which includes increased residence time of volatiles in the reactor, larger fuel particle size causing higher temperature gradients and longer residence time of volatiles inside the solid fuel matrix [22, 128].

In the present work, the major focus is on primary pyrolysis reactions and other factors (particle size, residence time, alkali salts) will be controlled to reduce the occurrence of secondary reactions. The primary pyrolysis process is complex due to several consecutive and parallel reactions occurring in a very narrow temperature range. However, as discussed in the later sections, the pyrolysis behavior can be simplified in terms of global representative reactions.

5.1.2 Kinetics analysis approaches

Traditionally, the kinetic analyses of solid fuel pyrolysis were conducted in the literature through instruments using an isothermal heating approach. However, recently the interest in isothermal methods has waned because of the difficulty to map all temperature regimes using this method in comparison to non-isothermal techniques (e.g. constant heating rates) [129]. The two possible formats of non-isothermal data, that are commonly used to investigate pyrolysis kinetics, are the thermogravimetric (TG) data using a TGA or calorimetric data using DSC. The thermogravimetric data reports the mass loss of the pyrolysis sample, while the calorimetric data provides the energetic transitions in the samples with the application of a heating rate program. The TG data provides more accurate data and is commonly used for kinetics research. There is another approach of using differential TG (DTG) data for kinetics analysis, but this method is approximated due to the smoothing issues of DTG curves [31]. As per the International Confederation for Thermal Analysis and Calorimetry (ICTAC) directive, the non-isothermal data must be obtained at multiple heating rates to provide the most accurate kinetics data [130-134].

Various mathematical tools can be used to convert the non-isothermal TG data to kinetic parameters. These include model free methods (ASTM E698, Ozawa-Flynn-Wall analysis and Friedman analysis) and the non-linear regression method. The model free methods provide reasonably accurate data for the simple reactions which does not involve any complex reaction pathways (consecutive, parallel or independent reactions) [135]. On the other hand, the kinetic parameters obtained from non-linear regression analysis provide a best fit to the assumed kinetic

model, irrespective of the complexity of the kinetics involving multiple consecutive, parallel or independent reactions [136]. The majority of kinetics data for coal-biomass pyrolysis in the older literature has been obtained through model free methods [5, 35, 125]. The non-linear regression analysis is recently emerging as a more popular technique for accurate coal-biomass kinetics investigation [21, 32, 45, 118, 119, 137]. Some other studies have recently implemented a distributed activation energy model (DAEM) for the kinetic analysis of pyrolysis process [31, 116, 125, 138-144]. This model assumes an infinite number of irreversible 1^{st} order parallel reactions to generate a distributed activation energy function for complex reactions. However, the pre-exponential factor (frequency parameter) is considered to be constant for the temperature range. It has also been claimed that the application of DAEM model is not suitable for oxidative pyrolysis of biomass [143]. Inclusion of large number of parameters for kinetics analysis is another criticism of DAEM model [45]. The main advantage of DAEM is that it can give a more objective representation of activation energy for the real process [116, 140].

5.1.3 Biomass pyrolysis

Many authors have investigated biomass pyrolysis kinetics in various levels of details and the work done on this aspect is diverse. The below subsections discuss the biomass pyrolysis literature review from various aspects.

5.1.3.1 Slow and fast biomass pyrolysis

Pyrolysis can be classified as slow pyrolysis (heating rates of the order 10°C/min) and flash (fast) pyrolysis (heating rate 1000°C/min) [22]. Both types of pyrolysis have been experimentally investigated in the literature [145, 146]. The volatile matter residence time is shorter for fast pyrolysis, thus the pyrolysis kinetics is best described by primary reactions [147]. Milosavljevic *et al* [148] conducted both slow and fast pyrolysis tests, and concluded that the derived biomass kinetics parameters are sensitive to the heating rate of the experiments. The experiments with fast pyrolysis provided lower activation energy (140-155 kJ/mol) and those with slow pyrolysis gave higher activation energy (~220 kJ/mol). Many authors have noticed the activation energies of biomass pyrolysis falling into both of these two categories [147-149]. Milosavljevic *et al* [148] attributed the lower activation energy to the pyrolysis of biomass shells (surface layer) and the higher activation energy to the pyrolysis of the sample interior. The effect

of heating rate has also been observed in other aspects of pyrolysis. The char yield has often been found higher for slow pyrolysis [22, 24]. This is due to the reduction in pressure driven flows inside the sample increasing the volatile residence time, and thus promoting secondary reactions and formation of char. In addition, the increase of volatile formation for fast pyrolysis also promotes secondary reactions due to similar reasons [146].

5.1.3.2 Biomass pyrolysis process

The devolatilization temperature of lignocellulosic biomass materials is low in the range of 200-400°C. There are three main regimes of weight loss during the slow pyrolysis process, namely, moisture release, followed by hemicellulose and cellulose decomposition. The decomposition of lignin is over a wide temperature range and does not exhibit a specific peak value at any particular temperature [29, 145, 146]. Various researchers use the temperature recordings at the decomposition initiation, shoulder, peak and termination to characterize different biomass fuels [29, 146].

The pyrolysis of biomass deliver additive kinetics as those from the additive weight based ratio of biomass constituents. The deviations found, if any, are reported due to the presence of inorganic salts causing catalysis of the primary reactions [2, 19, 21-35, 145]. Thus, the interactions between decomposing cellulose, hemicellulose and lignin have been found to be negligible for slow pyrolysis studies [118, 141, 146].

5.1.3.3 Pretreatment effect on biomass pyrolysis

Water leaching is generally used to remove inorganic salts in biomass samples, thus decreasing the probability of the occurrence of secondary reactions during pyrolysis. However, it has been noticed that water leaching significantly affects the pyrolysis process by elevating the peak temperature and activation energy for the decomposition of each biomass constituent (cellulose, hemicellulose and lignin). The DTG peak for each component becomes more distinguished from another on water leaching. Also, the char yield decreases and volatile yield increases on water treatment [119-121]. Thus, water leached sample devolatilize at higher temperature, but at a faster rate, thus yielding a lower char and higher volatile percentages. The removal of inorganic salts (ash) increases the fixed carbon percentage, and thus increases the energy density of the fuel. All these factors together produce a desirable effect for the plant operation [121]. It has also

been reported that the biomass particle size has no significant effect on the TGA pyrolysis for the mean diameter smaller than 1 mm and initial sample mass less than 15 mg [146].

5.1.3.4 Models used for biomass pyrolysis

The biomass kinetic studies can be classified into three main groups, namely, one step global models, one-stage multi reaction models and two-stage semi global models [127]. A representation for these models is given in **Figure 28**. One step global models represent simplified biomass pyrolysis process. One-stage multi reaction models are used to describe the primary pyrolysis of fuel into char, gas and tar using independent parallel reactions. Two-stage semi global models are used when both primary and secondary reactions are present during pyrolysis [127]. The pros, cons and other details on application of these models on biomass pyrolysis are given elsewhere [127, 146].

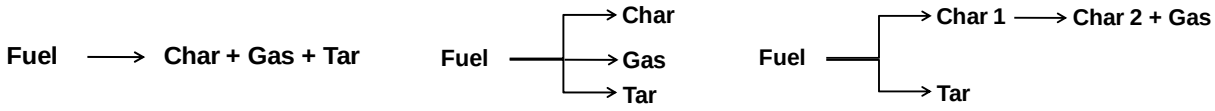

Figure 28: Types of decomposition models (a) One-step global model (simplified) (b) One-stage multi reaction model (primary reactions) (c) Two-stage semi global model (primary and secondary reactions)

Depending on the case, all three models have been satisfactorily applied for biomass and biomass constituent pyrolysis experiments. Kansa *et al*. [126] and Saddawi *et al*. [147] assumed that the 1st order global reaction is adequate to describe the decomposition of biomass into char and volatiles, neglecting the secondary reactions. Hashimoto *et al*. [32] used a single nth-order reaction model for biomass pyrolysis and successfully correlated it with the TG data. Cozzani *et al*. [21] assumed that each of the biomass constituents decompose into char and volatile matter through two independent parallel reactions (**Figure 29(a)**). The most popular model for primary pyrolysis reactions is the three independent parallel reaction model, in which each reaction corresponds to the weight loss of each biomass constituent [27, 29, 30, 118, 146, 150]. Teng *et al*. [119] included the fourth independent parallel reaction to account for the moisture release step. Although many models have been presented in the literature to account for the secondary reactions as shown in **Figure 29(b)-(d)**, the one presented by Shafizadeh [151] has been widely

accepted as the most appropriate and accurate representation of biomass pyrolysis. Most of these models are presented for cellulose pyrolysis, as the cellulose form the major weight proportion of biomass and for its kinetics being similar to that of hemicellulose [1].

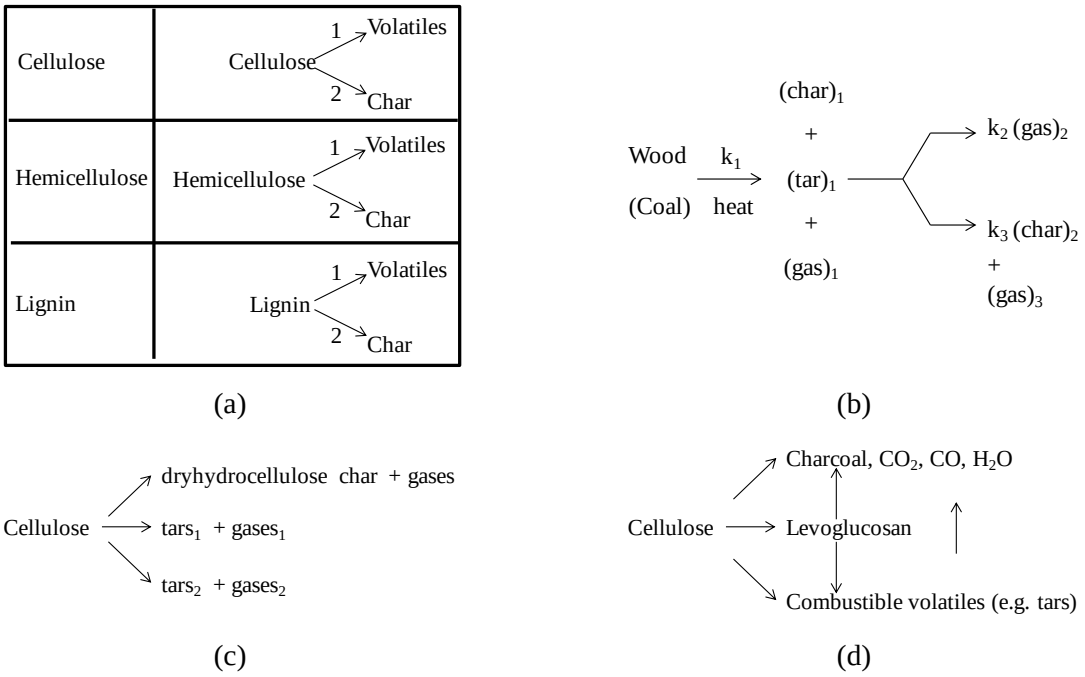

Figure 29: Biomass pyrolysis models (a) Cozzani *et al*. [21] (b) Kansa *et al*. [126] and Kanury *et al*. [152] (c) Milosavljevic *et al*. [148] (d) Shafizadeh [151]

5.1.4 Coal-Biomass co-pyrolysis

The devolatilization of coal is fundamentally different than biomass. Coal samples devolatilize with a single main weight loss step followed by a long tail of weight loss [153]. Coal samples devolatilize at temperatures much higher than biomass. The devolatilization of coal starts at about 400°C and it cannot be considered complete even at temperatures as high as 1000°C due to the long tail of weight loss. Thus, the pyrolysis duration of coal is much longer than biomass and occurs at higher temperatures as well [45]. The pyrolysis char yield of coals is much higher and volatile yield is much lower in comparison to biomass. The devolatilization rate (weight loss rate) of biomass particles is also higher than that of coals [19]. The difference in devolatilization rate is due to the bond structure of biomass and coal fuels. The lignocellulosic biomass constituents are linked with relatively weak ether bonds (bond energy of 380–420 kJ/mol) that break at low temperature range. The coal structure is made of dense polycyclic aromatic

hydrocarbons which are linked by alternate single and double bonds with extra resonance stability. Thus, coal samples are more resistant to thermal decomposition and have higher bond energy (1000 kJ/mol) [45]. Thus, the activation energy for coal pyrolysis is also higher than that of biomass [46].

Bradley *et al*. [34] investigated the kinetics of co-pyrolysis of coal biomass mixture. The kinetic model was developed to simulate the weight loss profile of mixture based on its C, H and O molar ratios. However, it was concluded that it was not possible to develop a co-pyrolysis model based on such approach.

Sadhukhan *et al*. [45] developed a kinetic model based on parallel reactions to analyze the coal-biomass pyrolysis using a TGA. The blended samples were prepared with coal and biomass ratios of 100:0, 50:50, 40:60, 10:90, and 0:100, respectively. The analysis of mass loss data of mixtures and individual fuels showed a lack of interaction between the coal and biomass samples. The kinetic parameters of the blend were also found to be similar to those of the respective individual samples. The residual char mass fraction of coal biomass blend was also found to be additive of the weight average values of individual coal and biomass samples.

A similar conclusion was derived by Biagini *et al*. [37], where the primary reactions for thermal decomposition of coal and biomass were found to be independent of each other. The TG curve of the coal-biomass blend was determined to lie between those of individual samples and as the weighted profile of the two fuels. The primary reactions of biomass were not found to be significantly affected by those of coal due to the difference in the devolatilization temperatures. The differences in the devolatilization temperature of coal and biomass lead to the absence of volatile species from one fuel component during the pyrolysis of the other. At lower temperatures, the blend behavior was found to be similar to that of biomass and at higher temperature the weight loss was governed by coal TG profile. Similar conclusions have been derived in various other studies [41-44, 46].

However, interactions between coal and biomass samples have also been noticed in the literature. Ulloa *et al*. [154] co-pyrolyzed an equal weight ratio blend of coal and pine-sawdust at multiple heating rates. Interactions in the blend indicated higher than expected volatile yield. The interactions were attributed to the secondary reactions between coal and biomass vapors at temperatures above 400°C. Similarly, interactions were found between the coal and sawdust blends prepared by Park *et al*. [19], revealing higher than expected char yield of the blend. This

time an additional weight loss step was observed at 700°C for the blend. A difference in weight loss rate for the blends was also observed, in comparison to individual samples. Park *et al*. [19] attributed these interactions to the presence of excess hydrogen donors in the volatile matter from sawdust, because the molar H/C ratio of sawdust is twice as higher than that of coal. Park *et al*. [19] also attributed these interactions to the difference in heat transfer characteristics of coal and biomass. It was suggested that since the heat transfer through coal is lower than biomass, the uneven temperature distribution in the blend may cause longer residence of vapor inside the blend, thus causing secondary reactions.

Folgueras et. al. [38] found an additive behavior for 50% weight based coal and sludge blends in oxidative atmosphere, where the decomposition reactions were found to be independent for both samples. Fermoso *et al*. [47] pyrolyzed coal-chestnut and coal-olive blends in 70% N_2 and 30% steam atmosphere. The blend ratio was 70% coal and 30% biomass for the two samples. No significant interactions were observed for the coal-chestnut blends; however, deviations from the additive behavior were found for the coal-olive blend.

5.2 Experimental procedure

The materials used in this research and their preparation method is described in Section 4.2.1. A NETZSCH 449 F1 Jupiter STA was used to characterize the gravimetric (TGA) response of fuels during pyrolysis. Experiments were conducted in an inert atmosphere to avoid oxidation reactions during heating. For this purpose, the furnace was vacuumed and refilled with 99.999% pure nitrogen two times before analysis. Nitrogen flow rate of 80 ml/min was maintained during the analysis. The fuel samples were tested in the mass range of 4.5 to 5.5 mg. The initial and final sample mass was measured with a ±0.01 mg accuracy balance. The tests were carried out from 298 K up to temperatures sufficiently above the pyrolysis temperature of the fuels at atmospheric pressure (1073 K). To determine the Arrhenius kinetic parameters of fuel pyrolysis, the STA tests were conducted at 5, 10, 20 and 40 K/min heating rates. A five minute residence time at 1073 K was provided to all the experimental and sample preparation (char and ash) runs conducted in this study. The tests were conducted multiple times to ensure repeatability. The kinetic model parameters were obtained by non-linear regression analysis on TGA data using the NETZSCH Thermokinetics software. The STA experimental procedure and its calibration methodology have been explained in a previous publication [155].

5.3 Results and discussion

The effects of leaching biomass and blending biomass and coal were evaluated through the use of thermogravimetric analysis (TGA). The thermogravimetric (TG) and differential TG (DTG) data for fuels and blends were measured at different heating rates and used to quantify kinetic parameters.

5.3.1 Gravimetric response of fuels

Figure 30 shows the TG and DTG signals for the pyrolysis of untreated and water leached SG samples at the heating rate of 20 K/min. The devolatilization temperature of biomass samples was found to be low in the range of 200-400°C. As observed from **Figure 30**, the biomass samples are comprised of a high amount of volatile mass with almost 80% of the sample decomposing during the pyrolysis process. Despite the wide variety of biomass feedstocks, biomass as a lignocellulosic material mainly consists of three major constituents, cellulose (30-60%), hemicellulose (20-35%) and lignin (15-30%) [1, 3, 6]. As shown in **Figure 30**, there are three main regimes of weight loss during the pyrolysis process, which are associated with the decomposition of these three major components. Hemicellulose decomposition occurs initially (at 312°C for the SG-Raw sample) followed by cellulose decomposition (at around 365°C for the SG-Raw sample). The pyrolysis of lignin occurs over a wide temperature range and did not exhibit a specific peak value at any particular temperature.

From **Figure 30**, it is noticed that the water leaching significantly affects the peak temperature for the decomposition of biomass constituents (hemicellulose elevated by 13.5ºC and cellulose by 1.1ºC in the case of SG). The char yield decreased (from 19.4% to 14.5% in case of SG) and volatile yield increased due to water treatment [119-121]. This was primarily due to removal of alkali salts during water leaching process and decrease in the secondary reactions during pyrolysis due to the same reason. This decrease in char yield was also accompanied by an increase in the peak decomposition rate of hemicellulose (about 1.5%) and cellulose (about 2.5%) constituents of the SG sample. Thus, water leached samples devolatilized at higher temperatures but at a faster rate, resulting in lower char yield. A similar observation was made for leaching of CS samples, where the char amount decreased from 22.4% to 13.7% on water leaching. The hemicellulose decomposition temperature increased from 311°C to 323°C and cellulose decomposition temperature increased from 354°C to 362°C. Although CS

leaching resulted in an increase in the peak rate of cellulose decomposition (from -16.9% to -23.7%), the hemicellulose peak decomposition rate increased by only 0.55%.

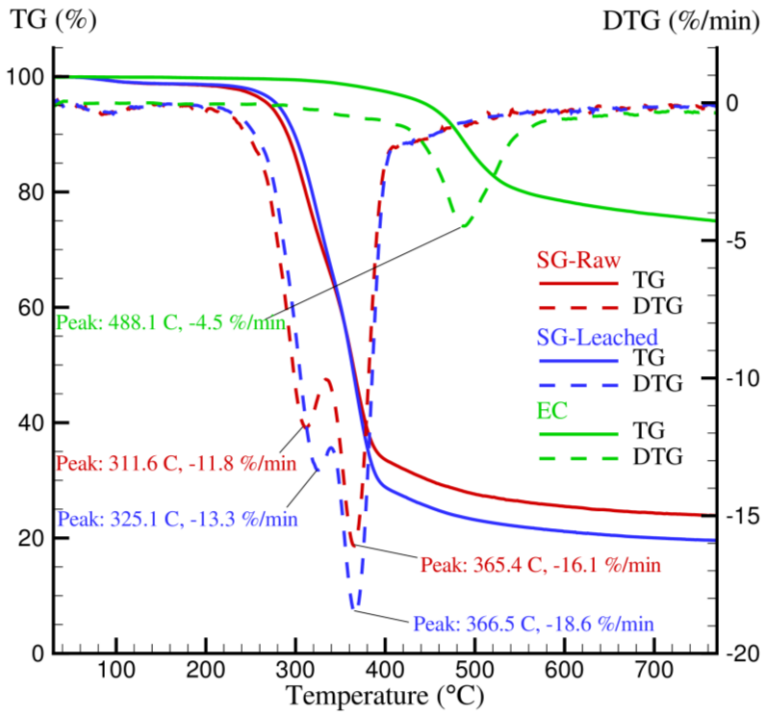

Figure 30: TG and DTG analysis of fuel pyrolysis at 20 K/min heating rate: SG-Raw, SG-Leached and EC samples

The gravimetric signals of the EC sample is also shown in **Figure 30**. The pyrolysis of EC is fundamentally different than SG-Leached biomass sample. EC devolatilized with a single main weight loss step followed be a long tail of weight loss . The devolatilization of EC starts at about 400°C and it cannot be considered complete even at temperatures as high as 800°C due to char gasification at higher temperatures. Thus, the pyrolysis duration of coal is much longer than biomass and occurs at higher temperatures as well. The pyrolysis char yield of coal was measured to be 74.7%, which is higher in comparison to the char yield of biomass samples (e.g., SG-leached 14.5%). In addition, the devolatilization rate of SG biomass particles was also found to be higher than that of EC. The difference in devolatilization rate is due to the difference in bond structure of biomass and coal fuels. The lignocellulosic biomass constituents are linked with relatively weak ether bonds (bond energy of 380–420 kJ/mol) that break at low temperature range. The coal structure is made of dense polycyclic aromatic hydrocarbons which are linked by

alternate single and double bonds with extra resonance stability. Thus, coal samples are more resistant to thermal decomposition and have higher bond energy (1000 kJ/mol) [45].

Figure 31 shows the gravimetric signals for the pyrolysis of 80:20 fuel mixture of EC and SG-Leached samples. At the tested mixture ratio and inert environment conditions, the coal-biomass fuel mixture decomposed as the sum of its constituents. The DTG peaks for decomposition of hemicellulose, cellulose and EC are apparent from the coal-biomass fuel mixture pyrolysis and located approximately at the same temperature as the peak temperatures of individual sample runs. The TG profile of a simulated weighted sum run for EC and SG-Leached sample in 80:20 ratio was generated from their individual gravimetric data. The simulated weighted sum TG profile matched sufficiently with the TG profile of the EC and SG-Leached fuel mixture. Thus, the mixture of EC and SG-Leached biomass sample delivered an additive thermogravimetric data during pyrolysis.

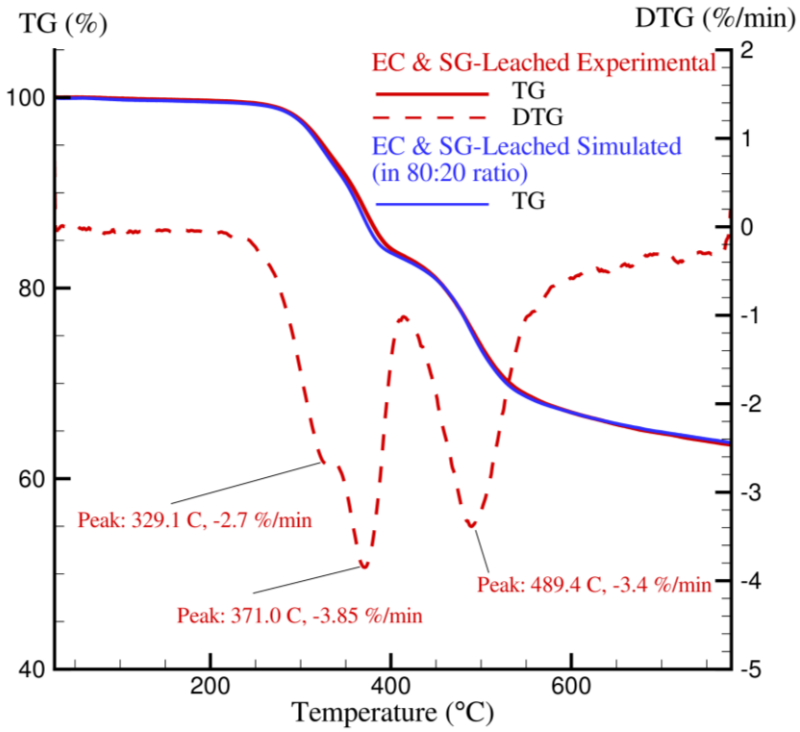

Figure 31: TG and DTG signals for pyrolysis of EC-SG-Leached mixture (80:20 by mass)

5.3.2 Model development and kinetic parameters

The biomass kinetic models can be classified into three main groups, namely, one step global models, one-stage multi reaction models and two-stage semi global models [127]. Depending on the fuel, all three models have been satisfactorily applied for biomass pyrolysis experiments *viz.* one step global models [32, 126, 147], one-stage multi reaction models [21, 29, 146] and two-stage semi global models [151].

The most popular model for biomass primary pyrolysis reactions is the three independent parallel reaction model, in which each reaction corresponds to the weight loss of each biomass constituent [21, 29, 146]. In the current study, as per the analysis from the Section 5.3.1 for the biomass samples, it was found that the hemicellulose, cellulose and lignin constituents pyrolyzed independently irrespective of its pretreatment with water. Hence, the three nth order independent parallel reaction model was selected to represent the pyrolysis of each biomass constituent. **Figure 32(a)** and **Figure 32(b)** shows the TG data at multiple heating rates for CS-Raw and CS-Leached samples respectively. **Figure 32** also shows the selected model kinetic fit for these TGA runs using the non-linear regression analysis. As observed from the **Figure 32**, the three independent nth order parallel reaction model fits satisfactorily with the TGA data. The non-linear regression analysis was also conducted for several other kinetic models mentioned in this section, and fits were compared statistically using the F-test. The three nth order independent parallel reaction model was found to be statistically best fit model for the biomass TGA data. The hemicellulose and cellulose decomposition peak temperatures also matched for the TGA and the fitted kinetic model. Similar results were obtained for the SG-Raw and SG-Leached biomass samples.

Table 8 reports the kinetic fit parameters for the four biomass samples tested in the study.

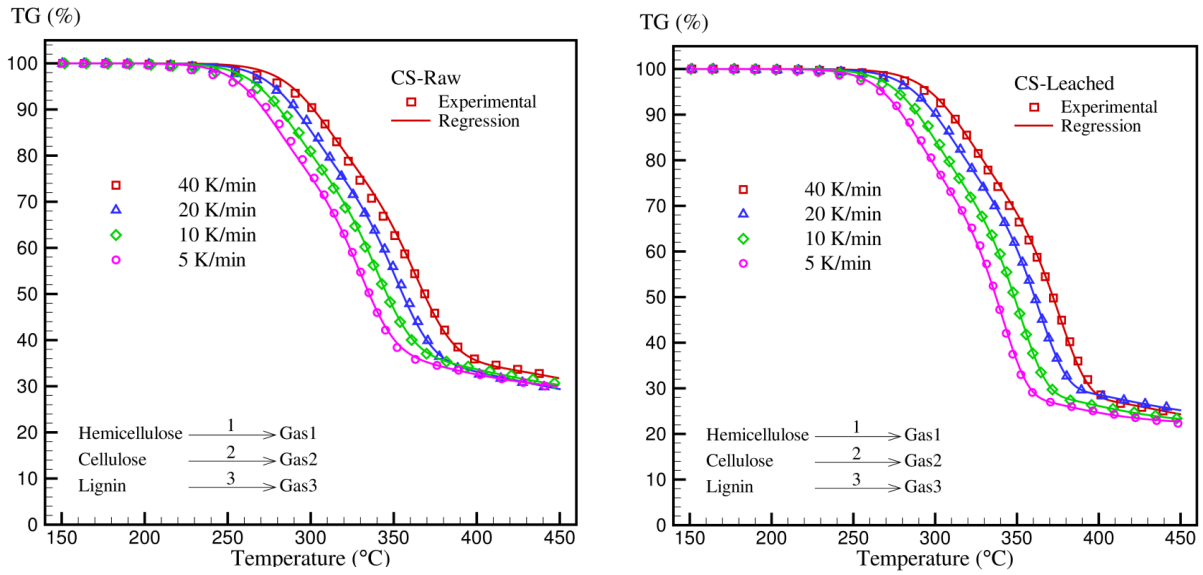

Figure 32: TG runs at multiple heating rates and kinetic fit estimation for biomass samples using non-linear regression (a) CS Raw (b) CS-Leached

Table 8: Kinetic parameters for pyrolysis of biomass and EC samples

Parameters	SG - Raw	SG - Leached	CS - Raw	CS - Leached	EC
log A_1 (s^{-1})	13.35	13.22	14.42	14.77	10.88
Ea_1 (kJ/mol)	166.02	167.51	175.66	182.58	155.56
n_1	2.00	2.00	2.00	2.00	3.00
log A_2 (s^{-1})	14.34	14.50	14.60	14.25	13.83
Ea_2 (kJ/mol)	195.75	198.79	195.01	194.41	227.49
n_2	1.10	1.01	1.29	.94	3.00
log A_3 (s^{-1})	7.35	7.64	6.12	6.49	-
Ea_3 (kJ/mol)	123.95	127.92	108.98	111.87	-
n_3	2.00	2.00	2.00	2.00	-
Fr. Mass $Loss_1$	.42	.42	.34	.34	.14
Fr. Mass $Loss_2$	.45	.47	.51	.54	.86
Fr. Mass $Loss_3$	.13	.11	.15	.12	-

For the biomass samples, the subscripts '1', '2' and '3' represents the reactions concerning the decomposition of hemicellulose, cellulose and lignin into gases respectively. The pre-exponential factor (A), activation energy (Ea) and reaction order (n) for each of these three decomposition reactions was obtained using non-linear regression analysis. The parameters named 'Fr. Mass Loss' represents the fraction of mass lost from the initial fuel mass due to each constituent decomposition reaction. As observed from **Table 8** and also confirmed from the DTG data in **Figure 30**, the maximum mass loss of the biomass sample is contributed by cellulose decomposition and the minimum mass loss is contributed by the lignin decomposition reaction. This is consistent with the decomposition behavior of these individual constituents in the literature, where the lignin component has been identified as the major char contributor in biomass pyrolysis [22]. It was also observed that the major impact of water leaching was on the contribution from cellulose decomposition, which increased for both biomass samples (SG and CS) due to the removal of alkali salts and secondary reactions from the pyrolysis process. The increase in decomposition fraction of cellulose due to leaching was countered by reduced contribution from lignin, whereas the fraction of hemicellulose decomposition remained nearly the same. Thus, higher decomposition of cellulose and lower contribution of lignin resulted in lower char amounts for biomass samples after leaching. It is also noted from the **Table 8** that the CS sample contains a higher amount of cellulose and a lower amount of hemicellulose compared with SG. The lignin amount is nearly same for both biomass samples. A similar observation was made by Radmanesh *et al*. [146] for beechwood and rice husk biomass samples, where cellulose and hemicellulose were identified as the major contributor to the fuel mass loss during pyrolysis.

Table 8 also reports the Arrhenius kinetic parameters for biomass pyrolysis. As noted from **Table 8**, the activation energy for hemicellulose decomposition is found to be lower than that of cellulose, thus indicating earlier decomposition temperature for hemicellulose. The activation energy and pre-exponential factor are noted to be the lowest for lignin decomposition reaction. No kinetics literature data was found for the SG and CS pyrolysis using three independent parallel reaction model. The activation energy and pre-exponential factors for three independent reactions were found in agreement with those reported by Koufopanos *et al*. [156] and Cozzani *et al*. [21] for wood samples. Although, the calculated hemicellulose and cellulose pyrolysis Arrhenius parameters also matched reasonably with some other studies reported in the literature [118, 119, 146], the literature lignin decomposition activation energy and pre-

exponential factors [118, 119, 146] were found to be significantly lower than those determined in the current study. However unlike the current study, these studies [118, 119, 146] assumed the order for all the independent decomposition reactions to be constant at 1 while implementing the regression analysis. In the current study, an increase in the activation energy (1-7 kJ/mol) has been observed for all biomass constituents on water leaching.

Similarly, EC sample pyrolysis runs were evaluated at multiple heating rates using the non-linear regression analysis. Various kinetic models were tested, including one global reaction model, one-stage multi reaction models and two-stage semi global models mentioned in the literature [127]. The statistical best fit to the kinetic data was obtained using a two nth-order independent parallel reaction model. The model fit to the TG data for EC sample is shown in **Figure 33(a)** and the Arrhenius parameters are reported in **Table 8**. The model predicts the first decomposition step takes place at a lower temperature range of 300-400ºC accounting for 14% of the total mass loss during the pyrolysis. The rest of the 86% of mass loss is due to a higher activation energy primary step occurring from 400 ºC until the end of pyrolysis temperature. The primary step activation energy of EC sample (227.5 kJ/mol) was found to be higher than that of biomass samples (195-198 kJ/mol), thus owing to the higher bond dissociation energy of coals in comparison to biomass [45, 46]. The DTG peak obtained from the kinetics model for EC primary step also matched that of the TG data.

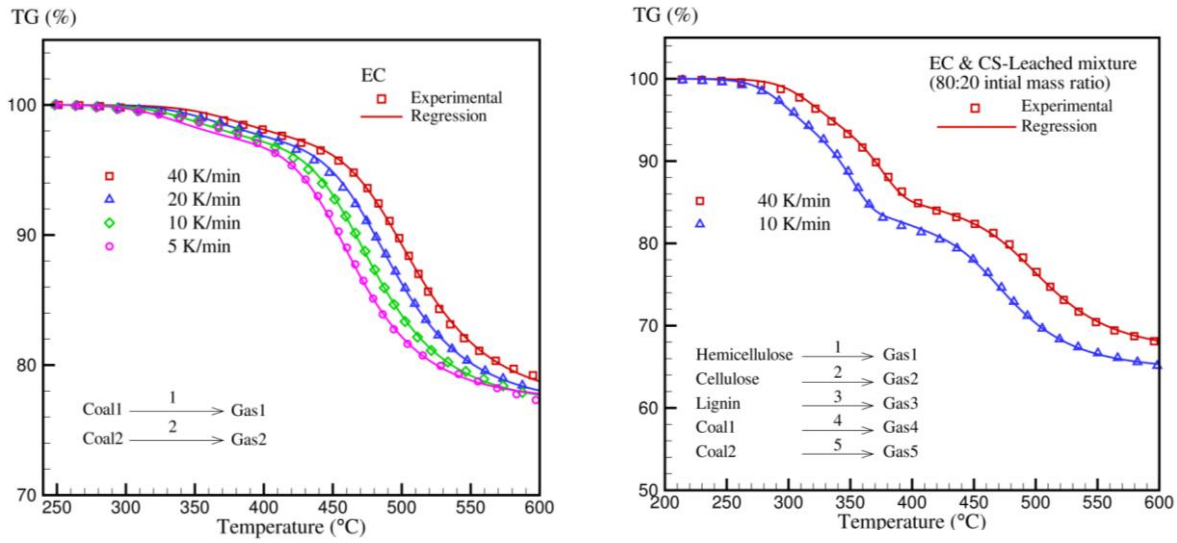

Figure 33: TG runs and kinetic fit estimation for fuel samples (a) EC with three nth order independent parallel reaction model (b) EC & CS-Leached mixture at 80:20 initial mass ratio using five nth order independent parallel reaction model

The physicochemical and TG-DTG analysis of co-pyrolysis of coal-biomass mixture samples indicate minimal interaction between the two types of fuels. As a result, an additive kinetic model was used for the coal-biomass co-pyrolysis. A five nth order independent parallel reaction model was selected for coal-biomass co-pyrolysis. The first three independent reactions simulated those regarding to hemicellulose, cellulose and lignin decomposition in biomass. The last two reactions corresponded to the decomposition of EC sample. The Arrhenius kinetic parameters (A, Ea and n) reported in **Table 8** were used in the five independent reaction model of coal-biomass mixtures, and the 'Fr. Mass Loss' term for each independent reaction was obtained using regression analysis. The fractional mass loss terms for all five reactions were found to be within ±15% to that reported in **Table 8**, when accounting for EC and biomass mixtures in 80:20 ratio. The resulting regression fit for the five independent reaction model was found to be in good agreement with the TG data for the coal-biomass mixture, as shown in **Figure 33(b)**.

Thus, EC and leached biomass mixtures, when pyrolyzed in 80:20 mixture ratio, exhibited weighted additive devolatilization behavior. However, interactions between coal and biomass samples have been noticed in the literature for higher biomass ratio in the mixture, e.g. 50:50 ratio [154] and 60:40 ratio [19] coal-biomass mixtures. Park *et al*. [19] attributed these interactions to the presence of excess hydrogen donors in the volatile matter from biomass, and also to the difference in heat transfer characteristics of coal and biomass fuels causing secondary reactions.

5.4 Conclusions

The focus of this chapter was to characterize the samples based on its kinetic parameters using thermal analysis of the fuel undergoing devolatilization. The effects of biomass water leaching on the kinetics of biomass fuels and coal-biomass fuel mixtures were also studied.

The water leaching of biomass samples mitigated the secondary reactions during pyrolysis, shifted the primary decomposition reactions to higher temperatures, and reduced the char yield of biomass fuel samples. An increase in the rate of devolatilization was noticed on biomass water leaching due to removal of secondary autocatalytic reactions.

An independent parallel reaction model of three n^{th} order reactions best described the biomass pyrolysis statistically, where each reaction signified the pyrolysis of a biomass

constituent viz. hemicellulose, cellulose and lignin. A small increase in the activation energy of each constituent pyrolysis reaction was found on water leaching. Coal pyrolysis was statistically best represented by a two independent nth order reaction model. It was found that the co-pyrolysis of coal and leached biomass fuel mixtures exhibited a weight additive thermogravimetric and kinetic behavior, when pyrolyzed on an 80:20 initial mass proportion.

6. PYROLYSIS AND COMBUSTION ENERGETICS[3]

6.1 Literature review

Predicting the thermal response of solid fuels undergoing pyrolysis and combustion has historically been of primary interest in the areas of energy recovery and gasification applications. Proper knowledge of the energetic response of such fuels is needed in order to optimize and predict gasifier performance. The energetic parameters of a fuel undergoing pyrolysis-combustion includes the amount of heat required to pyrolyze the fuel (heat of pyrolysis and heat of gasification) and the amount of heat generated by the fuel upon combustion (heat of combustion). Hence, a methodology needs to be developed for an accurate energetic characterization of fuel mixtures undergoing thermochemical conversion processes.

The co-firing of multiple fuels, such as coal and biomass mixtures, has emerged as an alternative fuel route to improve the economics, environmental impact and performance of gasifiers. Efforts have been directed in the literature towards realizing efficient coal-biomass co-firing [13, 46, 51, 53, 54, 59]. However, problems related to co-firing of fuel mixtures are less understood due the intricate pyrolysis and combustion behavior of multiple fuels. Moreover, the energetic characterization of coal-biomass mixtures is not as well understood as the other aspects of their pyrolysis process *viz.* kinetics [34, 38, 45, 147, 151]. This is primarily attributed to lack of validated pyrolysis energetics models and consistent experimental methodologies for the accurate energetic characterization of solid fuels [155]. The reactivity of a fuel requires a total energy balance on the fuel, which includes the energy required for pyrolysis of the material as well as the heat released from combustion of the evolved gases and char. A method was developed to quantify energy for pyrolysis of materials using thermogravimetric analysis (TGA), differential scanning calorimetry (DSC), and a pyrolysis model [155]. The approach was validated with liquid chemicals, plastics, and composite materials, and is noted in the reference [155]. Recently, a micro-scale combustion calorimeter (MCC) has been developed to measure the heat release rate from milligram size samples as a function of temperature [157]. This has also primarily been used on plastic materials and has not considered the effects of energy required for pyrolysis in the evaluation of fuels.

[3] A significant part of this chapter is published in *Method for Measuring the Standard Heat of Decomposition of Materials*, Gaurav Agarwal, Brian Lattimer, *Thermochimica Acta*, Volume 545, Issue 0, October 2012, Pages 34-47, *Used with permission of Elsevier, 2013*

Research has also been performed on the effects of biomass water leaching on the energetics of biomass fuels and coal-biomass fuel mixtures. The water leaching process removes most of the inorganic salts from the biomass samples [25, 26, 119-121]. The removal of inorganic salts increases the fixed carbon percentage, and thus increases the energy density of the fuel. The removal of these salts reduces the drawbacks of biomass gasification operation problems associated with fouling, slagging and corrosion [6, 112, 114]. All these factors together produce a desirable effect for the plant operation [121]. However, the co-pyrolysis energetics behavior of leached biomass with coal has not been thoroughly investigated in the literature [115].

The focus of this section is to present a methodology to quantify the energetic response of biomass, coal, and coal-biomass blends. Different than much of the previous work, these materials have significant char that must be accounted for in the analysis to obtain correct property values and accurate prediction of coal-biomass mixture behavior. A method is presented to quantify energy to decompose samples from a simultaneous thermogravimetric analyzer (STA) that includes a TGA and DSC. In addition, an approach is presented on quantifying the heat of combustion of these charring materials based on the temperature dependent heat release rate from the MCC. These methods are used to determine the energetic properties of coal, biomass and coal-biomass blends. An approach is then presented on predicting properties of coal-biomass blends from individual material properties.

6.2 Experimental procedure

The materials used in this chapter and their preparation method is discussed in Section 4.2.1. A NETZSCH 449 F1 Jupiter STA (**Figure 34(a)**) was used to characterize the gravimetric (TGA) and energetic (DSC) response of fuels during pyrolysis. Experiments were conducted in an inert atmosphere to avoid oxidation reactions during heating. For this purpose, the furnace was vacuumed and refilled with 99.999% pure nitrogen two times before analysis. Nitrogen flow rate of 80 ml/min was maintained during the analysis. The fuel samples were tested in the mass range of 4.5 to 5.5 mg. Pt-Rh cups with lids (two holes) were used for these experiments. The initial and final sample mass was measured with a ±0.01 mg accuracy balance. The tests were carried out from 298 K up to temperatures sufficiently above the pyrolysis temperature of the fuels at atmospheric pressure (1073 K). The sample heating rate was kept constant at 20K/min. A five

minute residence time at 1073 K was provided to all the experimental runs conducted in this study. The tests were conducted multiple times to ensure repeatability. The STA experimental procedure and its calibration methodology has been explained in reference [155].

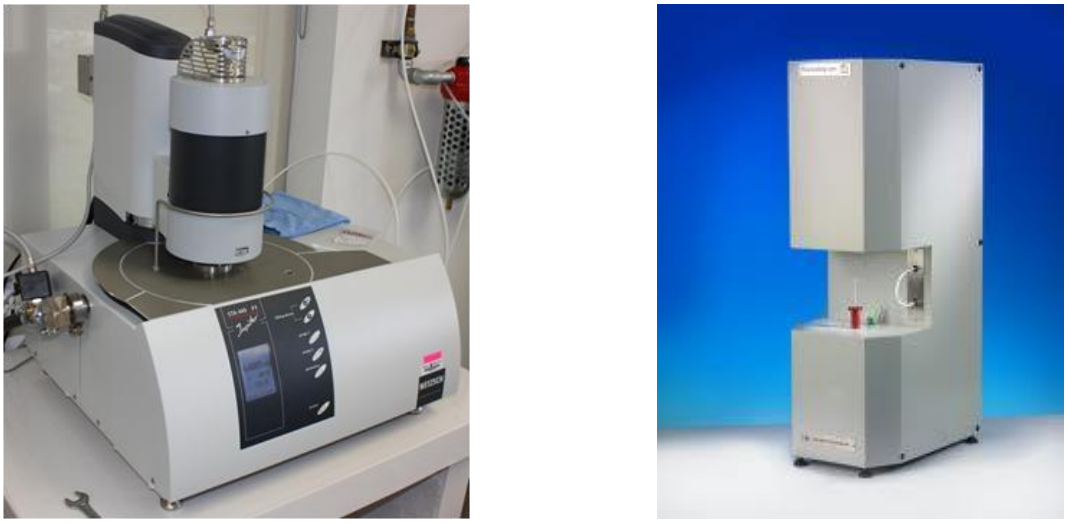

(a) (b)

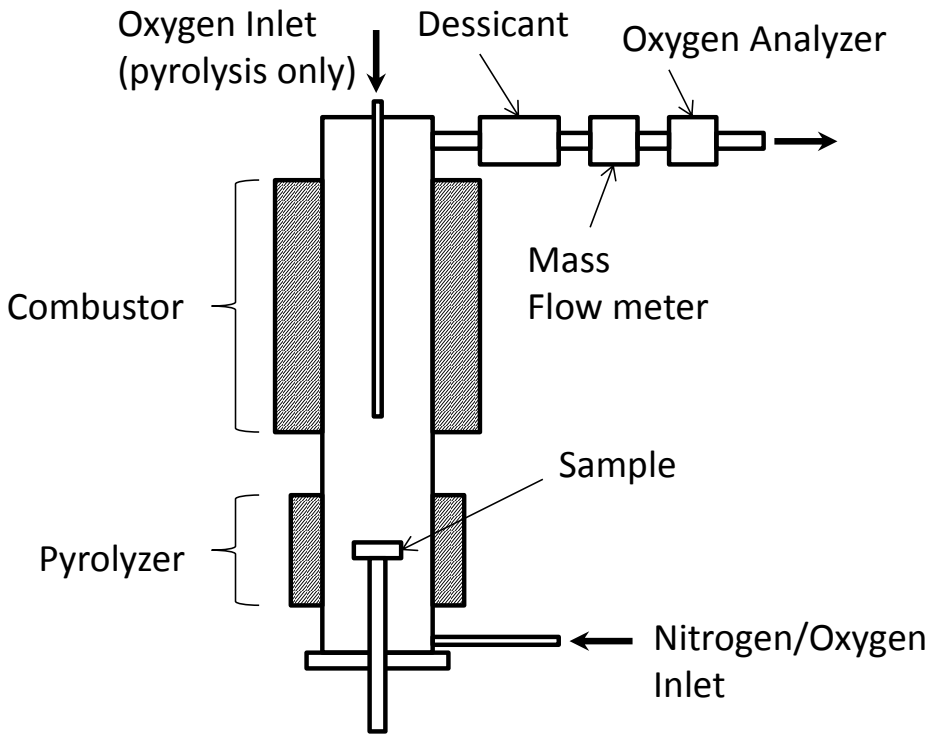

(c)

Figure 34: Instruments for energetic properties (a) STA (b) MCC (c) MCC schematic

A micro-scale combustion calorimeter (MCC) was used to quantify the heat release rate (HRR) from the combustion of the gases produced during the pyrolysis process, and heat release rate from the char combustion. A MCC is used by Federal Aviation Administration (FAA) to determine flammability characteristics for plastics and other composite materials used in the Aviation industry, and is carried out by ASTM D7309 [158]. A few modifications were made to this ASTM standard [158] to in order to test coal and biomass fuels in the current study. One of the main changes was to use the same Pt-Rh cups and lids (with two holes) as were used for the STA experiments. This change allowed the DTG and DSC peaks obtained from the STA experiments, and the HRR peaks obtained from the MCC experiments to be at the same temperature points. Other changes included the reduction in gas flow rates (N_2 and O_2) to get optimal accuracy from the HRR signals due to relatively low volatility of coal-biomass samples in comparison to plastics and composites.

For pyrolysis gas combustion, an 44 ml/min flow rate of nitrogen purge was used to pyrolyze the fuel samples at 20 K/min heating rate. The gases produced during the pyrolysis of fuels were instantaneously combusted in an oxygen atmosphere of 10 ml/min at 900ºC, as shown in Eqn. (5). The resultant data was used to calculate the heat of combustion for pyrolysis gas of the fuel, $\Delta h_{comb,p}$.

$$Fuel \xrightarrow{N_2,\Delta 20K/\min} Char + gas \xrightarrow{O_2,900°C} CO_2 + H_2O \quad (5)$$

The principle of oxygen consumption calorimetry was then used to calculate the HRR of the solid fuel during pyrolysis, after the correction for baseline drifts. The resultant heat release rate provided the measurement of heat output as a function of temperature per initial weight of the solid fuel.

Similar procedure was applied for char combustion experiments. A fuel char sample was kept on the sample carrier, and then oxidized at 20K/min atmosphere in 18.5% O_2 environment. The 18.5% O_2 atmosphere was selected due to the limitation of the STA instrument in producing up to 20.95% O_2 atmospheres. Thus, to keep the oxidation environment common in both setups, an 18.5% O_2 environment was selected for char oxidation. The remnant gas was completely oxidized in the combustor set at 900ºC, as shown in Eqn. (6). The resultant data was used to calculate the heat of char combustion, $\Delta h_{comb,cc}$.

$$Char \xrightarrow{18.5\%O_2,\Delta 20K/\min} Ash + gas \xrightarrow{O_2,900°C} CO_2 + H_2O \quad (6)$$

The MCC experimental procedure, calibration and apparatus description is provided elsewhere [157]. The sample preparation method and the temperature program were the same as that used in the STA analysis.

6.3 Energetic models

Heat of pyrolysis, Δh_{pyr}, heat of gasification, Δh_{gas}, heat of pyrolysis gas combustion, $\Delta h_{comb,p}$, heat of char combustion, $\Delta h_{comb,cc}$, and effective total heat of combustion, Δh_{comb}, were the energetic properties determined in the current study. A brief description of models and property determination procedure is provided below.

6.3.1 Pyrolysis model

The fuel pyrolysis mathematical model, its derivation, validation and application onto chemicals, polymers and composites is shown in reference [155]. In this section, the pyrolysis model relevant to calculating the heat of pyrolysis and heat of gasification for fuel samples is discussed in brief.

The heat of pyrolysis is defined as the difference of heat of formations of pyrolysis gas and the active solid material. Hence, the heat of pyrolysis is positive for an endothermic decomposition process. The heat of gasification is defined as the amount of energy required to vaporize a unit mass of volatile matter in the solid material, originally at the ambient temperature. The heat of gasification can be calculated for solid fuels as the sum of sensible heat required to raise the material temperature and the latent heat of pyrolysis, as shown in Eqn. (7) [155].

$$\Delta h_{gas} = \Delta h_{sen} + \Delta h_{pyr} \quad (7)$$

Many studies in the literature have calculated the heat of pyrolysis of materials using the STA instrument. In these studies, the heat of pyrolysis was calculated as the area difference between the apparent and sensible specific heat capacity curves, $\Delta h_{area,DSC}$, or as the area difference under the apparent and specific heat flow DSC curves [24-26, 159-166]. This calculation method of $\Delta h_{area,DSC}$ is shown in Eqn. (8) [155].

$$\Delta h_{area,DSC} = \int_{T_{in}}^{T} c_{app} d\theta - \int_{T_{in}}^{T} c_{sen} d\theta \quad (8)$$

In recent publication [155], it was validated and concluded that the heat of pyrolysis is different from the area difference under the apparent and sensible specific heat curves, or area difference under the apparent and sensible heat flow DSC curves for the degradation of a charring material. Unlike $\Delta h_{area,DSC}$, the heat of pyrolysis, Δh_{pyr}, is defined on the basis of per unit volatile mass lost, and can be calculated by applying the STA data onto a pyrolysis mathematical model [155]. Alternatively, it was proved that the Δh_{pyr} can be calculated for charring samples by using the $\Delta h_{area,DSC}$ data, and then accounting for the loss of volatile mass by implementing Eqn. (9) [155].

$$\Delta h_{pyr} = -\Delta h_{area,DSC} / \ln\left(Y_c\right) \quad (9)$$

In Eqn. (9), Y_c represents the final char yield of the fuel sample at the end of pyrolysis. Equation (9) also complies with the findings in literature [24-26, 159, 160] where the $\Delta h_{area,DSC}$ values were calculated for different fuels, and were found to be dependent on the final char yield of the fuel sample. The heat of gasification value, Δh_{gas}, is calculated by adding the sensible heat to and the heat of pyrolysis (Eq. (7)). Similar to Δh_{pyr}, the Δh_{gas} property is calculated on per unit volatile mass loss basis [155].

6.3.2 Combustion model

The heat of combustion is defined as amount of heat released from the combustion of volatiles released during the solid fuel pyrolysis [167]. MCC data was analyzed by calculating the $\Delta h_{area,MCC,p}$ and $\Delta h_{comb,p}$ properties. The $\Delta h_{area,MCC,p}$ property was calculated by integrating the HRR signal over the pyrolysis temperature range and dividing it by the heating rate of the sample, as shown in Eqn.(10) and described elsewhere [157].

$$\Delta h_{area,MCC,p} = \int_{T_{in}}^{T} \left(HRR\right) d\theta / (dT / dt) \quad (10)$$

The $\Delta h_{area,MCC}$, similar to HRR, is based on the initial mass of the sample. The effective heat of combustion is calculated on the basis of volatile mass for charring materials. Thus, the Δh_{comb} property was calculated as per Eqn. (11) [155].

$$\Delta h_{comb,p} = \Delta h_{area,MCC,p}\left(\frac{1}{1-Y_c}\right) \tag{11}$$

Similarly, heat of char combustion is calculated as per Eqn. (12)

$$\Delta h_{comb,cc} = \Delta h_{area,MCC,cc}\left(\frac{1}{1-Y_{cc}}\right) \tag{12}$$

and the total heat of combustion for a fuel sample is calculated as shown in Eqn. (13)

$$\Delta h_{comb,cc} = \left(1-Y_c\right)\Delta h_{comb,p} + Y_c \Delta h_{comb,cc} \tag{13}$$

6.4 Energetic signals

This discussion is divided in two parts. Firstly, the DSC-DTG signals obtained from the STA data are presented. Next, the HRR signals from MCC are discussed.

6.4.1 STA signal analysis

Figure 35 shows the DTG and DSC signals for pyrolysis of CS-Raw and CS-Leached samples.

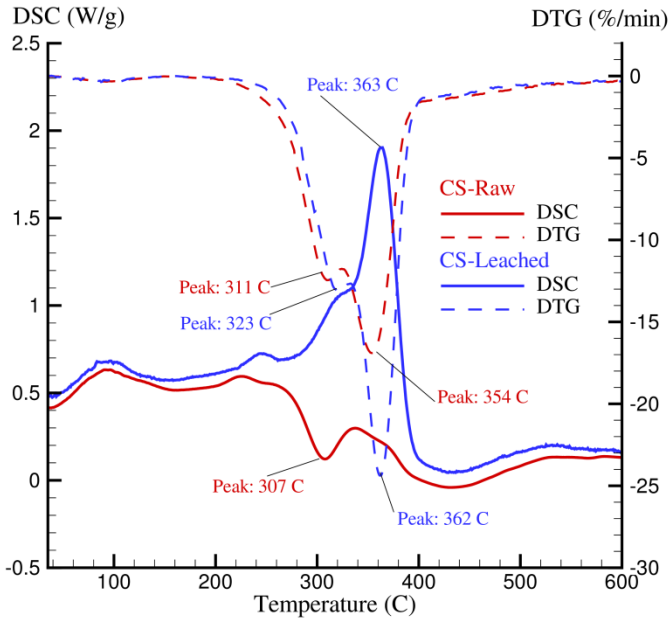

Figure 35: DSC and DTG signals for pyrolysis of CS-Raw and CS-Leached samples

The DSC signal is shown in per unit initial sample mass basis. For the CS-Leached sample, the DTG peak temperatures for hemicellulose and cellulose decomposition are noted to be accompanied with endothermic DSC peaks at the same temperature points. However, the energetics for the pyrolysis of CS-Raw sample produces different results. Although, the hemicellulose decomposition DTG peak temperature is accompanied by a DSC peak at around 308ºC, the direction of DSC peak suggests an exothermic reaction. On the other hand, the cellulose decomposition DTG peak temperature does not accompany any corresponding peak in its DSC signal for the CS-Raw sample. Similar results were observed for the leaching of SG biomass samples as well. The lack of endothermic peaks in raw biomass samples have been attributed to the occurring of secondary exothermic reactions due to the presence of alkali salts in their untreated state [26]. Overall, the decomposition reactions shifted to higher temperatures and became highly endothermic on biomass leaching.

Figure 36 shows the DTG and DSC signals for the EC and CS-Leached samples. Unlike leached biomass samples, the DTG peak temperature for EC sample at 488 ºC did not accompany any DSC peak. The devolatilization of coal is much more complex than biomass, where various stages of softening [160], physical transitions [168] and coal swelling [160] takes place apart from the primary pyrolysis reactions.

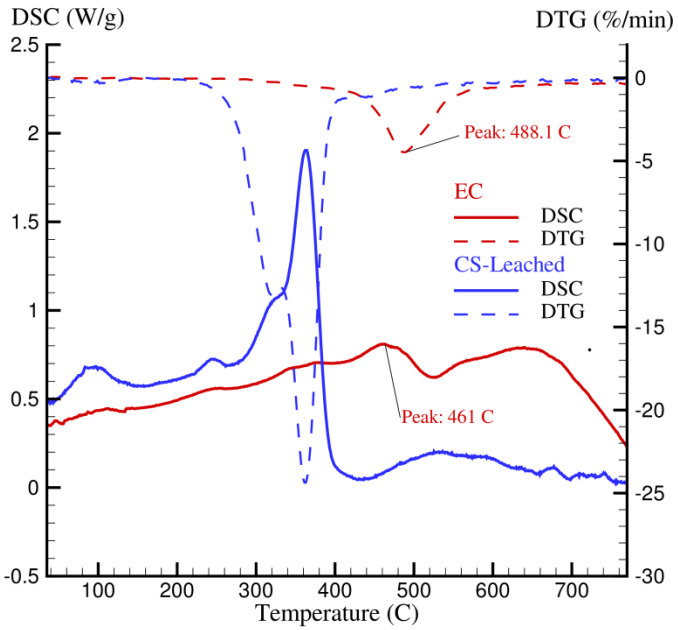

Figure 36: DSC and DTG signals for pyrolysis of EC and CS-Leached samples

As observed from **Figure 36**, EC pyrolysis resulted in a smaller endothermic peak than the CS-Leached sample. The smaller endothermic peak value of coal samples is partially due to much lower amount of volatile matter present in comparison to biomass samples. However, the DSC peak value for EC was comparable to the DSC peak value of CS-Raw sample despite the higher char yield of the coal sample.

Figure 37 shows the DSC signals obtained from the pyrolysis of 80:20 fuel mixture of EC and CS-Leached samples. The DSC profile for a simulated weighted sum of individual EC and CS-Leached sample DSC signals in 80:20 ratio was also generated. The simulated weighted sum DSC profile matched sufficiently the DSC profile of EC and CS-Leached fuel mixture, under the tested conditions. Thus, the mixture of EC and CS-Leached biomass sample delivered an additive pyrolysis energetics data. A similar conclusion was made out for EC and SG-Leached mixture STA data.

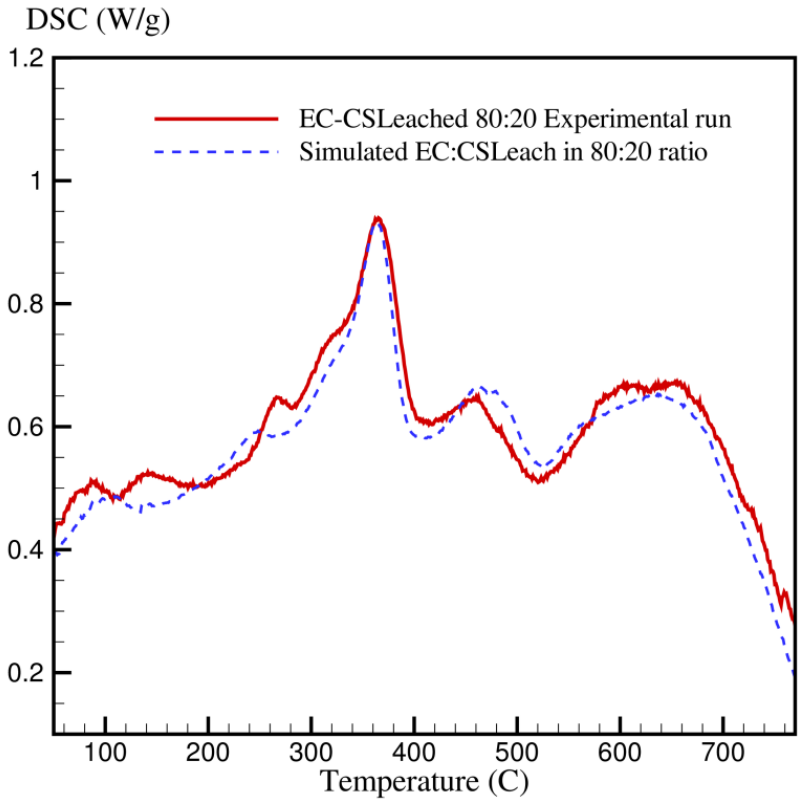

Figure 37: DSC signals for EC and CS-Leached mixture pyrolysis at 20 K/min heating rate.

6.4.2 MCC signal analysis

Pyrolysis gas combustion heat release rate signals of CS-Wash, CS-Leached and EC samples are shown in **Figure 38**. The HRR, similar to the DSC signal, is measured on the basis of per unit initial mass of the sample. As observed from **Figure 38**, the peak temperature for HRR of these fuels matches their respective peak temperature of DTG signal. As expected, this signifies that the rate of production of pyrolysis gases is proportional to the heat generated during the combustion of those gases.

Figure 38 demonstrates the effect of leaching on the pyrolysis gas combustion HRR signals of biomass samples. As observed from **Figure 38**, the peak HRR value of CS-Leached sample (58.2 W/g) is found to be much higher than that of the CS-Raw sample (37.5 W/g). This is in agreement with the DTG data shown in **Figure 30**, where it can be observed that the devolatilization rate increases on biomass leaching.

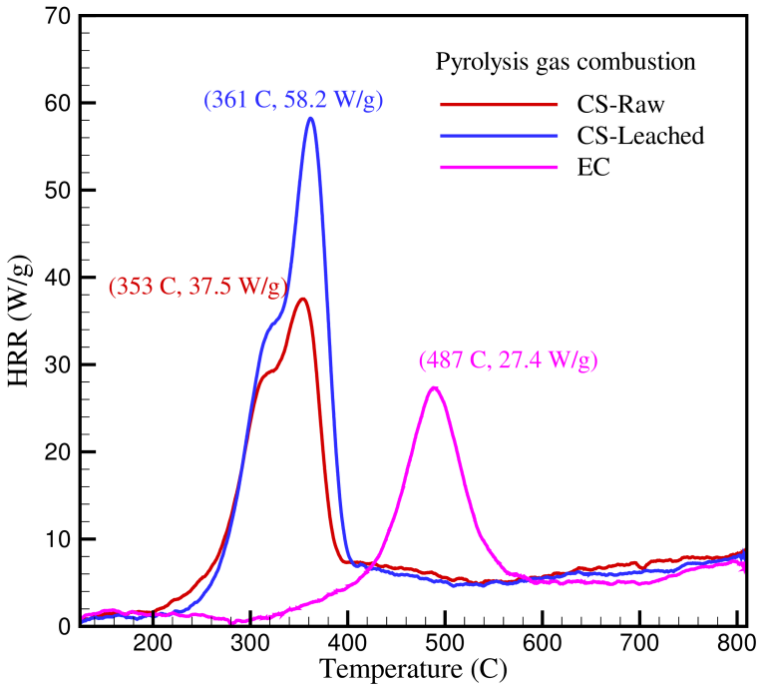

Figure 38: HRR for pyrolysis gas combustion of CS-Raw, CS-Leached and EC samples

A larger difference between the energy density of the samples is seen from comparing HRR signals of EC and biomass samples in **Figure 38**. As known from the previous discussion, the amount of volatile matter released from EC pyrolysis is substantially lower than that released

by biomass samples (~20% volatile matter for EC in compared to ~80% for biomass samples). With a relatively very low devolatilization rate for EC sample, as observed in **Figure 38**, the peak height for HRR signal of EC was comparable in comparison to biomass samples shown in **Figure 38**.

Figure 39 contains the initial mass based HRR signals obtained from the pyrolysis of 80:20 fuel mixture of EC and CS-Leached samples. The HRR profile for a simulated weighted sum of individual EC and CS-Leached sample HRR signals in 80:20 ratio was also generated. The simulated weighted sum HRR profile matched sufficiently the HRR profile of EC and CS-Leached fuel mixture. Thus, the mixture of EC and CS-Leached biomass sample delivered additive combustion energetics. A similar conclusion was determined for EC and leached SG co-pyrolysis HRR data.

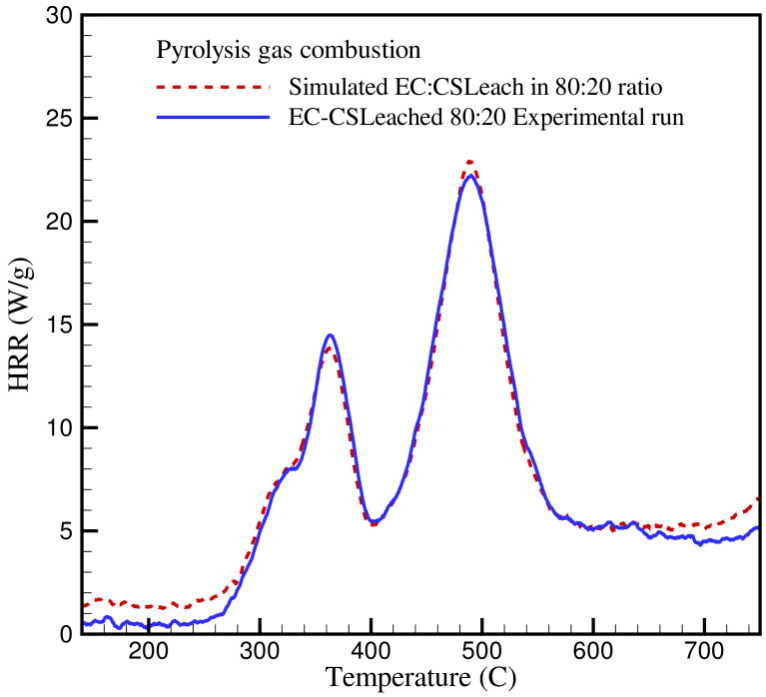

Figure 39: HRR for pyrolysis gas combustion of EC and CS-Leached mixture pyrolysis at 20 K/min heating rate.

Figure 40 includes the char combustion heat release rate signals for the CS-Raw, CS-Leached and EC samples. As observed from **Figure 40**, the peak temperature and shape profile for char combustion signals is different than those of pyrolysis signals. The char combustion experiments conducted in MCC are non-flaming in nature. Therefore, there are no sharp peaks

associated with the ignition of the samples and the oxidation is uniform over a wide temperature range. The biomass char combustion HRR peak and profile changes on water leaching, as seen from **Figure 40**. The leached biomass char oxidized at higher temperatures due to the removal of autocatalytic alkali salts. The peak HRR for leached biomass is lower than that of raw biomass, however the leached biomass sample oxidizes at over a broader temperature range than that of raw biomass.

The char combustion signal for EC is different than that of biomass samples. The EC char oxidizes at a higher temperature, with higher peak HRR and over a broader temperature range. The oxidation of EC char is not complete even at temperature as high as 750ºC (the limit of MCC).

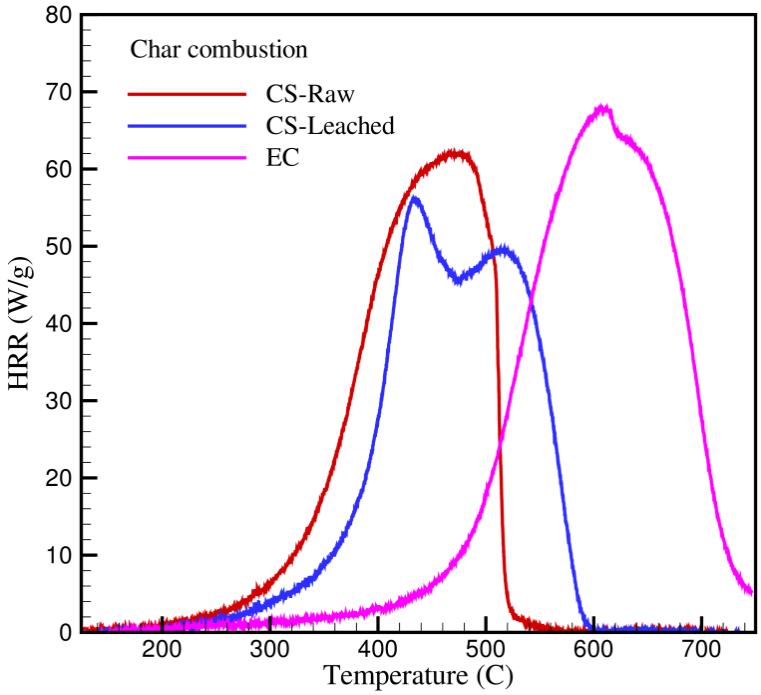

Figure 40: Char combustion heat release rate signals for CS-Raw, CS-Leached and EC samples

6.5 Energetic properties evaluation

6.5.1 Heat of pyrolysis and heat of gasification

Table 9 reports the $\Delta h_{area,DSC}$ (initial mass basis), Δh_{pyr} (volatile mass basis), Δh_{gas} (volatile mass basis) and Y_c values calculated for all samples at 20 K/min heating rate. Y_c values were calculated form ratio of final and initial mass of sample in Pt-Rh pan.

Table 9: Pyrolysis energetic properties of fuel samples pyrolysis at 20 K/min heating rate

Experimental Runs	$\Delta h_{area,DSC}$ (J/g)	Δh_{pyr} (J/g)	Δh_{gas} (J/g)	Y_c
SG-Raw	125 ± 1.2%	77 ± 1.2%	903 ± 1.2%	0.194
CS-Raw	19	13	731	0.225
SG-Leached	374	194	1235	0.146
CS-Leached	538	271	1133	0.137
EC	389	1336	5312	0.747
EC & SG-Leached in 80:20 Mixture	320	766	3894	0.658
EC & CS-Leached in 80:20 Mixture	461	900	3276	0.599

The quantities were calculated per the pyrolysis model application [155] (Eqn. (7), (8) and (9)) onto the STA data. Based on lower char yield from biomass pyrolysis (0.14-0.22 for different samples), the Δh_{pyr} values are noted to be lower than the corresponding $\Delta h_{area,DSC}$ values. Contrarily, the Δh_{pyr} value for EC sample is noted to be much higher than its $\Delta h_{area,DSC}$ value, owing to its high char yield ($Y_c = 0.75$). Thus, the Δh_{pyr} values for EC sample was found to be much higher than Δh_{pyr} values for biomass samples.

Consequently, as the Δh_{pyr} directly contributes to the heat of gasification (Eqn. (7)), the Δh_{gas} values for EC sample was found to be much higher than Δh_{gas} values for biomass samples. The high value of Δh_{gas} values for EC is also attributed to the fact that the coal pyrolysis takes place at higher temperature ranges than biomass samples, thus resulting in a higher sensible heat for EC pyrolysis. Between the two leached biomass samples, even though the Δh_{pyr} value was higher for the CS-Leached sample, the Δh_{gas} value was found to be higher for the SG-Leached sample due to its higher sensible heat.

Table 9 also contains $\Delta h_{area,DSC}$, Δh_{pyr} and Δh_{gas} values for the two fuel mixture test cases of EC and leached biomass samples. An interesting point noted from the data for the two fuel mixture samples is related to comparing their $\Delta h_{area,DSC}$ and Δh_{pyr} values. For the 80:20 initial mass mixture ratio of EC and leached biomass samples, the $\Delta h_{area,DSC}$ value was not found to be close to the two values from the individual runs of each coal and leached biomass runs. In the case of EC and SG-Leached mixture, the $\Delta h_{area,DSC}$ (320.1 J/g) was found to be lower than the $\Delta h_{area,DSC}$ values for each EC (389 J/g) and SG-Leached samples (374 J/g). However, the Δh_{pyr} and Δh_{gas} values for each of the mixtures were found to be in between energetic values for the

individual fuels. This was in part attributed to correct calculation of energetic properties on their per unit volatile mass basis using the validated pyrolysis model [155]. Thus, Δh_{pyr} and Δh_{gas} properties were able to more accurately characterize the energetic properties of fuel in comparison to the traditional approach of using $\Delta h_{area,DSC}$ values.

To further assert the above mentioned point, weight additive values of Δh_{pyr} and Δh_{gas} properties were compared for fuel mixture data. It has already been shown in previous sections that the mixture of EC and leached biomass samples deliver additive TGA and DSC curves. Thus, the energetic properties derived from the EC and leached biomass mixture runs should also deliver weight additive energetic properties of individual coal and leached biomass samples. These values were calculated for weighted additions of energetic properties of individual EC and leached biomass samples and are reported in **Table 10**. The simulated values reported in **Table 10** are compared with those present in **Table 9** for the coal and leached biomass mixtures and presented as error percentage in brackets. The weighted simulations, presented in **Table 10**, were calculated for two types of weighted additions. The first type of weight addition, for EC and leached biomass samples, was conducted per the initial weight contribution of each fuel (i.e. in 80:20 ratio). The second type of weight addition was carried out on the basis of the volatile mass contribution of the respective fuels. The volatile contribution for an initial mass mixture of EC and leached biomass in 80:20 ratio yielded volatile matter in 54:46 ratio for both test cases involving different biomass samples. The rationale behind using the second weighted addition methodology lies in the definition of Δh_{pyr} and Δh_{gas} properties, which are both calculated on the volatile mass loss basis.

Table 10: Weighted additions of Δh_{pyr} and Δh_{gas} properties for individual fuel samples to estimate the energetic properties for the two fuel mixture test cases.

Estimation Methodology	80:20 ratio property addition from individual fuel samples (J/g)		54:46 ratio property addition from individual fuel samples (J/g)	
Fuels simulated	Δh_{pyr} (Error %)	Δh_{gas} (Error %)	Δh_{pyr} (Error %)	Δh_{gas} (Error %)
EC & SG-Leached (80:20)	1107.8 (+43.7%)	4496.54 (+15.5%)	810.8 (+5.9%)	3436.4 (-11.7%)
EC & CS-Leached (80:20)	1123.1 (+24.8%)	4476.3 (+36.6%)	846.1 (-6.0%)	3389.8 (+3.5%)

Column 2 and column 3 in **Table 10** provide the energetic properties estimated by the first type of weighed addition in 80:20 ratio. These were compared with the calculated energetic properties reported for the two fuel mixture test cases reported in **Table 9**. As seen from **Table 10**, large errors were observed in the property estimation by the initial mass based weighted addition. In comparison, the properties estimated on the volatile mass contribution basis are shown in **Table 10** to be closer to those measured for the actual fuel mixture runs reported in **Table 9**. A validation for weighted energetic property addition has not been conducted in the literature for coal and biomass samples. These analyses validate that Δh_{pyr} and Δh_{gas} properties must be calculated on the volatile mass loss basis. In addition, it also asserts that the predictions for energetic properties of fuel mixtures must be made on the basis of their volatile mass contribution, instead of their initial mass proportion.

6.5.2 Heat of pyrolysis gas combustion and heat of char combustion

Table 11 reports the $\Delta h_{area,MCC,p}$ (initial mass basis), $\Delta h_{comb,p}$ (volatile mass basis), $\Delta h_{area,MCC,cc}$ (initial mass basis), $\Delta h_{comb,cc}$ (volatile mass basis), Δh_{comb} (volatile mass basis), Y_c and Y_{cc} values calculated for all samples at 20 K/min heating rate using MCC. The definition, and method of calculation of these properties has previously been described from Eqn. (10)-(13).

Table 11: Energetic combustion properties of fuel samples from MCC

Experimental Runs	$\Delta h_{area,MCC,p}$ (J/g)	$\Delta h_{comb,p}$ (J/g)	$\Delta h_{area,MCC,cc}$ (J/g)	$\Delta h_{comb,cc}$ (J/g)	Δh_{comb} (J/g)	Y_c	Y_{cc}
SG-Raw	10,542	12,570	26,659	30,206	15,416	0.161	0.118
CS-Raw	9,641	11,274	26,840	30,461	14,052	0.145	0.119
SG-Leached	10,275	12,170	27,247	30,295	14,992	0.156	0.101
CS-Leached	9,641	12,501	26,840	30,324	15055	0.143	0.086
EC	9,185	36,038	35,424	40,307	39,219	0.745	0.121
EC & SG-Leached in 80:20 Mixture	9,277	24,045	29,067	33,531	29,871	0.614	0.133
EC & CS-Leached in 80:20 Mixture	9,545	26,129	29,892	34,641	31,532	0.635	0.137

*Uncertainty in heat of combustion = ±3%; Uncertainty in area values = ±2%;

For biomass samples, the $\Delta h_{area,MCC,p}$ values were found to be slightly lower than their corresponding $\Delta h_{comb,p}$ values, owing to their lower char yield as per Eqn. (11). Contrarily for EC sample, the $\Delta h_{area,MCC,p}$ value are much higher than its $\Delta h_{comb,p}$ value, owing to its high char yield. Thus the heat of pyrolysis gas combustion, $\Delta h_{comb,p}$, for EC sample is measured to be much higher than that of biomass samples, when calculated on the basis of volatile mass. This is in agreement with the similar observation made in the previous section regarding the Δh_{pyr} values of fuel samples. Also, the heat of char combustion, $\Delta h_{comb,cc}$, for EC is higher than that of biomass counterparts. Consequently as per Eqn. (13), the total heat of combustion, Δh_{comb}, for EC was found to be much higher than biomass samples.

As observed from **Table 11**, the $\Delta h_{comb,p}$ values for leached biomass sample are not significantly different than the corresponding values of their untreated counterparts. This is in clear contrast to the observations in the previous section, where a substantial increase in the Δh_{pyr} values was observed on biomass leaching, primarily due to the absence of secondary exothermic reactions (**Table 9**). Thus, leaching of biomass samples does not necessarily increase the pyrolysis gas energy density of the biomass fuel. However, the $\Delta h_{area,MCC,p}$ values for biomass samples show a clear increase due to water leaching. This happens due to $\Delta h_{area,MCC,p}$ values been calculated on the initial sample mass basis, where as $\Delta h_{comb,p}$ is calculated on the volatile mass basis of the pyrolyzing fuel. Similarly, the $\Delta h_{comb,cc}$ values do not change on biomass water leaching. This observation signifies that the absence of salts does not significantly affect the quality of the biomass char. Consistent with the two observations, the Δh_{comb} values were not significantly affected on biomass water leaching.

The difference between the measurement of $\Delta h_{area,MCC,p}$ and $\Delta h_{comb,p}$ values is also evident from the property values reported for coal and leached biomass mixture runs in **Table 11**. Here, $\Delta h_{comb,p}$ values for mixture samples show a better representation of weighted sum of $\Delta h_{comb,p}$ values of individual fuels, in contrast to the $\Delta h_{area,MCC,p}$ properties.

To further assert the above mentioned point, weight additive $\Delta h_{comb,p}$ values of individual fuels were compared to those of fuel mixture runs. It has already been shown through **Figure 39** that the mixture of EC and leached biomass samples deliver additive HRR curves. Thus, the $\Delta h_{comb,p}$ values derived from the EC and leached biomass mixture runs must also deliver weight additive $\Delta h_{comb,p}$ values of individual coal and leached biomass samples. Thus, the simulated weighted sum values of the fuel mixtures were calculated and are reported in **Table 12**. The

simulated values reported in **Table 12** are compared with those present in **Table 11** for the coal and leached biomass mixture runs (last two rows in **Table 11**) and presented as error percentage in brackets. The weighted simulations, presented in **Table 12**, were calculated for two types of weighted additions. Similar to the previous section, these additions were based on the initial weight contribution of the individual coal and biomass fuels, and volatile mass contributions for coal and biomass samples. A similar exercise was run for $\Delta h_{comb,cc}$ values for coal and leached biomass mixtures, and the results are shown in **Table 12**.

Table 12: Weighted additions of $\Delta h_{comb,p}$ and $\Delta h_{comb,cc}$ properties for individual fuel samples to estimate the energetic properties for the two fuel mixture test cases. Additions in initial mass ratio (80:20) and volatile mass ratio (54:46) basis.

Estimation Methodology	80:20 ratio property addition from individual fuel samples (J/g)		Volatile ratio property addition from individual fuel samples (J/g)	
Fuels simulated	$\Delta h_{comb,p}$ (Error %)	$\Delta h_{comb,cc}$ (Error %)	$\Delta h_{comb,p}$ (Error %)	$\Delta h_{comb,cc}$ (Error %)
EC & SG-Leached (80:20)	31264 (+30.0%)	38305 (+14.2%)	25059 (+4.2%)	35701 (+6.5%)
EC & CS-Leached (80:20)	31331 (+19.9%)	38310 (+10.6%)	25211 (-3.5%)	35715 (+3.1%)

Table 12 provides the energetic properties estimated by the first type of weighed addition in 80:20 ratio. Large errors were observed in the property estimation by the initial mass based weighted addition. In comparison, the properties estimated based on the volatile mass contribution basis, shown in **Table 12**, were closer to those calculated for the actual fuel mixture runs reported in **Table 11**. This is in agreement with the conclusions from the previous section where the Δh_{pyr} property addition on the basis of volatile mass contributions of individual fuel samples, accurately predicted the Δh_{pyr} properties of the fuel mixture. This is due to both Δh_{pyr} and Δh_{comb} properties being calculated on the fuel volatile mass basis. These analyses firstly validate that the Δh_{comb} property must be calculated on the volatile mass loss basis. Secondly, it asserts that the predictions for combustion energetic properties of fuel mixtures must be made on the basis of their volatile mass contribution, instead of their initial mass proportion.

6.6 Conclusions

The focus of this chapter was to accurately characterize the pyrolysis and combustion energetics of decomposing solid fuel samples. The energetic properties of coal, biomass and coal-biomass mixture samples were investigated using a STA and a MCC. The effects of biomass water leaching on the energetics of biomass fuels and coal-biomass fuel mixtures were also studied.

The water leaching of biomass samples mitigates the secondary reactions during pyrolysis, shifted the primary decomposition reactions to higher temperatures, and reduced the char yield of biomass fuel samples. An increase in the heat of pyrolysis was noticed on biomass water leaching due to removal of secondary exothermic reactions. However, the heat of combustion of leached biomass was not measured to be significantly higher than that of untreated biomass samples. Thus, leaching of biomass samples does not necessary increase the energy density of biomass fuels.

It was found that the co-pyrolysis of coal and leached biomass fuel mixtures exhibited a weight additive energetic behavior, when pyrolyzed on an 80:20 initial mass proportion. It was further validated and concluded that the weighted sum prediction for the heat of pyrolysis and the heat of combustion for coal-biomass fuel mixtures must be conducted on the basis of their individual volatile mass contributions and not on the basis of initial fuel mixture proportion.

6.7 Nomenclature

c	Specific heat capacity (J/g-K)
dT/dt	Heating rate of the sample (K/s)
DSC	Heat given to the sample using DSC (W/g)
DTG	Derivative of TG (%/min)
Δh	Specific heat associated with process (J/g)
HRR	Heat release rate using MCC (W/g)
T	Temperature (K)
TG	Thermogravimetric response (initial weight %)
Y	Yield

Subscripts

app	Apparent
area	Area difference between apparent and sensible
c	Char
cc	Char combustion
comb	Combustion
DSC	Measured by the DSC apparatus
gas	Gasification
in	Initial
MCC	Measured by the MCC apparatus
p	Pyrolysis
pyr	Pyrolysis
sen	Sensible

7. FUEL PERFORMANCE

7.1 Introduction

Questions about the long-term availability of traditional fossil fuels, their geopolitical availability, and the tightening environmental restrictions have resuscitated the need to explore renewable and clean sources of energy to alleviate the concerns of ever increasing energy demand. Addition of renewable fuels such as biomass [13, 42, 51-55, 59], industrial wastes from biodiesel production such as glycerol [169], and municipal solid waste (MSW) [38-40, 170, 171] including wide range of plastics [172], waste wood [51, 52, 54], cardboard [173], paper [43] etc. have been recently investigated for co-combustion usage with coal. The pyrolysis of blends of alternate sources of fuels with traditional fossil fuels, such as coals, leads to improved energy and chemical recovery from the lifecycle of these products [38]. Additionally, it also provides an alternative to the current disposal techniques of wastes such as land filling and incineration, which has raised issues related to soil fertility, land price depreciation and environmental pollution [39].

Predicting the thermal response of solid fuels and blends undergoing pyrolysis and combustion has historically been of primary interest in the areas of fire flammability and gasification applications. Proper characterization of such fuels is needed in order rank the fuel performance and customize the fuel blends in for efficient usage. However, the literature studies have been limited to the characterization of blends and identification of interactions between different fuel samples during co-pyrolysis [14, 41-44, 46]. There is a lack of approach in the literature to design and customize fuel bends for efficient combustion along the pyrolysis temperature range and predict its performance using simple experiments and mathematical models.

As a first step to the customization of fuel blends, a system to indicate the rank based performance of an individual fuel needs to be developed. In the literature, the fuels have primarily been distinguished on the basis of their char yields [26, 159], pyrolysis temperature range [29, 40, 146], Arrhenius kinetic parameters [32, 34, 38, 45, 47, 137, 138, 147, 148, 154], HHV (from bomb calorimeter data) [174-178] and evolved gas analysis [14, 39, 40, 44, 179]. However, the energetic characterization (in terms of heat of pyrolysis and heat of combustion) of fuel and blends is not as well understood as the other aspects of their pyrolysis process. Proper characterization of fuels, both from pyrolysis and combustion perspectives, is necessary to

develop such fuel performance model. Hence, a methodology needs to be developed for complete characterization of fuels, including proper energetic characterization, and integrate it with a validated process that determines the ranking of fuels.

The reactivity of a fuel requires a total energy balance on the fuel, which includes the energy required for pyrolysis of the material as well as the heat released from combustion of the evolved gases and char. These quantities are required as a function of temperature in order to estimate the performance of fuel and blends, which decompose at different temperature ranges. The methodology of calculating accurate heat of pyrolysis and heat of combustion has been discussed in Chapter 6 using simultaneous thermogravimetric analyzer (STA) and micro-scale combustion calorimeter (MCC) instruments, respectively. These two instruments also combines the fuel properties based on their temperature dependent char yields (using TGA data), pyrolysis temperature (using STA data), Arrhenius kinetic parameters (using TGA data), evolved gas analysis (estimating gas quality from MCC data), pyrolysis energetics (using DSC data) and combustion energetics (using MCC data) simultaneously. Integrating the fuel characterization with a fuel decomposition and combustion model will provide the tools necessary to estimate the performance of fuels and blends.

Therefore, with the help of these instruments both temperature based, as well as integrated energetic properties of the fuels can be determined for fuel ranking. The data acquired from these techniques can be applied onto an energy balance model for a single fuel particle to determine the fuel performance, and hence its ranking, along the decomposition temperature range of the fuel.

7.2 Experimental procedure

The coal-biomass materials and their preparation method is discussed in Section 4.2.1. The instrumentation and analysis procedure for STA and MCC is discussed in Section 6.2. In addition to coal- biomass fuels, glycerol (99% purity CAS# 56-81-5) and Polystyrene (PS; MW = 250,000) were used in this study. Both samples were obtained from Sigma Aldrich. PS granules were of irregular form and crushed to < 1 mm diameter range using liquid nitrogen cooled mortar. The powdered PS was tested in the mass range of 4-6 mg in STA and MCC. Glycerol was used in its viscous liquid form and its sample mass was on the order of 10-15 mg.

7.3 Fuel performance model

Solid fuels when sufficiently heated will produce gas volatiles through pyrolysis. This includes non-charring materials such as many plastics as well as charring materials.

$$Fuel \xrightarrow{N_2,\Delta} char + gas$$

Based on the energy balance of a single fuel particle undergoing pyrolysis, a model for the transient temperature rise of a fuel with lumped model analysis is [155, 180].

$$\dot{Q}_{net} = \left[mc\frac{dT}{dt} + \dot{m}_{pyr}\left(-\Delta h_{pyr}\right) \right] \tag{14}$$

Here $\dot{Q}_{net}$ is the net heat transfer rate to the fuel (W), m is the instantaneous fuel mass (g), c is the specific heat of the fuel (J/g-K), T is the fuel temperature (K), t is time (s), $\dot{m}_{pyr}$ is the fuel mass loss rate due to pyrolysis (g/s), and Δh_{pyr} is the heat of pyrolysis (J/g). The first term on the right hand side of the Eqn. (14) represents the sensible energy to heat up the fuel while the second term is the latent heat to generate volatiles. An endothermic reaction is defined here to be a positive value. For certain plastics, an additional term for the heat of melting can also be added to Eq. (14) [155].

The heat of combustion of volatiles generated during pyrolysis of fuels is calculated by

$$\dot{Q}_{c,p} = \dot{m}_{pyr}\Delta h_{comb,p} \tag{15}$$

Here $\dot{Q}_{c,p}$ is the heat release rate of the volatiles due to combustion (W) and $\Delta h_{com,pb}$ is the effective heat of combustion of the volatiles generated from fuel pyrolysis (J/g) [157, 167]. Since the combustion process is exothermic, $\Delta h_{comb,p}$ is a negative value.

The fuel pyrolysis performance parameter represents the rate of energy released from the combustion of pyrolysis gases, to the rate of energy required to generate pyrolysis gases. An expression for fuel pyrolysis performance was derived by solving the Eqn. (14) and Eqn. (15) for $\dot{m}_{pyr}$ and rearranging to obtain

$$\eta_p = \frac{\dot{Q}_{c,p}}{\dot{Q}_{net}} = \left(1 - \frac{mc\dfrac{dT}{dt}}{\dot{Q}_{net}}\right)\left(\frac{-\Delta h_{comb,p}}{\Delta h_{pyr}}\right) \tag{16}$$

Note that the pyrolysis performance parameter in Eqn. (16) is temperature dependent. From Eqn. (16), the fuel pyrolysis performance parameter is dependent on the fuel temperature during pyrolysis, the heat transfer rate for sensible heating of the fuel, and the ratio of the heat of combustion to heat of decomposition.

An integrated form of Eqn. (16) provides a single value that represents the total pyrolysis performance of the fuel.

$$\eta_{p,tot} = \frac{Q_{c,p}}{Q_{net}} = \left(1 - \frac{\int mc\dfrac{dT}{dt}\,dt}{Q_{net}}\right)\left(\frac{-\Delta h_{comb,p}}{\Delta h_{pyr}}\right) \tag{17}$$

For current experiments, the heating rate (*dT/dt*) has been kept constant at 20 K/min. The instantaneous mass (*m*) and specific heat (*c*), along with the $\dot{Q}_{net}$ given to the fuel sample for complete pyrolysis was obtained using the STA data [155, 180]. The measurement procedure for heat of pyrolysis and heat of combustion was described in Section 6.3.

The fuel pyrolysis performance expressions listed in Eqn. (16) and Eqn. (17) assimilates the contribution of char yield, pyrolysis temperature, mass loss kinetics, evolved gas quality, pyrolysis energetics and combustion energetic, apart from other temperature dependent properties. This is in contrast with many literature studies where some of these individual properties have been evaluated to compare and characterize the performance of fuels.

The char combustion performance parameter can similarly be calculated for the following reaction.

$$Char \xrightarrow{O_2,\Delta 20K/\min} ash + gas$$

The temperature dependent char combustion performance parameter is defined as ratio of heat released during char oxidation to the sensible heat required to heat the char sample up to its

gasification temperature. Assuming the latent heat of pyrolysis of a char sample to be negligible, the expression for char combustion performance is defined as follows:

$$\eta_{cc} = \frac{\left(-\Delta h_{comb,cc}\right)\frac{dm}{dt}}{\left(m_c c_c + m_{ash} c_{ash}\right)\frac{dT}{dt}} \tag{18}$$

The total char performance parameter can then be calculated as:

$$\eta_{cc,tot} = \frac{\left(-\Delta h_{comb,cc}\right)\left(M_{in,cc} - M_{fin,cc}\right)}{\int\left(m_c c_c + m_{ash} c_{ash}\right)dT} \tag{19}$$

The cumulative fuel performance as a sum of pyrolysis performance and char performance can be calculated as Eqn. (20) on temperature basis and Eqn. (21) on total basis.

$$\eta_{cum} = \left(1 - Y_c\right)\eta_p + Y_c \eta_{cc} \tag{20}$$

$$\eta_{cum,tot} = \left(1 - Y_c\right)\eta_{p,tot} + Y_c \eta_{cc,tot} \tag{21}$$

7.4 Results and discussion

7.4.1 Fuel pyrolysis performance

Figure 41(a) contains the ratio of the pyrolysis gas combustion heat release rate and heat transfer rate to heat the fuel (i.e., fuel pyrolysis performance parameter, η_p). In general, a higher fuel pyrolysis performance indicates a better fuel for pyrolysis application. As seen in **Figure 41(a)**, these different types of fuels undergo pyrolysis over a wide range of temperature. The glycerol evaporates between 150-300ºC while the SG-Raw undergoes the majority of pyrolysis at temperatures of 220-500ºC. The pyrolysis of PS occurs over a narrow temperature of 350-450ºC while EC undergoes pyrolysis over a broader temperature range (300-600ºC) with the primary degradation between 400ºC and 550ºC. The advantage of fuels pyrolyzing over such a wide temperature range is that it could assist in designing customized fuel blends for consistent performance over a wide temperature range, e.g. the coal-biomass blend as shown in **Figure 41(b)**.

The complexities of defining the fuel performance parameter based on its Δh_{pyr} and $\Delta h_{comb,p}$ values have been discussed in the Section 6.5, where there were increases in Δh_{pyr} property values on biomass water leaching, and decrease in Δh_{pyr} and $\Delta h_{comb,p}$ property values due to biomass mixing in coal. In such definitions of performance, the fuel ranking becomes uncertain.

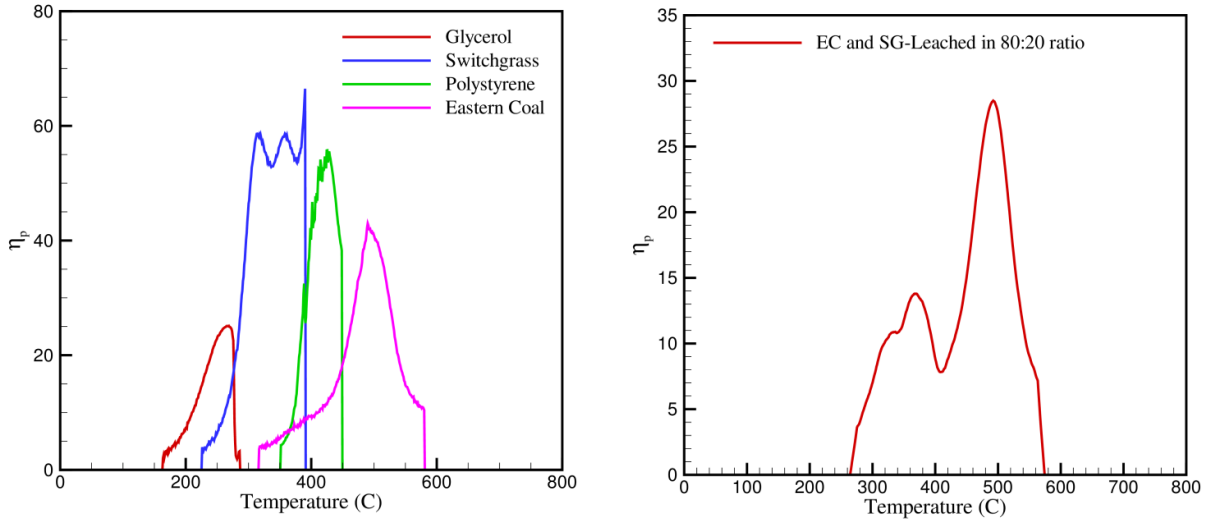

Figure 41: Temperature dependent fuel pyrolysis performance parameter η_p (a) Glycerol, PS, SG-Raw and EC samples (b) EC & SG-Leached mixture in 80:20 ratio

Table 13 reports the peak heat release rate (HRR_{peak}), $\Delta h_{comb,p}/\Delta h_{pyr}$ and $\eta_{p,tot}$ pyrolysis properties of glycerol. PS, SG-Raw, and EC fuel samples. Many studies in the literature have used the peak heat release rate, heat of pyrolysis, heat of combustion or $\Delta h_{com,p}/\Delta h_{pyr}$ as an indicator of fuel performance. However, as indicated in the **Table 14**, all these criteria reveal a different fuel performance order with no two criteria providing the same answer. However, as discussed in the previous sections, all these properties, including the temperature dependent fuel properties (such as *m*, *c* etc.) play an important role in defining the total performance of the fuel in terms of Eqn. (16) and Eqn. (17) as η_p and $\eta_{p,tot}$. As per the total fuel pyrolysis efficiency, the pyrolysis performance order for the fuels become PS > SG-Raw > Glycerol > EC.

The model also clarifies the effect of leaching on biomass in terms of pyrolysis performance change. From the previous analysis, it was shown that Δh_{pyr} values increase due to biomass leaching and $\Delta h_{com,p}$ values remained relatively constant upon biomass water leaching. Also, as per

Table 13, the HRR_{peak} increased for both biomass samples due to water leaching; whereas, the $\Delta h_{com,p}/\Delta h_{pyr}$ values showed decline on water leaching. The $\eta_{p,tot}$ property evaluation for biomass samples reveal a net decline of 31-46% in total pyrolysis performance due to water leaching. This indicates that the water leaching of biomass feedstocks is not advantageous in terms of fuel pyrolysis performance.

Table 13: Pyrolysis performance indicating energetic properties of fuel samples

Fuel	HRR_{peak} (W/g)	$\Delta h_{comb,p} / \Delta h_{pyr}$	$\eta_{p,tot}$
Glycerol	169.4	25.1	12.7±5.2%
PS	389.8	62.1	29.3
SG-Raw	42.7	164.3	18.7
CS-Raw	37.3	895.0	19.1
SG-Leached	50.3	62.7	10.1
CS-Leached	58.2	46.2	13.2
EC	26.7	27.0	7.0

Table 14: Fuel pyrolysis performance ranking order as per different criteria

Property basis	Ranking Order based on property
Δh_{pyr}	SG-Raw > Glycerol > PS > EC
$\Delta h_{com,p}$	PS > EC > Glycerol > SG-Raw
$\Delta h_{com,p}/\Delta h_{pyr}$	SG-Raw > PS > Glycerol > EC
HRR_{peak}	PS > Glycerol > SG-Raw > EC
$\eta_{p,tot}$	PS > SG-Raw > Glycerol > EC

The pyrolysis performance model also defines the difference between the performance of CS and SG biomass samples. Consistent with the MAF BTU values for the biomass samples listed in **Table 1**, the **Table 13** data shows that the CS-Raw performance is slightly higher, if not equal, to the SG-Raw performance. After water leaching, however, the performance of CS-Leached is higher than the SG-Leached sample by a factor of 1.3.

Another point of discussion in this analysis is regarding the impact of addition of biomass with coal samples onto the pyrolysis performance of blended fuel. This matter is of high importance for currently operating industrial coal based gasification plants, where the economics of biomass addition in small quantities is needed to be understood more closely. Similar to previous analysis, the evaluation of performance based on traditional criteria such as peak heat release rate, heat of pyrolysis, heat of pyrolysis gas combustion or $\Delta h_{comb,p}/\Delta h_{pyr}$ revealed conflicting results, as shown in **Table 15**. However, the application of fuel pyrolysis performance model provides a more definitive answer to the question, as the model is based on the actual physics of the fuel pyrolysis.

Table 15: Pyrolysis performance evaluation of fuel blends

Fuel	HRR_{peak} (W/g)	Δh_{pyr} (J/g)	$\Delta h_{com,p}$ (J/g)	$\frac{\Delta h_{comb,p}}{\Delta h_{pyr}}$	$\eta_{p,tot}$
EC	26.7	1336.2	36038	27.0	7.0±5.2%
EC & SG-Leached in 80:20 Mixture	20.4	765.8	24045	31.4	8.5
EC & CS-Leached in 80:20 Mixture	21.1	900.1	26129	29.0	9.3

Table 15 presents the pyrolysis performance based energetic properties of EC and blends of EC with leached biomass samples in 80:20 ratio. As observed from **Table 15**, the addition of 20% biomass to EC samples decreased the peak HRR and $\Delta h_{comb,p}$ values, while simultaneously increasing the $\Delta h_{comb,p}/\Delta h_{pyr}$ values for the mixtures. However, the fuel pyrolysis performance model reveals that the performance ranking of the fuel blend increased on biomass addition. For an addition of 20% biomass to the EC sample, the total fuel blend pyrolysis performance increased by 21% for SG-Leached addition and by 33% for CS-Leached addition. This increase in the fuel pyrolysis performance is somewhat expected based on the relatively high pyrolysis performance of the biomass, but it would not be anticipated based on the evaluating the fuel on parameters such as heat of combustion or peak heat release rate. This increase in pyrolysis performance of the fuel blend is a significant number while considering the economics of transforming a coal based reactor to coal-biomass based reactor.

7.4.2 Char combustion and cumulative performance

For many co-firing plants, where instead of fuel gasification the fuel is completely combusted in air, the performance of the fuel must also be understood in terms of char combustion performance and cumulative performance.

Figure 42(a) shows the temperature dependent char combustion performance for SG-Raw and SG-Leached samples calculated using Eqn. (18). As observed from the **Figure 42(a)**, the leaching affects the char combustion performance of fuel char at the peak temperatures of hemicellulose and cellulose decomposition. **Figure 42(a)** also shows the char combustion performance of EC char and EC-SG Leached mixture char samples. The peak values for char performance for both EC and coal-biomass mixture samples are lower than those of biomass only char samples. However, **Figure 42(a)** does not consider the effect of amount of char produced by a unit amount of fuel at the start of pyrolysis. To equate the starting amount of fuel used for a fair comparison of combustion performance, the η_{cc} factor should be multiplied by the char yield of the fuel, Y_c, as shown in **Figure 42(b)**. From **Figure 42(b)**, it can be observed that the EC char sample combustion performance is higher than those of biomass samples. Also, the EC-SG Leached mixture char sample produces its highest combustion performance at a higher temperature than that of EC char. However, the peak value of the char combustion performance of the coal-biomass mixture char is lower than that of EC.

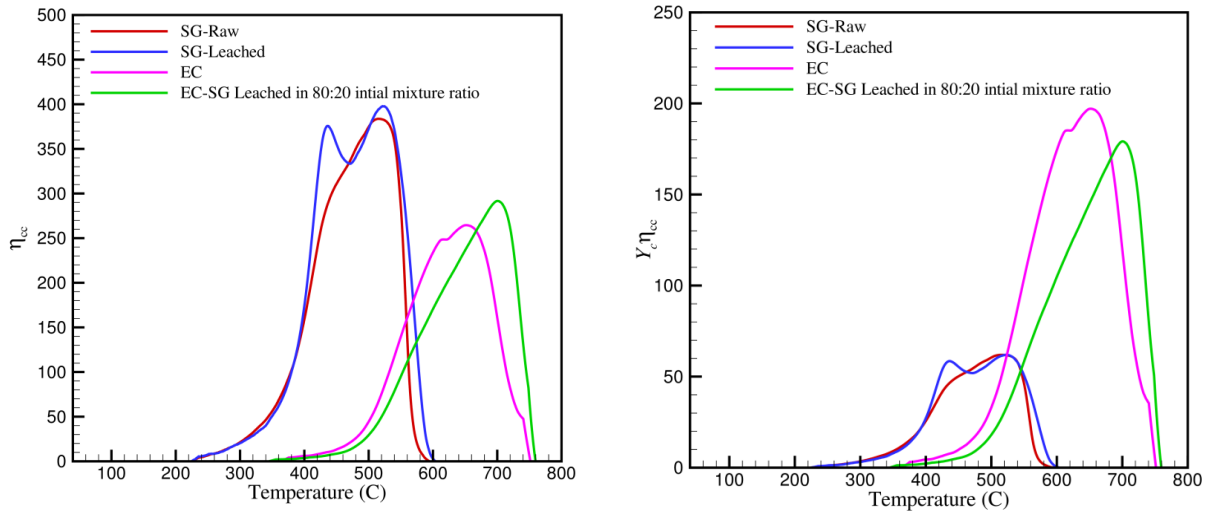

Figure 42: Temperature dependent char performance of fuel chars (a) η_c (b) $Y_c\eta_c$

To compare the combustion performance of fuel resulting from both pyrolysis and char combustion, the cumulative fuel performance can be used, as shown in **Figure 43**. The cumulative fuel performance, η_{cum}, is calculated using Eqn. (20) and considers the factor of char yield of a fuel while calculating its cumulative combustion performance. It can be observed from **Figure 43** that for lignocellulosic fuels such as biomass, where a substantial amount of pyrolysis gases are produced, the cumulative performance is significantly directed by both combustion of pyrolysis gases and char combustion. However, for fuels such as EC and their 80:20 mixtures with biomass, where char yields are much higher, the total fuel performance is primarily governed by the char combustion performance. Hence, considering the total combustion of fuel (pyrolysis + char combustion), the combustion performance of EC samples is found to be much higher than that of biomass samples and slightly higher than that of EC and biomass mixtures in 80:20 ratio.

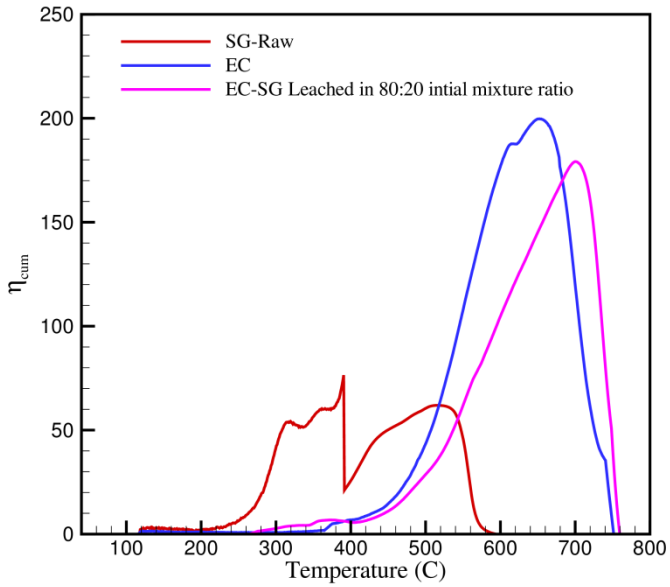

Figure 43: Temperature dependent cumulative fuel performance η_{cum}

Table 16 contains the comparison of all performance parameters of tested coal, biomass and mixture fuels. Looking at the $Y_c.\eta_{cc,tot}$ parameter to compare the char combustion performance of fuel char formed from same amount of initial fuel, it can be observed that the biomass water leaching decreases the char combustion performance by 23-26%. The char combustion performance for CS samples, both in raw and water leached states, were found to be

slightly higher than SG samples. The char combustion performance of EC char samples was found to be three times higher than that of biomass samples in raw form, as consistent with **Figure 42(b)**. Thus, the addition of leached biomass onto EC samples produced ~ 28% lower char combustion performance.

Table 16: Fuel combustion performance parameters for coal and biomass fuels

Fuel	$\eta_{p,tot}$	$\eta_{cc,tot}$	$(1-Y_c)\eta_{p,tot}$	$Y_c.\eta_{cc,tot}$	$\eta_{cum,tot}$
SG-Raw	18.7	63.1	15.7	10.2	25.9
CS-Raw	19.1	51.9	16.4	7.5	23.9
SG-Leached	10.1	67.9	8.6	10.6	19.1
CS-Leached	13.2	57.1	11.3	8.2	19.5
EC	7.0	43.8	1.8	32.6	34.4
EC & SG-Leached in 80:20 Mixture	8.5	36.9	3.3	22.7	26.0
EC & CS-Leached in 80:20 Mixture	9.3	37.6	3.4	23.9	27.3

The last column in **Table 16** compares the cumulative total combustion performance, $\eta_{cum,tot}$, of different fuels, as calculated by Eqn. (21). As per the $\eta_{cum,tot}$ performance factor, the water leaching process decreases the cumulative fuel performance of biomass fuels by 18-26%. The difference between the cumulative combustion performance of SG and CS samples were found to be statistically negligible. The cumulative combustion performance of EC sample was found to be ~28% higher than raw biomass samples and ~44% higher than the water leached biomass samples. Upon mixing biomass in coal samples in 80:20 ratio, the cumulative combustion performance of the mixture decreased by ~22% of the EC only value. This number signifies the amount of extra mass of mixture fuel that would needed to be fed into a co-firing plant in order to obtain the same performance as coal-alone combustion plant.

7.5 Conclusions

The focus of this section was to quantify the combustion performance index of fuel and blends by developing a model based on its gravimetric, pyrolysis and combustion energetics data. The models were developed for fuel pyrolysis performance, char combustion performance and cumulative fuel combustion performance. The models were developed to calculate both temperature based performance and total integrated performance of fuels and blends. The experimental data was generated using a simultaneous thermogravimetric analyzer and a micro-scale combustion calorimeter. The fuels tested in this study included coal, biomass, polystyrene and glycerol. The effects of biomass water leaching, as well as, coal-biomass blending, was also investigated in terms of fuel performance.

Using temperature dependent performance parameters, it was shown that different fuels produce peak performance at different temperatures. Thus, the mixing of various fuels will help blended fuels in generating consistent performance over a wider temperature range, which in turn can be advantageous for power plant operation.

It was found that the pyrolysis performance of a biomass fuel decreased 31-46 % on water leaching. The char combustion performance of biomass decreases 23-26 % on water leaching. Thus, the cumulative combustion performance of biomass samples decreased 18-26 % on water leaching. Hence, it was found that the water leaching may not be advantageous in terms of fuel pyrolysis or combustion performance.

The blending of coal and leached biomass fuels in 80:20 ratio was also evaluated in terms of total integrated performance parameters. It was found that the blending of biomass increases the pyrolysis performance of coal by 21-33%. However, the blending of biomass decreased the char combustion performance of coal samples by 28%. Thus, blending of biomass decreased the cumulative fuel combustion performance of coal by 22%. This performance drop due to blending signifies the amount of extra mass of mixture fuel that would needed to be fed into a co-firing plant in order to obtain the same performance as coal-alone combustion plant.

7.6 Nomenclature

c	Specific heat capacity (J/g-K)
dT/dt	Heating rate of the sample (K/s)
DSC	Heat given to the sample using DSC (W/g)

DTG	Derivative of TG (%/min)
Δh	Specific heat associated with process (J/g)
HRR	Heat release rate signal using MCC (W/g)
m	Instantaneous mass of fuel (g)
$\dot{m}$	Mass loss rate (g/s)
η	Performance
$Q_{c,p}$	Integrated heat release due to combustion (J)
$\dot{Q}_{c,p}$	Heat release rate (W)
Q_{net}	Integrated net heat required for fuel pyrolysis
$\dot{Q}_{net}$	Net heat transfer rate to the fuel
T	Temperature (K)
TG	Thermo-gravimetric response (initial weight %)
Y	Yield

Subscripts

app	Apparent
area	Area difference between apparent and sensible
c	Char
cc	Char combustion
cum	Cumulative
comb	Combustion
DSC	Measured by the DSC apparatus
in	Initial
MCC	Measured by the MCC apparatus
peak	Peak value
P	Pyrolysis
pyr	Pyrolysis
sen	Sensible
tot	Total

8. FUEL BLEND BRIQUETTING

8.1 Introduction

Alternative fuels to coal are being explored for use in existing power plants as well as more advanced systems such as gasifiers [181]. In this respect, co-firing of coal and biomass fuels into existing coal based reactors has generated substantial interest [53, 182-186]. However, there are many challenges related to the co-firing of two very different types of fuels, both in terms of reactor operations and fuel handling. One option being explored is the manufacturing of briquettes or pellets that contain one or more types of fuels [187-189]. Briquettes containing biomass are attractive because they not only increase the density of the fuel allowing for a higher energy content fuel to be delivered to the facility, but also improve the fuel handling, storage, fuel injection and issues related to biomass degradation over time [190, 191]. In addition, briquettes containing mixtures of coal and biomass have been developed for use in existing power plants to reduce the carbon footprint and decrease emissions [182, 192]. Some gasifiers have also been powered by pellets of municipal waste containing plastics, paper, and cardboard products [14, 181].

The understanding of briquette combustion behavior to date has been largely based on details of the solid combustion for individual materials without much consideration of the briquette properties. It is thus often assumed that the combustion behavior of individual fuels will dictate the combustion behavior of blended pellets [42, 182]. Most of the literature studies focus on thermogravimetric (TGA) analysis of pellet combustion behavior [37, 42, 182, 193, 194]. The usage of TGA requires the tested sample to be of milligram size, thus requiring the tested briquette to be crushed. This procedure will not accurately reflect the properties of an uncrushed briquette subjecting to its mechanical durability and non-thermally thin behavior during combustion process. The usage of TGA primarily provides the decomposition data of fuels when subjected to low heating rates (5-50 K/min) in a controlled environment. This analysis is also different to the real-time conditions that briquettes encounter while entering a furnace/reactor. In a reactor, the briquettes are instantaneously subjected to a very high heat flux and the briquette temperature rise rate is substantially higher. The fuel briquette reacts to its high temperature flames and is also affected by flames and radiation from other adjacent burning briquettes. Thus, the popular assertions that the combustion properties behavior can be simulated from the sum of its contributing constituent [182], may not turn out to be true in reactor

operations involving briquettes. The same questions also arise over the applicability of emission gas data (such as NOx, CO and CO_2) from the TGA-MS studies [182].

One of the primary motivation to study the briquette combustion behavior was the interest in co-firing biomass with coal in the Virginia Tech (VT) power plant. The VT power plant is a coal based CHP cycle plant that has been recently authorized to co-fire coal and biomass fuels (up to 15%). In a recent trial, the boiler was co-fired with coal and biomass that was loosely mixed prior to feeding into the hopper. During co-firing, the temperature in the boiler increased and the NOx levels increased as well. This increase in NOx is contradictory to many of the studies in the literature [5, 16] that indicate including biomass in the fuel reduces the NOx levels in the flue gases due to the lower levels of nitrogen in biomass compared with coal.

This study focused on evaluating the influence of blending biomass with coal on the heat production, ignitability, and emission gas composition aspects. The research considered the effects of the manner in which the fuels were blended (i.e., loosely mixed or formed briquettes) as well as the air flow into the fuel bed. For direct comparison of performance, the experimental study was performed using full size briquettes as well as a similar mass of loosely mixed fuel under the same thermal exposure. In addition to providing insight on the impact of these parameters on the fuel combustion, the experimental data were also used to assist in understanding the behavior of co-firing coal and biomass in real-scale boilers through comparison of the small-scale data with trends noted in the VT power plant.

8.2 Experimental procedure

8.2.1 Materials and preparation

The fuels tested for the study included EC, SG-Raw and CS-Raw feedstocks, which are the same as those mentioned in Section 4.2.1. However, the heat treatment of the feedstocks in this study was different than Section 4.2.1 to simulate the fuel conditions encountered during operation of a power plant. The feedstocks were air dried for about one day before further processing. Coal particles obtained were fine enough to pass through a 400 μm sieve (40 mesh) while biomass particles were sieved between 2.38-2.81 mm particle size (7-8 mesh), as shown in **Figure 44(a)**. The resultant moisture in EC-Raw was 2.35% by weight after natural drying. Moisture in SG-Raw was 16% and CS-Raw was 13% by weight after natural drying.

(a)

(b)

Figure 44: Fuel samples tested in this study, as shown from left to right: (a) EC, SG-Raw and CS-Raw (b) EC briquette, EC & SG-Raw 80:20 blend briquette and EC briquette, EC & CS-Raw 80:20 blend briquette

Powdered EC sample was blended with milled raw biomass feedstocks in a 80:20 coal-to-biomass ratio to form coal-biomass raw blends. The fuels and blends were also tested in briquetted forms. Pill shaped briquettes were prepared using a roll press briquetting machine (Komarek B-100R) without using any binding material. The method of briquette preparation and its durability analysis is discussed elsewhere [187, 189, 195].

In the current study, briquettes of EC, briquettes of EC and SG Raw mix in 80:20 ratio, and briquettes of EC and CS Raw mix in 80:20 ratio were developed to compare the combustion behavior of blended briquettes versus the combustion behavior of raw blends. These three types of briquettes are shown in **Figure 44(b)**. The average dimensions of briquettes were 43 x 23 x

13.5 mm with blend briquettes ~2 mm thicker than the coal pellets. On an average, the mass of a single briquette was 9.15 g. The density of EC briquettes was calculated to be 800 kg/m^3, while that of blend briquettes was calculated to be 635 kg/m^3 for SG-Raw blend briquette and 650 kg/m^3 for CS-Raw blend briquette.

8.2.2 Instrument and procedure

A bench-scale fixed-bed reactor was fabricated to quantify the performance of the fuels in a more realistic environment. As shown in **Figure 45(a)**, a grate system was placed in the test chamber of the cone calorimeter on top of the scale balance. The grate system was constructed from stainless steel, as shown in **Figure 45(b)**, and was insulated around the perimeter with high temperature ceramic fiber insulation board during tests to reduce heat losses to the surroundings. Air was naturally drawn up through the bottom of the grate to the fuel, which rested on an aluminum (Al) alloy plate. The Al alloy plate permits free air flow up through the fuel bed. The aluminum plate also collects any ash that falls through the grate so that the mass of the fuel during combustion can be accurately monitored. The heater in the cone calorimeter was set to 50 kW/m^2. Assuming a radiation dominated environment in a furnace, this heat flux is consistent with a furnace exposure temperature of approximately 738ºC.

Placing the grate system inside the cone calorimeter allows for continuous measurement of the mass loss rate of the fuel, time to fuel ignition, fuel burn time, heat release rate, and combustion products downstream of the reactor. The flammability behavior of a fuel can be monitored from clear glass windows surrounding the setup. The load cell in the cone calorimeter has an accuracy of 0.1 g, allowing for accurate mass measurements during the combustion experiments. A spark igniter was located between the fuel and the heater to ignite flammable combustion products during the experiment. The combustion products from the reactor were sampled in the exhaust and the NOx (Range 0-5000 ppb), CO (0-2000 ppm), CO_2 (0-5 volume %) and O_2 (0-25 volume %) concentrations were continuously measured. These concentrations along with the mass flow rate in the duct were used to determine the heat release rate applying the oxygen consumption principle in accordance with ASTM E-1354 [196]. The heat release rate data was used to calculate the effective heat of combustion of fuel [196].

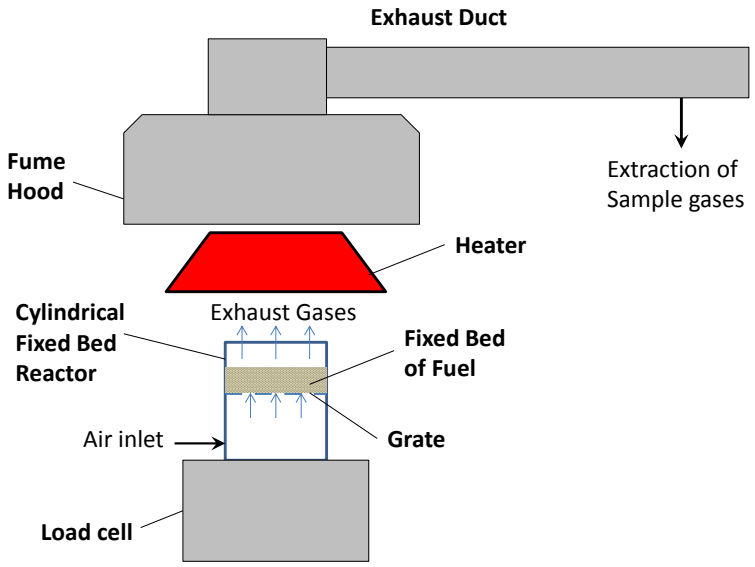

(a)

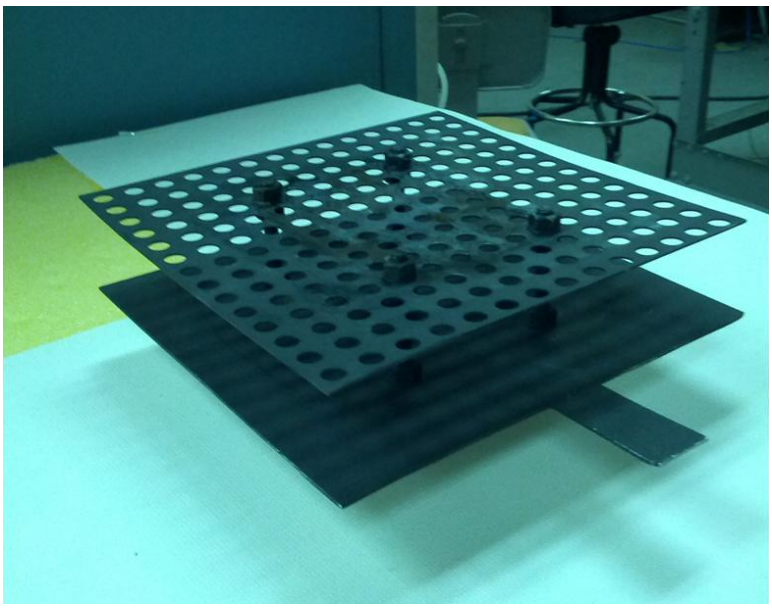

(b)

Figure 45: (a) Bench-scale fixed bed reactor inside the cone calorimeter (b) Stainless steel open grate system with aluminum pan at bottom. The system is painted with high temperature high emissivity black paint.

The cone heater temperature was set to 50 kW/m^2 for these experiments. The fuels, when kept in the reactor, were exposed to the heat flux for up to 1.5 hr duration. The fuels were combusted in two types of operating conditions that varies the combustion environment of fuels:

i. Al foil experiments: In these experiments, the fuel samples were kept on top of an aluminum foil. Thus, there was less oxygen available during the experiment. This case simulated a limited air supply condition that is being evaluated for low NOx emissions for the VT power plant. An example of this setup is shown in **Figure 46(a)** and **Figure 46(b)**.

ii. Open grate experiments: In these experiments, the grates are open at the bottom (no Al foil). Air was naturally drawn up through the bottom of the grate to the fuel and more air was available for combustion. An example of this setup is shown in **Figure 46(c)**. This case simulated the current conditions at the VT power plant where sufficient air is supplied during fuel combustion. However, only briquettes were tested for this configuration as the raw samples would just fall through the grate to the ash plate.

In both operating conditions, a ceramic insulation wall was applied to reduce heat losses.For briquette tests, six briquettes were kept in adjacent position while testing, as shown in **Figure 46(b)**. While testing raw fuel samples, an equivalent amount of raw fuel (~55 gm) was tested in the same operating conditions, as shown in **Figure 46(a)**. The test matrix in **Table 17** demonstrates all tests conducted in the study with an 'X' mark.

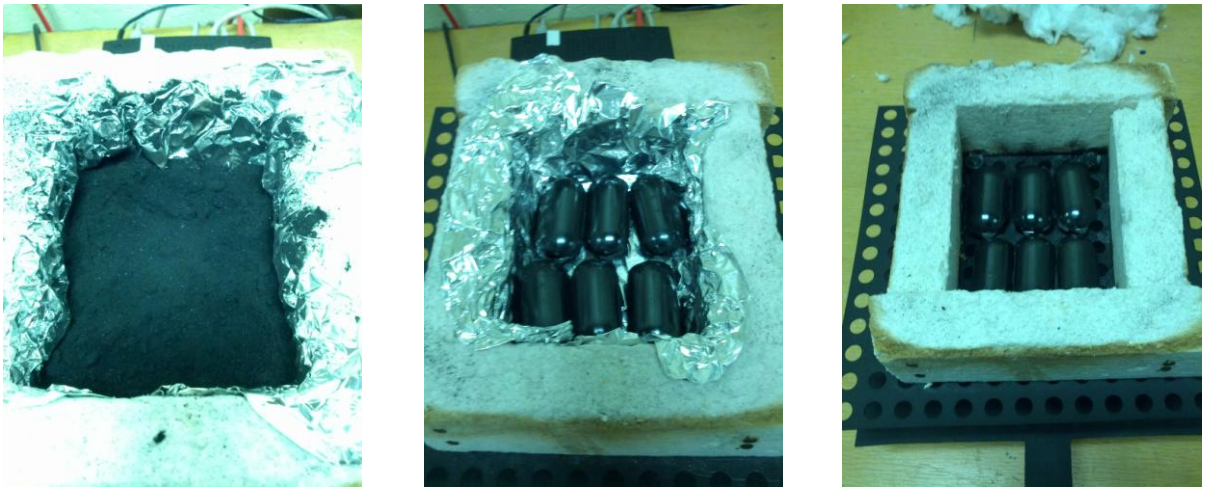

Figure 46: Three types of test conditions using EC fuel (a) Raw fuel in Al foil (b) Briquettes in Al foil (c) Briquettes in open grate system

Table 17: Test matrix for fuel briquetting study

Fuel type and nomenclature	Al foil system	Open grate
EC	X	
SG-Raw	X	
CS-Raw	X	
EC & SG-Raw 80:20 blend (Raw EC-SG blend)	X	
EC & CS-Raw 80:20 blend (Raw EC-CS blend)	X	
EC briquettes	X	X
EC & SG-Raw 80:20 blend briquette (EC-SG blend briquette)	X	X
EC & CS-Raw 80:20 blend briquette (EC-CS blend briquette)	X	X

8.3 Results and discussion

8.3.1 Flammability and combustion performance

Figure 47(a), **(b)** and **(c)** shows the final ash from the test cases shown in **Figure 46**. When combusted in Al foil, EC-Raw fuel in **Figure 47(a)** burnt with low flames. The coal particles on the upper layer swelled and shielded the inner coal particles from combusting. Upon further combustion, the upper swollen layer cracked and short flames emerged through the cracks until the fuel burnt out. After combustion, the topmost ash layer was removed and an un-burnt layer of lower level EC sample was found, as shown in **Figure 48(a)**.

When burnt as a briquette in Al foil, the EC-Raw fuel shown in **Figure 47(b)** showed more complete combustion. Since more surface area was available for combustion, the flame heights were found to be high. The flames not only originated from the top of the briquette but also from the bottom due to briquette shape. During the burning process, the upper layer of briquettes were combusting and peeling off with time while revealing the inner briquette layers. However, a small amount of char sample was left at the bottom of the Al foil when the upper layer of ash was removed, as shown in **Figure 48(b)**. This analysis shows that briquettes provides a better flammability performance than raw samples, but the briquette size can be made smaller for more efficient combustion.

Figure 47: After-combustion three types of test conditions using EC fuel (a) Raw fuel in Al foil (b) Briquettes in Al foil (c) Briquettes in open grate system

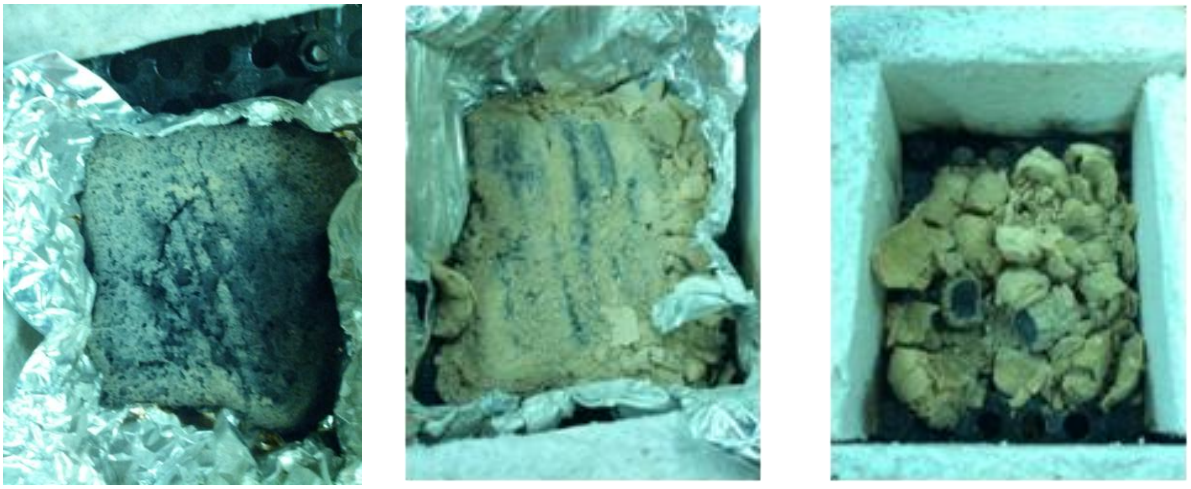

Figure 48: After-combustion three types of test conditions using EC fuel upon ash removal from upper surface (a) Raw fuel in Al foil (b) Briquettes in Al foil (c) Briquettes in open grate system

When EC briquette was burnt in an open grate system, the fuel showed even more complete combustion. As shown in **Figure 47(c)** and **Figure 48(c)**, the briquettes were completely combusted. With more air available for the combustion from bottom of the grate, the briquettes in this test cracked along the width instead of peeling. The flame size in this test was also found to be lower than that of briquettes with Al foil. **Figure 48(c)** also shows that even

though most of the briquettes were completely burnt in the 1.5 hr test, some of them had un-burnt interior left behind. Hence, development of smaller briquettes may provide more efficient combustion in open grate tests as well.

Figure 49(a) and **Figure 49(b)** provides the after combustion pictures of both blended briquettes (EC:SG-Raw and EC:CS-Raw) from open grate experiments. When compared to burnt briquette pictures of EC briquettes shown in **Figure 48(c)**, the biomass blended briquettes depicted complete combustion even on the inside of the sample. This was made possible due to the presence of high ignitability biomass in the briquettes, which provided higher flames and thus higher flame temperature to completely combust the insides of the blended briquettes. A similar result was found when same briquette combustion was compared for Al foil experiments, where higher flames and better combustion was found with the presence of biomass in the briquettes.

Figure 49: After-combustion two types of test conditions using blend briquettes upon ash removal (a) EC and SG-Raw briquette (b) EC and CS-Raw briquette

When the post-combustion results were compared for coal-biomass raw blends and coal-biomass briquette blends in the Al foil test, it was found that the briquette blends provided more complete combustion than raw mixture coal-biomass blends. The raw EC-biomass blend's flammability was hampered by the emergence of coal swelling on the upper layer of mixture. This in turn prohibited the lower levels of coal-biomass raw blends to completely combust.

These analyses shows flammability and combustion performance of briquettes were found to be better than that of raw fuel samples. It was also confirmed that the presence of biomass in briquettes favored the flammability and combustion performance of fuels in reactor operations.

This assertion was further validated with comparing the effective heat of combustion, Δh_{com}, data from different tests. The effective heat of combustion is calculated on the basis of amount of matter combusted during the process, i.e. total amount of energy released during combustion process divided by the total mass lost during the process. The effective heat of combustion for different tests for blended fuels is presented in **Table 18**.

Table 18: Effective heat of combustion for different blended fuel tests

Methodology → Fuel↓	Raw Blend (Al foil)	Briquette blends (Al foil)	Briquette blends (Open grate)	MCC[a] (**Table 11**)
EC:CS (80:20)	20.5	27.5	34.9	31.5
EC:SG (80:20)	23.5	26.0	30.8	30.0

[a] for Leached biomass blends with EC

As observed from **Table 18**, the Δh_{com} for briquette blends were found to be 10-25% higher than that for raw blends, when combusted in similar conditions (column 2 and column 3). This data confirms higher combustion performance of briquette blends in comparison raw blends. **Table 18** also confirms that the combustion performance from open grate experiments (column 4) provided better combustion performance than Al foil experiments for briquette blends (column 3). The heat of combustion data from MCC (column 5) for similar coal and leached biomass blends provided the similar Δh_{com} (**Table 11**) as that for the briquetted blends in open grate conditions. Although the Δh_{com} in **Table 11** was calculated as a weighted sum of

pyrolysis and char combustion processes, the results are still close for complete combustion of fuel blends. This analysis proves that (i) open grate combustion of blended briquettes do indeed go to complete combustion (ii) there is no loss in calorific value of fuels after briquetting. The heat of combustion data from MCC (**Table 11**), although form blend of EC and leached biomass, can be compared to that of blended EC and unwashed biomass briquettes because Δh_{com} of biomass is not affected due to water leaching (**Table 11**).

A further proof of combustion performance is provided by the final mass yield data of these runs. The final mass yield is defined as the ratio of final sample mass after combustion and the initial sample mass before combustion. A lower yield reveals a better combustion performance from a fuel blend. Table 19 provides the final mass yield data for the runs mentioned in **Table 19**.

Table 19: Final mass yield for different blended fuel tests

Methodology → Fuel↓	Raw Blend (Al foil)	Briquette blends (Al foil)	Briquette blends (Open grate)	MCC[a,b] (**Table 11**)
EC:CS (80:20)	0.43	0.27	0.08	0.09
EC:SG (80:20)	0.41	0.31	0.06	0.08

[a] for Leached biomass blends with EC, [b] $=Y_c * Y_{cc}$ from **Table 11**

As observed from **Table 19**, the blended briquettes provide 24-37% lower mass yield than raw blend combustion, thus confirming better performance from blended briquettes. The final yield of briquetted blends in open grate experiments was found close to that reported from MCC data as multiplication of Y_c and Y_{cc}, thus confirming more complete combustion of briquettes due to the presence of high flammability performing biomass.

The analysis from this section indicates the following: (i) flammability and combustion performance of briquettes is better than raw fuel (ii) presence of biomass in coal briquettes improves the performance of briquettes (iii) flammability, combustion performance, heat of combustion and final mass yield for blended briquettes is better than raw blends, and (iv) decreasing the briquette size may improve the flammability and combustion of briquettes.

8.3.2 Ignitability and burn duration

The ignitability, or the ignition time (t_{ig}), of a fuel is an important parameter that determines how quickly the fuel catches fire. Not only does this parameter determine the flame height, temperature, stability, extinction and emissions [193, 197], but a significant set of operating conditions of a reactor as well. Fuel with very low t_{ig} may burn before reaching the optimal position in a reactor, or may even ignite during fuel injection inside the fuel feeding chute. This kind of change in ignitibility of fuel is likely to happen in the case of coal and biomass co-firing and may lead to unsuspected drop in performance or unit failure/shutdown.

Ignitibility of a fuel is closely related to the off-gassing time (t_{off}) of the fuel, which is the time at which fuel starts producing pyrolysis gases when subjected to heat flux. An earlier off-gassing of fuel may release gases at non-optimal location where a significant part of it may remain un-combusted, thus leading to drop in reactor efficiency. An earlier off-gassing may also release gases at unsafe locations and lead to suffocation or fire related accidents.

The burn duration of a fuel (t_{burn}) represents the amount of time a fuel takes to completely burn out after ignition. A fuel with lower t_{burn} may indicate presence of flashpoints at which the significant part of fuel will burn in a short duration. Such flashpoints are undesirable for operation of reactors and may affect the life of critical components such as refractory. A lower burn time may also indicate that the fuel is not burning along the full length of conveyer belt, which may result in drop in plant efficiency. Thus, the change in operation of a furnace is be closely linked with the t_{burn} of the fuel.

In all coal based reactors, the operation of a plant is closely linked to t_{off}, t_{ig} and t_{burn} of the coal fuel. With the introduction of diverse fuel such as biomass, these parameters are bound to change and thus the operation of coal based plants should be changed in accordance. However, it is always desired that the amount of changes in the plant operation should be minimal. This is both due to limitations of the current coal based plants and also the costs associated with the same. Thus, a closer t_{off}, t_{ig} and t_{burn} of blended fuel to that of coal would be considered as a preferred fuel in terms of least changes in the plant operating conditions.

The present section seeks to find the effect of biomass addition to changes in these parameters for a coal based plant. It will then be evaluated whether the briquetting of fuel further brings t_{off}, t_{ig} and t_{burn} closer to that of coal-only operation.

Table 20 reports the t_{off}, t_{ig} and t_{burn} parameters for all fuels tested in this study using the Al foil setup.

Table 20: The t_{off}, t_{ig} and t_{burn} parameters for all fuels tested using Al foil setup

	Fuel type and nomenclature	t_{off} (s)	t_{ig} (s)	t_{burn} (s)
(i)	EC-Raw	17	45	935
	SG-Raw	2	4	466
	CS-Raw	2	3	317
(ii)	EC & SG-Raw 80:20 blend (Raw EC-SG blend)	2	4	976
	EC & CS-Raw 80:20 blend (Raw EC-CS blend)	2	3	867
(iii)	EC briquettes	20	70	1610
(iv)	EC & SG-Raw 80:20 blend briquette (EC-SG blend briquette)	14	21	1059
	EC & CS-Raw 80:20 blend briquette (EC-CS blend briquette)	10	33	1407

The first data in **Table 20** provides us with t_{off}, t_{ig} and t_{burn} parameters of EC-Raw burn at 50kW/m^2 as 17, 45 and 935 s respectively. These times represent the parameters for which an EC based power plant operating conditions must be designed. The times represent a delay in off-gassing of coal fuel, further delay in its ignition time and considerable burn duration, after which the coal fuel will undergo char oxidation.

The discussion for **Table 20** is divided in four parts from (i) to (iv). In each part, the effect of change in fuel is understood in terms of change in its t_{off}, t_{ig} and t_{burn} parameters from those of EC parameters. Based on the analysis, the effects of such changes on the possible operation of an EC based plant is discussed. Lastly, it is analyzed whether burning a certain fuel would be feasible in an EC based plant with minimal changes in plant's operating conditions.

i. <u>Feeding raw biomass in a EC based plant:</u>

The first discussion entails a situation where biomass feedstocks are fed into a EC based power plant. The t_{off}, t_{ig} and t_{burn} parameters for such scenario are listed in Row (i) of **Table 20**. It can be seen from the results that why feeding biomass into a coal-based reactor provides

a huge number of operational challenges. It can be seen that the t_{off}, t_{ig} and t_{burn} parameters for biomass are significantly lower than those of EC fuel. The fuel will off-gas and ignite at non-optimal locations (possibly the feeding chute) that will lead to a series of operational problems mentioned earlier in the section. The t_{burn} of biomass feedstocks is also very low, thus making it practically unfeasible to burn biomass feedstocks in a coal based plant with minimal operational changes.

ii. Feeding coal-biomass blends in an EC based plant:

The second discussion entails a situation where coal and biomass feedstocks are fed into a EC based plant in 80:20 ratio (Row ii). This scenario is similar to the one recently encountered by VT power plant where a series of operational issues were observed with the same situation. Even though the coal-biomass blends deliver near identical t_{burn} in comparison to that of EC samples, the t_{off} and t_{ig} times for blend burn correspond to those of biomass feedstocks. Thus the blended fuel will off-gas and ignite at non-optimal locations, providing high flames and emissions due to high flame temperature. This kind of operation will lead to loss in plant efficiency and other maintenance/safety issues. Thus, changing the operating conditions of the coal-based reactors to suit those of blended fuels would be an expensive and challenging task.

iii. Feeding EC briquettes in an EC based plant:

In the third scenario, a situation where EC briquettes are fed into a power plant designed for EC-raw feedstock is discussed. It can be seen from Row (iii) in **Table 20**, that the t_{off} of the EC-briquette (20s) is similar to that of EC-Raw feedstock (17s). The t_{ig} and t_{burn} time for EC-briquette are 55% and 70% higher than those of EC-Raw sample. Even though these differences are high, the change in operating conditions of EC-Raw based power plant to suit the EC-briquette based operation should not be as difficult as in case (i) and (ii). The changes that may be required to suit the new briquetted fuel may include lowering of conveyer belt speed or having higher heat fluxes to combust the briquette faster, among others.

However, as more and more coal based power plants are required to burn coal-biomass blends, the effect of biomass in a briquette must be understood in terms of changes in plant operation. This case will be important as in the previous discussion (Case ii), the presence of biomass dominated the burning characteristic of a blend, thus rendering it unfeasible.

iv. Feeding EC-biomass blend briquettes in an EC based plant:

In the fourth and final situation, a scenario is discussed where EC and biomass blend briquettes are fed into a power plant designed for EC-Raw feedstock. As observed from Row (iv) of **Table 20**, the t_{off} decreases slightly (by 3-7 s) for blended briquettes in comparison to t_{off} of EC-Raw sample. Also, the t_{ig} for blended briquettes (21 and 33 s) is comparable to that of EC-Raw sample (45 s). Both of these parameters (t_{off} and t_{ig}) for blended briquettes in Row (iv) are an improvement from the same parameters from raw blends in Row (ii), and are much closer to the parameters of EC-Raw sample. This analysis indicates that blended briquettes would require significantly lesser amount of operational changes in the EC based power plant, in comparison to if a raw coal-biomass blended fuel were used. Thus, the briquetting of biomass with a coal sample controls the ignitability properties of biomass and provides a better combustion/flammability behavior as well (Section 8.3.1).

In terms of t_{burn} parameter, the burn time of a blended briquette (1059-1407 s) is higher than that for EC-Raw sample (935 s). However, the t_{burn} of a blended briquette (1059-1407 s) in Row (iv) is also significantly lower than t_{burn} of EC-only briquette (1610 s) in Row (iii). This shows that usage of a blended briquette may be preferred over an EC-only briquette to keep the burn time as close to EC-Raw as possible. Thus, blended EC-biomass briquettes (in 80:20 ratio) may provide easier operation of power plant in comparison to EC-only briquettes.

The main points from the discussion in this section includes (i) Feeding biomass or coal-biomass mixtures in raw form may require highest amount of changes in coal-based plant operating conditions (ii) Feeding coal briquettes as a substitute fuel in a coal-based power plant will require less changes in the coal-based plant operating conditions. However, the high ignition delay and slow burn rate must be considered for such scenario. Also, the operation of coal-only briquettes will not earn carbon credits for not using renewable fuels (iii) Usage of coal-biomass blended briquettes will not only provide a scenario where least amount of changes would be required to operating conditions of a coal based power plant, but it was also improve the ignition delay and burn time in comparison to that of coal-only briquettes. Thus, the usage of coal-biomass blended briquettes not only improves the flammability and combustion performance of a coal-based power plant (Section 8.3.1), but it also requires lower amount of changes in the operating conditions of the same by controlling the ignitability properties of biomass fuels.

8.3.3 Emission gas profiles and yields

In the previous sections, it was determined that the flammability, combustion performance, ignitability and burn duration of blended briquettes is better than those of raw blends. In this section, the emissions entailing different fuels and operating conditions are analyzed.

Understanding the emission behavior of a fuel is very important in terms of its feasibility to use it in coal-based power plants. Even if the fuel provides better combustion performance and thermal efficiency, if the emissions from the combustion of fuels are higher than the regulatory standards then such fuel is not suitable for use in reactors.

In the literature, the understanding of emission behavior from coal-biomass blends has primarily been conducted in terms of data from a TGA setup. Usually the DTG peaks from thermogravimetric data are correlated to peak data of certain emissions [37, 39, 40, 116, 146, 179, 198, 199]. Other literature studies have conducted blend emission analysis in order to determine additive evolved gas behavior of coal and biomass samples on co-pyrolysis or co-combustion [2, 19, 44]. As discussed in previous sections, these analyses do not provide adequate data regarding briquette combustion in high heat flux environment. Some studies have characterized the emission data from fixed bed or other gasification setups [186, 200]. However, these studies have not conducted work on emission comparison from coal-biomass blend briquettes and other briquetted fuels.

As mentioned in Section 8.1, one of the primary motivations for this study was to solve the coal-biomass co-combustion problems related to the VT power plant. In a recent operation at VT power plant, it was found that the NOx levels increased when a coal-biomass co-firing was performed. Hence, the current section primarily focuses on NOx peak data from coal-biomass co-firing. The reasons behind the difference in NOx behavior from different fuels will be evaluated in terms of heat release rate (HRR) of the sample. Then the analysis of other important emission gases, such as CO_2 and CO will also be conducted.

Figure 50 shows the NOx profile behavior as a function of time for different tests conducted in this study. The average room NOx level (10-20 ppb) was subtracted from the actual NOx data to present data in **Figure 50**. The Savitzky-Golay smoothing [201] was applied on all cone calorimeter data collected in the experiments as a function of time (NOx, CO, CO_2, HRR). The time, t =0, represents the instant when the sample was introduced to 50 kW/m^2 heat flux.

Only the first 1100 s of data is showed in the below plot (and other plots in this section) in order to capture the main moments of t_{ig} until t_{burn} for most fuels.

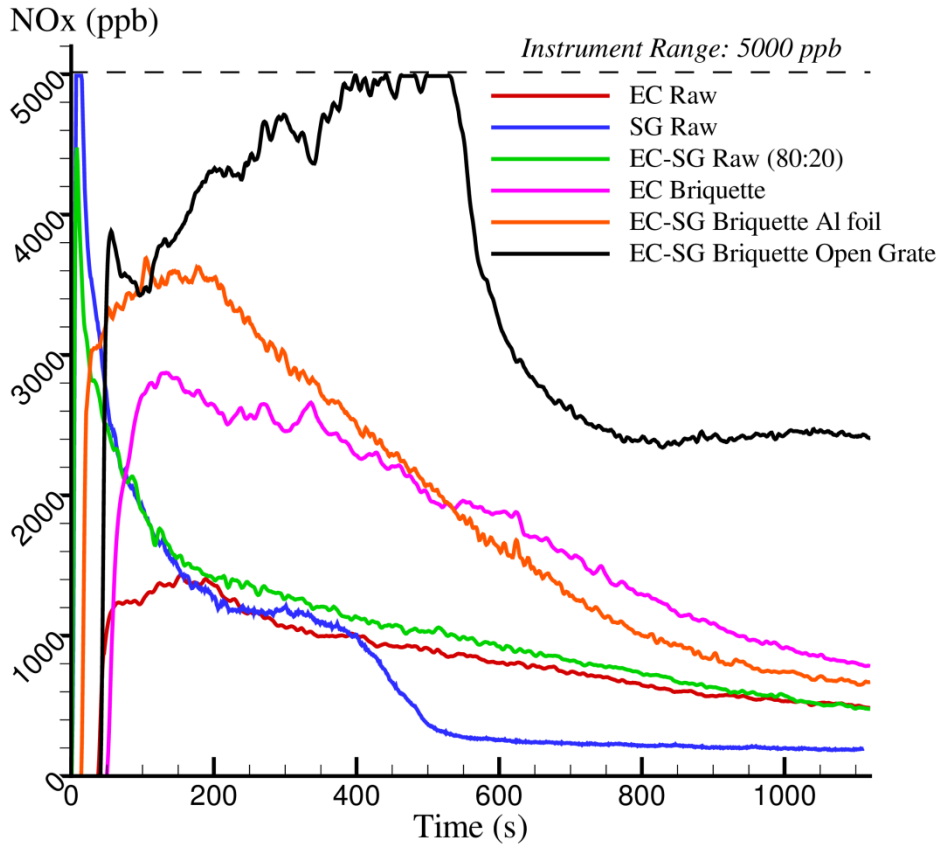

Figure 50: NOx profiles (in ppb) as a function of time for various experiments. (All experiments conducted with Al foil except for last legend)

The observations from **Figure 50** are discussed in the decreasing order of plot legend.

(i) The first curve shows the NOx profile from combusting EC-Raw sample in its powdered form (Red curve). As shown, the EC-Raw sample burns at t_{ig} of 45 s, thus providing increase in NOx level from zero ppb. The NOx levels gradually reach the peak levels of ~1400 ppb at ~150 s. Thereafter, the NOX levels gradually decrease with time until fuel burnout and subsequent char oxidation. This profile will be used as a representative of NOx data from a coal based power plant, and will be compared with data from other fuels.

(ii) The second curve (in blue) shows the NOx data for SG-Raw burning in same operating conditions. As observed, the SG sample burns instantaneously (t_{ig} = 3 s), thus producing high flames and high sample temperature. The NOx levels suddenly rises up to more than the range of the NOx instrument (5000 ppb). These kind of peaks can cross the regulatory limits and lead to furnace shutdowns, thus showing the incompatibility of biomass fuels in coal based furnaces. After initial peak, the NOx levels immediately decreases until burn-out time (t_{burn} = 466s). During char oxidation phase, the NOx levels stays low and decreases gradually.

(iii) The third curve (in green) shows the NOx profile for EC and SG Raw blend combustion. As observed, and as previously described in Sections 8.3.1 and 8.3.2, the coal-biomass raw blend burns in a manner similar to that of biomass rather than coal. Thus, the raw blend sample produces initial high flames and leads the peak NOx levels to as high as 4500 ppb. This high peak level of NOx simulates the similar problem encountered by the VT power plant while co-combusting coal and biomass raw blends. After the initial peak, the NOx levels gradually decrease in a manner similar to that of EC rather than biomass. This behavior of NOx pattern concurs with the t_{ig} and t_{burn} data for coal-biomass blend, where t_{ig} was found to be same as that of biomass and t_{burn} same as that of EC-Raw burn in **Table 20**.

(iv) The fourth curve (pink) shows the NOx profile for EC-briquette burnt in similar conditions. As seen from **Figure 50**, the NOx profile for EC-briquette combustion follows the similar profile as that of EC-Raw combustion. However, due to higher flames in EC-briquette (Section 8.3.1), the peak NOx levels (2800 ppb) produced are higher than that of EC-Raw sample. The decrease in NOx levels after peak is less gradual than that of EC-Raw sample combustion. Hence, it can be seen that usage of EC-briquettes would provide a similar combustion profile than that of EC-Raw sample which in turn will help the operational changes of the plant. The higher peak level of NOx from EC-briquette, if not higher than the regulatory standards, will require further changes in the operational procedure of a power plant.

(v) The fifth curve (shown in orange) depicts the NOx profile for EC-SG briquette blend in same conditions. This curve follows the same profile as that of EC-Raw and EC-briquette combustion, and would require lesser changes in the operating conditions of a power plant. Although, the NOx peak level for blend briquette combustion is found to be higher than that of EC-Raw sample combustion, the peak levels for the blend briquette combustion were also found to be much lower than peak levels from raw blend combustion (green curve). Thus, the present study favors the usage of blended briquettes in comparison to that of raw blends for lower peak NOx emissions.

(vi) The sixth and the last curve (black) represents the blended briquette combustion in Open Grate experiments where higher amount of air (and hence N_2) was available for fuel combustion. This is the only case in **Figure 50** that depicts profile for Open Grate combustion as the rest of the five tests were conducted with Al Foil, where limited air is available during fuel combustion. As shown for this case, the NOx levels at the initial ignition of the fuel were higher than that of blended briquette burning with Al foil (5th case, orange). The NOx levels then gradually increase to more than the range of NOx instrument. The NOx levels remain more than 5000 ppb for significant time (~150 s) during combustion before the sample burns out and char oxidation takes place. This experiment shows that in order to obtain lower peak level of NOx from Coal-biomass briquette combustion, the amount of air and hence the amount of N_2 available should be reduced. In an existing coal-based power plant like that at Virginia Tech, this operating condition can be controlled by lowering the air blower speed of fans located at the bottom of the conveyer belt.

The last analysis shows that NOx generation during coal-biomass fuel combustion is dependent of N_2 level (in air) and not particularly on the N content of the fuel. The **Figure 51** shows the HRR data for all the test cases shown in **Figure 50**. As observed, the profiles of HRR and NOx data are similar in nature. This observation depicts that the NOx levels are controlled by the Zeldovich (or thermal) mechanism, where the higher flame temperature in presence of N_2 produces higher NOx during hydrocarbon combustion [202].

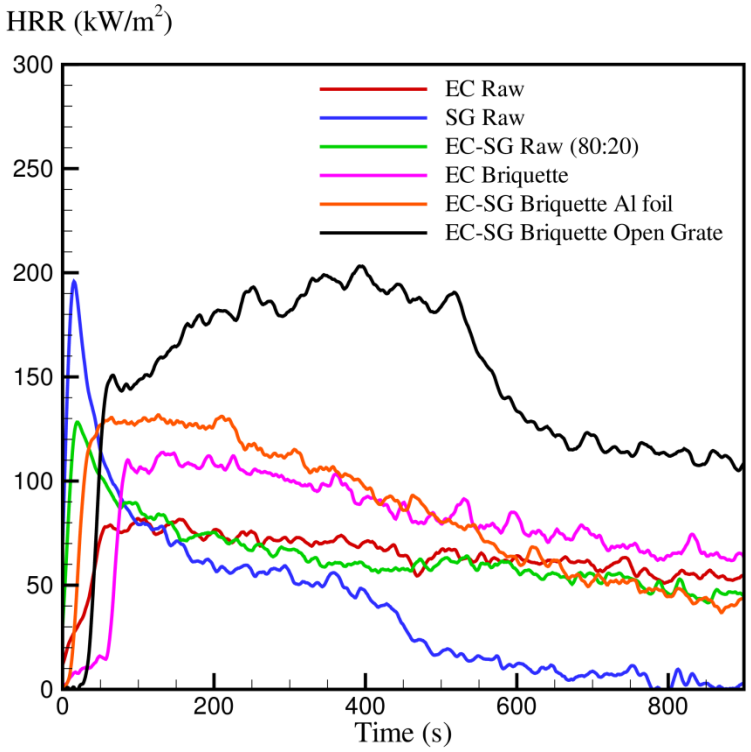

Figure 51: HRR profiles (in kW/m^2) as a function of time for various experiments. (All experiments conducted with Al foil except for last legend)

Figure 51 also provides important data regarding fuel combustion. It can be seen that as combustion of EC-Raw (red curve) provides a uniform and high HRR with time, the biomass combustion (blue curve) provides a flash of heat at ignition and substantially lower HRR afterwards. The EC-briquette combustion (pink curve) provides higher HRR than that of EC-Raw combustion (red curve), which indicates better combustion performance from coal briquettes in comparison to raw coal. The HRR of blended briquettes (orange curve) was found much higher and uniform along time than the HRR of raw blends (green curve). The presence of more air in Open grate system (black curve) provided more HRR than that in Al foil for blended briquettes (pink curve).

Figure 52 shows the CO_2 profiles for all the test cases depicted in **Figure 50**. As observed, the CO_2 profiles for all the tests are similar to those of NOx and HRR profiles shown in **Figure 51** and **Figure 52** respectively. Hence, the discussion for the CO2 profiles is also similar in nature. However, for gases like CO and CO_2 the power plants are more concerned

about the total yields rather than the peak values. The yield discussion for these gases will be conducted later in this section.

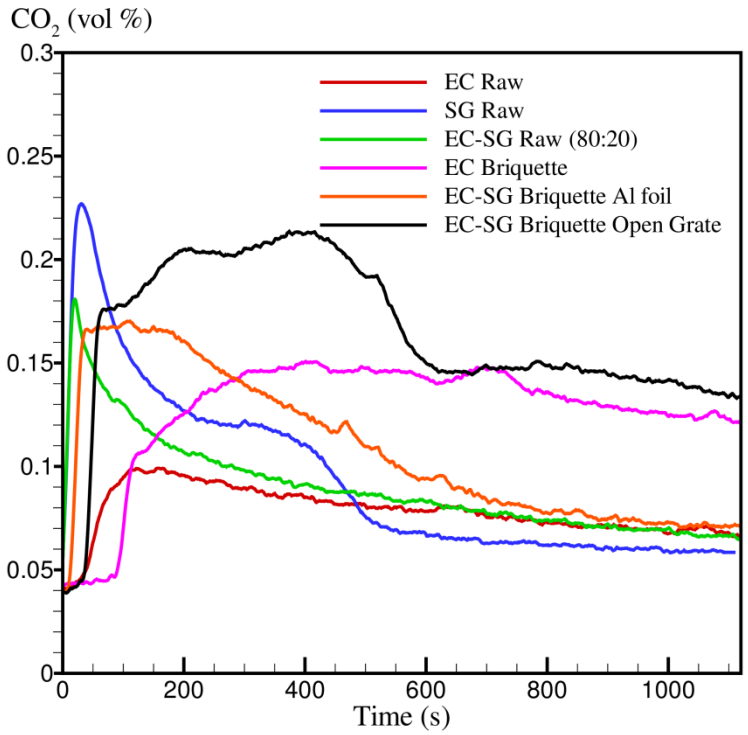

Figure 52: CO_2 profiles (in volume %) as a function of time for various experiments. (All experiments conducted with Al foil except for last legend)

Figure 53 shows the CO profiles for all the test cases depicted in **Figure 50**. The CO profiles are different than those of NOx, HRR and CO_2. This is because CO_2 formation is predominant during the flaming combustion and CO formation is dominant during the non flaming char oxidation after sample burn out (smoldering). Thus in all test cases, the CO profiles have been seen rising as the combustion progresses. As seen from CO profile for biomass combustion (blue) which shows full cycle of fuel burn, the CO levels increase with time until the sample burns (t_{burn} = 466s). During char smoldering, the CO levels decrease gradually or remain relatively constant (as in case for coal based fuels) until the end of tests. For some coal based fuel CO profile (all except pink curve), an initial spike in the CO formation was observed with an instantaneous decrease, which may indicate a different mechanism of CO generation for ignition instant when high flames were present.

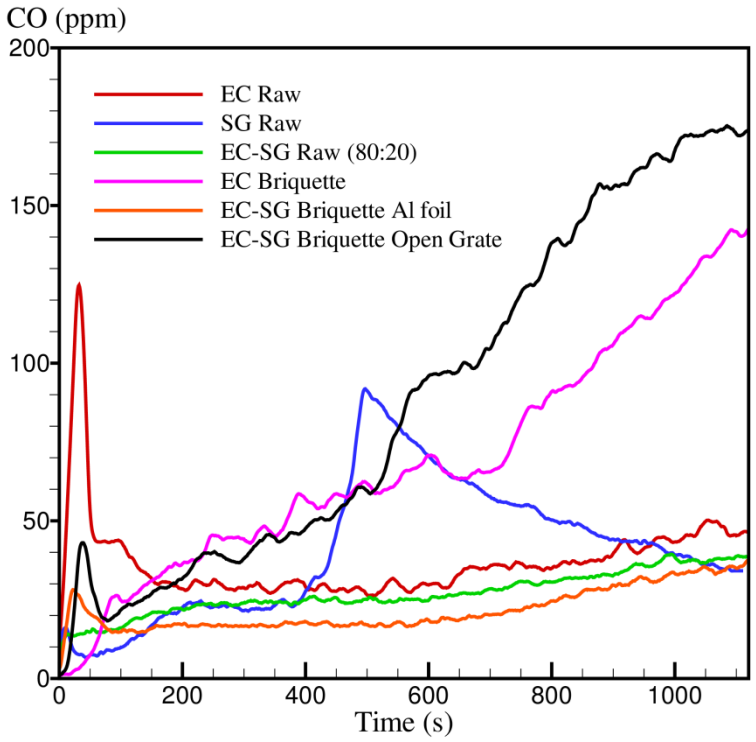

Figure 53: CO profiles (in ppm) as a function of time for various experiments. (All experiments conducted with Al foil except for last legend)

The yields for NOx, CO_2 and CO gases were calculated as per the Eqn. (22).

$$Yield = \frac{\int X_{gas} \times \dot{m}_e}{\Delta m_{fuel}} \tag{22}$$

Here, *Yield* represents unitless yield for emission gas (NOx, CO_2 or CO). X_{gas} represents the mass fraction of the gas in exhaust stream of cone calorimeter. $\dot{m}_e$ is the mass flow rate in the exhaust stream and Δm_{fuel} is the net mass loss of the fuel during the combustion process. The yield data for gases (NOx, CO_2 and CO) is mentioned in **Table 21** for the tests discussed in **Figure 50**.

Looking at the yield values for NOx test, it was found that the EC-briquette provides higher NOx yield than yield form the EC-Raw combustion, and similarly blend Briquette provides higher NOx yield than raw blend. Therefore, although the peak NOx values are lower for briquette combustion, their NOx yields are higher than combustion of raw fuel. However, as discussed previously, the peak values of NOx may be more significant parameter for a power

plant rather than the NOx yield values. The coal-biomass blending reduced the NOx yields, both in comparison to EC-Raw and EC-briquette cases. It was also found that limiting the air (and hence N_2) during combustion significantly reduces the NOx yield of the briquetted fuel.

Table 21: Yield data for NOx, CO_2 and CO gases for various experiments

Yield → / Fuel and process ↓	NOx (*0.001)	CO_2 (* 1.0)	CO (*0.1)
EC-Raw (Al foil)	4.57	7.60	3.64
SG-Raw (Al foil)	2.21[+]	2.65	7.00
EC-SG Raw in 80:20 ratio (Al foil)	3.83	5.88	2.67
EC-Briquette (Al foil)	6.49	6.99	2.32
EC-SG Briquette (Al foil)	5.39	5.47	1.68
EC-SG Briquette (Open grate experiment)	8.04[+]	5.22	3.04

[+] NOx levels crossed the range of the instrument, hence underestimated values

The data on CO_2 yield reveals that CO_2 yields are lower for biomass combustion that coal combustion. Hence, combustion of coal and biomass blend in raw form produces lower CO_2 yield than the combustion of EC-Raw. Similarly, combustion of blended briquettes produced lower CO_2 yield than combustion of EC-briquette. It is also observed that the CO_2 yield from combustion of briquetted fuel is lower than that of raw fuel. Thus, the combustion of briquetted fuel may be favored for reducing the green house gas emissions.

The data on CO yield reveals that CO yields are higher for biomass combustion than coal combustion. However, the CO yields for blended fuel combustion (both in raw and briquetted forms) was found to be lower than the CO yield of EC-Raw combustion. The CO yields for briquetted fuels were found to be lower than the CO yields for similar constituent fuels. It was also observed that limiting the air supply during combustion reduced the CO yield for blended briquetted fuel.

8.3.4 Conclusions

A combustion setup was develop to understand the effect of fuel briquetting on the flammability, ignitability, combustion performance, burn duration and emissions of the fuel. Coal, biomass feedstock and blends were used in the study. Coal briquettes and coal-biomass blend briquettes were also tested. The fuels were tested in different combustion environments to study its effects on fuel combustion behavior.

The fuel flammability observations were made from flame behavior. The combustion performance of the fuel was evaluated in terms of final mass yield and effective heat of combustion, Δh_{com}. It was found that the flammability and combustion performance of blended briquettes were better than those of raw blended fuels. It was further noticed that reducing the size of briquettes may help improve the flammability and combustion performance of tested briquettes.

The fuel off-gassing time, ignitability and burn duration were measured in these tests. It was found that the fuel off-gassing time, fuel ignition time and fuel burn duration for blended coal-biomass briquettes were close to that of coal. It was further concluded that for an existing coal-based power plant, usage of blended briquettes may require least amount of changes in its operation conditions. In turn, usage of just raw blends of coal and biomass will require considerable operational challenges in a coal-based power plant.

In terms of peak NOx emissions, it was concluded that the usage of blended briquettes will provide lower NOx peak values than raw blends of coal and biomass fuels. The CO_2 and CO yields from blended briquette combustion were found to be lower than that from raw coal and biomass blend combustion.

The heat release rate profile for blended briquette was higher and more uniform than the heat release rate profile for coal-biomass raw blends. These profiles for blended briquettes were also found to be more similar to that of coal and coal briquette heat release rate profiles.

Together with all these factors, it was determined that usage of coal-biomass blended briquettes will not only provide a scenario where least amount of changes would be required to operating conditions of a coal based power plant, but it will also improve the combustion behavior of fuels in terms of flammability, combustion performance, ignitability, burn duration and emissions from constituent raw fuels.

9. RESEARCH CONCLUSIONS

The current study was conducted owing to the challenges associated with the co-firing of coal and biomass fuels in power plants. These challenges includes developing a proper understanding of the co-firing behavior of blended coal-biomass fuels, and study the operation of advanced gasification systems used for converting such blended fuels to energy.

A rectangular cold-flow fluidized bed setup was developed to study the evolution of inlet gas jets located at the distributor. Experiments were conducted with varying distributor types and bed media to understand the motion of particles and jets in the grid-zone region of a fluidized bed. Particle Image Velocimetry and Digital Image Analysis were used to quantify the parameters that characterize these jets. The effects of fluidization velocity, particle diameter, particle density, distributor orifice diameter, and distributor orifice pitch on solid circulation of a fluidized bed were investigated. It was determined from this study that the solid circulation rate linearly increased with an increase in the fluidization velocity until the multiple jet system transitioned from isolated to an interacting system. In the interacting system of jets, the solid circulation increased with fluidization velocity but at a much lower rate. For multiple jet systems, this phenomenon may indicate the presence of an optimum operating condition with high circulation rate and low air input in the bed.

The pyrolysis-combustion behavior of pulverized coal-biomass blended fuels was quantified on the basis of their physicochemical, kinetic, energetic and evolved gas analysis during pyrolysis and combustion. Fuel pyrolysis and combustion performance models were developed to quantify the performance of blended fuels. The effect of briquetting of pulverized blended fuels was also analyzed to find solutions related to coal and biomass co-firing by developing a bench scale fuel combustion setup.

The Environmental Scanning Electron Microscope (ESEM) was used to analyze the physicochemical properties of blended fuel, char and pyrolyzed ash samples. The effects of biomass water leaching on the physicochemical behavior of biomass fuels and physicochemical interactions within coal-biomass fuel mixtures during pyrolysis were investigated. A significant reduction in inorganic salts was observed due to biomass leaching. Physicochemical property differences between coal and biomass samples were demonstrated in their un-pyrolyzed, char and ash phases. The physicochemical interactions between coal and leached biomass sample, following co-pyrolysis, were found to be minimal.

Thermogravimetric (TG) data was obtained from a simultaneous thermogravimetric analyzer (STA) for coal-biomass fuel blends undergoing co-pyrolysis at multiple constant heating rates. Non linear regression analysis was conducted on the TG data to determine the Arrhenius kinetic parameters for fuel blend co-pyrolysis. From the analysis of the TG and differential TG (DTG) data, it was determined that coal and leached biomass fuel blends depict an additive TG behavior during co-pyrolysis. Based on this conclusion, the Arrhenius kinetic parameters for the fuel blends were predicted from those parameters from the individual coal and biomass samples. It was found that a five independent n^{th} order reaction statistically best describes the co-pyrolysis behavior of fuel blends, with the first three reactions corresponding to the decomposition of biomass and the last two corresponding to the decomposition of coal. The Arrhenius parameters for the blend co-pyrolysis fitted the experimental TG data, thus showing an additive thermogravimetric and kinetics behavior for coal-biomass fuel blends.

The energetic behavior of coal-biomass fuel blends undergoing pyrolysis-combustion process was investigated using a STA and a micro-scale combustion calorimeter (MCC). The instruments were used to generate differential scanning calorimetry (DSC) and heat release rate (HRR) signals for the blended fuels. Mathematical models were developed for fuels undergoing pyrolysis-combustion, and experimental signal data was applied onto the models to calculate the heat of pyrolysis and heat of combustion properties for the fuel blends.

The mathematical models and the approach developed in this work was applied on samples such as glycerol, polymers, composites and cardboard. The heat of pyrolysis and heat of combustion data generated from these tests was validated against the literature findings to properly understand their energetic behavior during pyrolysis-combustion. The approach was then applied onto coal-biomass fuel blends to quantify their energetic behavior in terms of the properties of constituent fuels of the blends. It was found that the pyrolysis-combustion energetic signals and properties for coal-biomass blended fuel exhibited a weight additive behavior. It was further validated and concluded that the weighted sum prediction for the heat of pyrolysis and the heat of combustion properties for coal-biomass fuel blends must be conducted on the basis of their individual volatile mass contributions from constituent fuels and not on the basis of initial fuel mixture proportion. This should also happen because the energetic properties such as heat of pyrolysis and heat of combustion are calculated on the volatile mass basis of the fuel samples, instead on their initial mass basis.

To further the understanding of coal-biomass blend pyrolysis-combustion behavior, a study on of fuel blend performance was conducted. Lumped mathematical models were developed to calculate fuel pyrolysis performance, char combustion performance and cumulative fuel combustion performance. The models were developed to calculate both temperature based performance and total integrated performance of fuels and blends. The experimental data for model application was generated using a STA and a MCC. Using temperature dependent performance parameters, it was shown that different fuels produce peak performance at different temperatures. Thus, the mixing of various fuels will help blended fuels in generating consistent performance over a wider temperature range, which in turn can be advantageous for power plant operation. The blending of coal and leached biomass fuels in 80:20 ratio was evaluated in terms of total integrated performance parameters. It was found that the blending of biomass increases the pyrolysis performance of coal by 21-33%. However, the blending of biomass decreased the char combustion performance of coal samples by 28%. Thus, blending of biomass decreased the cumulative fuel combustion performance of coal by 22%. This performance drop due to blending signifies the amount of extra mass of mixture fuel that would needed to be fed into a co-firing plant in order to obtain the same performance as coal-alone combustion plant.

Lastly, a combustion setup was developed to understand the effect of fuel briquetting on the flammability, ignitability, combustion performance, burn duration and emissions of the fuel. Coal-biomass blend briquettes were developed and their combustion behavior was compared against raw coal-biomass blends of same mixture proportion. The fuel blends were also tested in different combustion environments to study its effects on combustion behavior.

It was found that the flammability and combustion performance of blended briquettes were better than those of raw blended fuels. The off-gassing time, ignitability and burn duration of blended coal-biomass briquettes combustion were found to be close to that of coal-only combustion. The heat release rate profile for blended briquette was higher and more uniform than the heat release rate profile for coal-biomass raw blends. In terms of peak NOx emissions, it was concluded that the usage of blended briquettes will provide lower NOx peak values than raw blends of coal and biomass fuels. The CO_2 and CO yields from blended briquette combustion were found to be lower than that from raw coal and biomass blend combustion. It was thus concluded that for an existing coal-based power plant, usage of blended briquettes may require

least amount of changes in its operating conditions. In turn, usage of just raw blends of coal and biomass will require considerable operational challenges in a coal-based power plant.

Together with all these factors, it was determined that usage of coal-biomass blended briquettes will not only provide a scenario where least amount of changes would be required to operating conditions of a coal based power plant, but it will also improve the combustion behavior of fuels in terms of flammability, combustion performance, ignitability, burn duration and emissions from constituent raw fuels.

10. FUTURE WORK

In the future studies, the fuel blend pyrolysis-combustion behavior investigation can be further extended to develop more sophisticated decomposition models for fuels undergoing co-pyrolysis and co-combustion. The focus can be shifted from loosely packed pulverized coal-biomass mixtures to energy-dense blended fuel briquettes. Hence, the physicochemical behavior, kinetics analysis, energetic model development and performance estimations must be investigated for such blended briquetted fuels.

The focus can also be shifted to more realistic reactor conditions in order to develop comprehensive models and experiments. For example, the experiments to understand the coal-biomass behavior can be done on larger scale setups and with higher heat fluxes or heating rates (similar to those in the power plant) than used in the presented study. These experiments will help the research group in developing more comprehensive mathematical models that can quantify the kinetics, energetics, performance and evolved gas behavior of thermally thick samples, rather than milligram size samples covered in the present study. A more sophisticated approach to determine decomposition process in a thick solid fuel sample would need to be developed. Therefore, the models and experiments will be able to quantify the briquette combustion process in terms of briquette cracking, volatile gas production, fuel ignition, flame spread and radiation effects, re-radiation from adjacent briquettes, and their subsequent effect on the modeled/experimented briquette.

The physicochemical analysis in such a study will focus more on briquette physicochemical behavior while under exposure from extreme thermal conditions. The thermo-mechanical properties of briquettes must be analyzed to determine briquette cracking, peeling and crumbling while under thermo-mechanical stress. The elemental analysis of the un-pyrolyzed, charred, and ash briquette must be conducted to understand its thermo-chemical behavior during the combustion process.

New kinetic models must be developed that can account for both pyrolysis and combustion processes occurring simultaneously at high heating rates (or high heat fluxes). Such comprehensive kinetics models should be flexible enough to accommodate varying combustion environments with different percentages of oxygen gas during co-firing process.

More comprehensive energetic models must be developed that can simultaneously quantify the energetic properties of fuel relating to both pyrolysis and combustion. As mentioned

previously, any such approach should be developed for thermally thick samples that can include the effects of briquette cracking, flame spread and re-radiation effects from adjacent briquettes. This approach should be developed based on the actual kinetics of the briquette combustion process, and thus should be flexible for varying combustion atmospheric levels.

The emission gas behavior must be correlated with the physicochemical, kinetic and energetic behavior and similar models must be developed to complete the understanding of emission gas behavior. Apart from NOx, CO_2 and CO gases, other pollutant gases (such as SOx) and non-pollutant gases (such as CH_4, H_2 and H_2O) must also be quantified to completely understand the emission gas behavior. Advanced chromatography techniques such as GC-MS, GC-FID and GC-TCD can be used apart from rack analyzers to attain this objective.

Such models will be able to better predict the performance of different briquetted fuel blends in actual power plant environment, and will also be able to indicate possible improvements in the fuels, briquetting process and reactor operating conditions that will be beneficial for the power plant efficiency.

Apart from developing realistic experiments and comprehensive models for better understanding of briquette combustion behavior, a significant effort must also directed towards optimizing the briquette preparation technology to develop high performance briquettes for power plant operation. The briquette size must be optimized for complete combustion of the same during the limited time of the combustion process in the power plant, as any un-combusted inner parts of briquettes will decrease the efficiency of the plant. This study would also require a better understanding of the thermo-mechanical and thermo-chemical behavior of the briquettes, thus leading to a future study related to briquette size optimization. The improvement briquetting technology should also be understood in terms of trying different coal-biomass blend ratios, testing briquette blends with more than two fuels, and analyzing different binding agents/techniques to make optimized briquettes for future power operation.

Lastly, the research group should also invite diverse stakeholders in the project that can contribute to the various aspects of briquette combustion physics, briquette size optimization, pilot-scale power plant with traditional and advanced combustion systems, and numerical modeling teams that can help further the understanding of pyrolysis-combustion behavior of briquetted fuel blends.

REFERENCES

[1] Van de Velden, M., Baeyens, J., Brems, A., Janssens, B., and Dewil, R., 2010, "Fundamentals, kinetics and endothermicity of the biomass pyrolysis reaction," Renewable Energy, 35(1), pp. 232-242.

[2] Biagini, E., Barontini, F., and Tognotti, L., 2006, "Devolatilization of Biomass Fuels and Biomass Components Studied by TG/FTIR Technique," Industrial & Engineering Chemistry Research, 45(13), pp. 4486-4493.

[3] Zinoviev, S., Müller-Langer, F., Das , P., Bertero , N., Fornasiero , P., Kaltschmitt , M., Centi , G., and Miertus, S., 2010, "Next-Generation Biofuels: Survey of Emerging Technologies and Sustainability Issues," ChemSusChem, 3(10), pp. 1106-1133.

[4] Senneca, O., Chirone, R., Masi, S., and Salatino, P., 2002, "A Thermogravimetric Study of Nonfossil Solid Fuels. 1. Inert Pyrolysis," Energy & Fuels, 16(3), pp. 653-660.

[5] Osvalda, S., 2007, "Kinetics of pyrolysis, combustion and gasification of three biomass fuels," Fuel Processing Technology, 88(1), pp. 87-97.

[6] Kumar, A., Jones, D., and Hanna, M., 2009, "Thermochemical Biomass Gasification: A Review of the Current Status of the Technology," Energies, 2(3), pp. 556-581.

[7] A.V, B., 2003, "Renewable fuels and chemicals by thermal processing of biomass," Chemical Engineering Journal, 91(2–3), pp. 87-102.

[8] Hamelinck, C. N., and Faaij, A. P. C., 2006, "Outlook for advanced biofuels," Energy Policy, 34(17), pp. 3268-3283.

[9] Fischer, G., and Schrattenholzer, L., 2001, "Global bioenergy potentials through 2050," Biomass and Bioenergy, 20(3), pp. 151-159.

[10] Hoogwijk, M., Faaij, A., van den Broek, R., Berndes, G., Gielen, D., and Turkenburg, W., 2003, "Exploration of the ranges of the global potential of biomass for energy," Biomass and Bioenergy, 25(2), pp. 119-133.

[11] Perlack, R. D., United States. Dept. of, E., United States. Dept. of, A., and Oak Ridge National, L., 2005, Biomass as feedstock for a bioenergy and bioproducts industry : the technical feasibility of a billion-ton annual supply, Oak Ridge National Laboratory, Oak Ridge, TN.

[12] Bruce C. Gates, George W. Huber, Christopher L. Marshall, Phillip N. Ross, Jeffrey Siirola, and Wang, Y., 2008, "Catalysts for Emerging Energy Applications."

[13] Andrew J, M., 2005, "Coal gasification for advanced power generation," Fuel, 84(17), pp. 2222-2235.

[14] Biagini, E., 2002, "Energy and Material Recovery by Thermal Treatments of Biomasses and Wastes (Co-combustion, Pyrolysis and Gasification)," PhD Thesis, Università di Pisa (Italy).

[15] Van Krevelen, D. W., 1950, "Graphical-statistical method for the study of structure and reaction processes of coal," Fuel (Guildford), 29(12), p. 269.

[16] Munir, S., Nimmo, W., and Gibbs, B. M., 2010, "Co-combustion of Agricultural Residues with Coal: Turning Waste into Energy," Energy & Fuels, 24(3), pp. 2146-2153.

[17] Khelfa, A., Finqueneisel, G., Auber, M., and Weber, J., 2008, "Influence of some minerals on the cellulose thermal degradation mechanisms," Journal of Thermal Analysis and Calorimetry, 92(3), pp. 795-799.

[18] Arvelakis, S., Jensen, P. A., and Dam-Johansen, K., 2004, "Simultaneous Thermal Analysis (STA) on Ash from High-Alkali Biomass," Energy & Fuels, 18(4), pp. 1066-1076.

[19] Park, D. K., Kim, S. D., Lee, S. H., and Lee, J. G., 2010, "Co-pyrolysis characteristics of sawdust and coal blend in TGA and a fixed bed reactor," Bioresource Technology, 101(15), pp. 6151-6156.

[20] Darvell, L. I., Jones, J. M., Gudka, B., Baxter, X. C., Saddawi, A., Williams, A., and Malmgren, A., 2010, "Combustion properties of some power station biomass fuels," Fuel, 89(10), pp. 2881-2890.

[21] Cozzani, V., Petarca, L., and Tognotti, L., 1995, "Devolatilization and pyrolysis of refuse derived fuels: characterization and kinetic modelling by a thermogravimetric and calorimetric approach," Fuel, 74(6), pp. 903-912.

[22] Sinha, S., Jhalani, A., Ravi, M. R., and Ray, A., 2000, "Modeling of Pyrolysis in Wood: A Review," SESI Journal, 10(1), pp. 41-62.

[23] Raveendran, K., Ganesh, A., and Khilar, K. C., 1996, "Pyrolysis characteristics of biomass and biomass components," Fuel, 75(8), pp. 987-998.

[24] Strezov, V., Moghtaderi, B., and Lucas, J., 2003, "Thermal study of decomposition of selected biomass samples," Journal of Thermal Analysis and Calorimetry, 72(3), pp. 1041-1048.

[25] Stenseng, M., Jensen, A., and Dam-Johansen, K., 2001, "Investigation of biomass pyrolysis by thermogravimetric analysis and differential scanning calorimetry," Journal of Analytical and Applied Pyrolysis, 58–59(0), pp. 765-780.

[26] Gomez, C., Velo, E., Barontini, F., and Cozzani, V., 2009, "Influence of Secondary Reactions on the Heat of Pyrolysis of Biomass," Industrial & Engineering Chemistry Research, 48(23), pp. 10222-10233.

[27] Vovelle, C., Mellottée, H., and Delbourgo, R., 1982, "Kinetics of the thermal degradation of cellulose and wood in inert and oxidative atmospheres," Symposium (International) on Combustion, 19(1), pp. 797-805.

[28] Ward, S. M., and Braslaw, J., 1985, "Experimental weight loss kinetics of wood pyrolysis under vacuum," Combustion and Flame, 61(3), pp. 261-269.

[29] Grønli, M. G., Várhegyi, G., and Di Blasi, C., 2002, "Thermogravimetric Analysis and Devolatilization Kinetics of Wood," Industrial & Engineering Chemistry Research, 41(17), pp. 4201-4208.

[30] Branca, C., Albano, A., and Di Blasi, C., 2005, "Critical evaluation of global mechanisms of wood devolatilization," Thermochimica Acta, 429(2), pp. 133-141.

[31] Várhegyi, G. b., Chen, H., and Godoy, S., 2009, "Thermal Decomposition of Wheat, Oat, Barley, and Brassica carinata Straws. A Kinetic Study," Energy & Fuels, 23(2), pp. 646-652.

[32] Hashimoto, K., Hasegawa, I., Hayashi, J., and Mae, K., 2011, "Correlations of kinetic parameters in biomass pyrolysis with solid residue yield and lignin content," Fuel, 90(1), pp. 104-112.

[33] White, J. E., Catallo, W. J., and Legendre, B. L., 2011, "Biomass pyrolysis kinetics: A comparative critical review with relevant agricultural residue case studies," Journal of Analytical and Applied Pyrolysis, 91(1), pp. 1-33.

[34] Bradley, L. C., Miller, S. F., Miller, B. G., and Tillman, D. A., 2011, "A Study on the Relationship between Fuel Composition and Pyrolysis Kinetics," Energy & Fuels, 25(5), pp. 1989-1995.

[35] Aboyade, A. O., Hugo, T. J., Carrier, M., Meyer, E. L., Stahl, R., Knoetze, J. H., and Görgens, J. F., 2011, "Non-isothermal kinetic analysis of the devolatilization of corn cobs and sugar cane bagasse in an inert atmosphere," Thermochimica Acta, 517(1–2), pp. 81-89.

[36] Sahu, S. G., Sarkar, P., Chakraborty, N., and Adak, A. K., 2010, "Thermogravimetric assessment of combustion characteristics of blends of a coal with different biomass chars," Fuel Processing Technology, 91(3), pp. 369-378.

[37] Biagini, E., Lippi, F., Petarca, L., and Tognotti, L., 2002, "Devolatilization rate of biomasses and coal–biomass blends: an experimental investigation," Fuel, 81(8), pp. 1041-1050.

[38] Folgueras, M. B., Díaz, R. M., Xiberta, J., and Prieto, I., 2003, "Thermogravimetric analysis of the co-combustion of coal and sewage sludge," Fuel, 82(15–17), pp. 2051-2055.

[39] Ndaji, F. E., Ellyatt, W. A. T., Malik, A. A., and Thomas, K. M., 1999, "Temperature programmed combustion studies of the co-processing of coal and waste materials," Fuel, 78(3), pp. 301-307.

[40] Otero, M., Díez, C., Calvo, L. F., García, A. I., and Morán, A., 2002, "Analysis of the co-combustion of sewage sludge and coal by TG-MS," Biomass and Bioenergy, 22(4), pp. 319-329.

[41] Lester, E., Gong, M., and Thompson, A., 2007, "A method for source apportionment in biomass/coal blends using thermogravimetric analysis," Journal of Analytical and Applied Pyrolysis, 80(1), pp. 111-117.

[42] Gil, M. V., Casal, D., Pevida, C., Pis, J. J., and Rubiera, F., 2010, "Thermal behaviour and kinetics of coal/biomass blends during co-combustion," Bioresource Technology, 101(14), pp. 5601-5608.

[43] Yanfen, L., and Xiaoqian, M., 2010, "Thermogravimetric analysis of the co-combustion of coal and paper mill sludge," Applied Energy, 87(11), pp. 3526-3532.

[44] Di Nola, G., de Jong, W., and Spliethoff, H., 2010, "TG-FTIR characterization of coal and biomass single fuels and blends under slow heating rate conditions: Partitioning of the fuel-bound nitrogen," Fuel Processing Technology, 91(1), pp. 103-115.

[45] Sadhukhan, A. K., Gupta, P., Goyal, T., and Saha, R. K., 2008, "Modelling of pyrolysis of coal–biomass blends using thermogravimetric analysis," Bioresource Technology, 99(17), pp. 8022-8026.

[46] Sütcü, H., and Pişkin, S., 2011, "The Pyrolytic Characteristics and Kinetics of Agricultural Waste, Bituminous Coal, and Their Blends," Materials and Manufacturing Processes, 26(1), pp. 99-103.

[47] Fermoso, J., Gil, M. V., Pevida, C., Pis, J. J., and Rubiera, F., 2010, "Kinetic models comparison for non-isothermal steam gasification of coal–biomass blend chars," Chemical Engineering Journal, 161(1–2), pp. 276-284.

[48] Werther, J., Saenger, M., Hartge, E. U., Ogada, T., and Siagi, Z., 2000, "Combustion of agricultural residues," Progress in Energy and Combustion Science, 26(1), pp. 1-27.

[49] A.V, B., 1994, "Catalysis in thermal biomass conversion," Applied Catalysis A: General, 116(1–2), pp. 5-47.

[50] Bridgwater, A. V., 2001, Progress in thermochemical biomass conversion, Blackwell Science.

[51] Robinson, A. L., Junker, H., Buckley, S. G., Sclippa, G., and Baxter, L. L., 1998, "Interactions between coal and biomass when cofiring," Symposium (International) on Combustion, 27(1), pp. 1351-1359.

[52] Ayhan, D., 2003, "Sustainable cofiring of biomass with coal," Energy Conversion and Management, 44(9), pp. 1465-1479.

[53] Sami, M., Annamalai, K., and Wooldridge, M., 2001, "Co-firing of coal and biomass fuel blends," Progress in Energy and Combustion Science, 27(2), pp. 171-214.

[54] Kumabe, K., Hanaoka, T., Fujimoto, S., Minowa, T., and Sakanishi, K., 2007, "Co-gasification of woody biomass and coal with air and steam," Fuel, 86(5–6), pp. 684-689.

[55] Lapuerta, M., Hernández, J. J., Pazo, A., and López, J., 2008, "Gasification and co-gasification of biomass wastes: Effect of the biomass origin and the gasifier operating conditions," Fuel Processing Technology, 89(9), pp. 828-837.

[56] Whitty, K. J., Zhang, H. R., and Eddings, E. G., 2008, "Emissions from Syngas Combustion," Combustion Science and Technology, 180(6), pp. 1117-1136.

[57] Richard L, B., 1993, "Electricity from biomass in the United States: Status and future direction," Bioresource Technology, 46(1–2), pp. 86-93.

[58] Peter, M., 2002, "Energy production from biomass (part 2): conversion technologies," Bioresource Technology, 83(1), pp. 47-54.

[59] Ghosh, D., D Sagar, A., and Kishore, V. V. N., 2006, "Scaling up biomass gasifier use: an application-specific approach," Energy Policy, 34(13), pp. 1566-1582.

[60] Thorley, B., Saunby, J. B., Mathur, K. B., and Osberg, G. L., 1959, "An analysis of air and solid flow in a spouted wheat bed," The Canadian Journal of Chemical Engineering, 37(5), pp. 184-192.

[61] Lefroy, G. A., 1969, "The mechanics of spouted beds," Transactions of the Institution of Chemical Engineers, 47(a), p. 120.

[62] Gidaspow, D., and Ettehadieh, B., 1983, "Fluidization in two-dimensional beds with a jet. 2. Hydrodynamic modeling," Industrial & Engineering Chemistry Fundamentals, 22(2), pp. 193-201.

[63] Patrose, B., and Caram, H. S., 1984, "The mechanics of particle motion in a grid jet," Journal Name: AIChE Symp. Ser.; (United States); Journal Volume: 80:241, pp. Medium: X; Size: Pages: 48-56.

[64] Ettehadieh, B., Gidaspow, D., and Lyczkowski, R. W., 1984, "Hydrodynamics of fluidization in a semicircular bed with a jet," Aiche Journal, 30(4), pp. 529-536.

[65] Morgan Iii, M. H., Day, J. Y., and Littman, H., 1985, "Spout voidage distribution, stability and particle circulation rates in spouted beds of coarse particles--I. Theory," Chemical Engineering Science, 40(8), pp. 1367-1377.

[66] Day, J. Y., Morgan Iii, M. H., and Littman, H., 1987, "Measurements of spout voidage distributions, particle velocities and particle circulation rates in spouted beds of coarse particles--II. Experimental verification," Chemical Engineering Science, 42(6), pp. 1461-1470.

[67] van Deemter, J. J., 1967, "The counter-current flow model of a gas-solids fluidized bed," Proceedings of the international symposium on fluidization. Eindhoven, pp. 334-347.

[68] Baeyens, J., and Geldart, D., 1986, "Solids Mixing," Gas Fluidization Technology, D. Geldart, ed., John Wiley & Sons Ltd., pp. 97-122.

[69] van Deemter, J. J., 1985, "Mixing," Fluidization, J.F. Davidson, R.Clift, and D. Harrison, eds., Academic Press, London; Orlando, pp. 331-354.

[70] Merry, J. M. D., 1976, "Fluid and particle entrainment into vertical jets in fluidized beds," Aiche Journal, 22(2), pp. 315-323.

[71] G. Donsi, L. Massimilla, and Colantuoni, L., 1980, "The dispersion of axi-symmetric gas jets in fluidized bed," Fluidization, J.R.Grace, and J. M. Matsen, eds., Plenum Press, New York, pp. 297-304.

[72] Abramovich, G. N., 1963, The theory of turbulent jets, M.I.T. Press (Cambridge, Mass)

[73] Massimilla, L., 1985, "Gas jets in fluidized beds," Fluidization, J.F. Davidson, R.Clift, and D. Harrison, eds., Academic Press, London; Orlando, p. 133.

[74] Gidaspow, D., Lin, C., and Seo, Y. C., 1983, "Fluidization in two-dimensional beds with a jet. 1. Experimental porosity distributions," Industrial & Engineering Chemistry Fundamentals, 22(2), pp. 187-193.

[75] Luo, C. H., Aoki, K., Uemiya, S., and Kojima, T., 1998, "Numerical modeling of a jetting fluidized bed gasifier and the comparison with the experimental data," Fuel Processing Technology, 55(3), pp. 193-218.

[76] Horio, M., Kiyota, H., and Muchi, I., 1980, "PARTICLE MOVEMENT ON A PERFORATED PLATE DISTRIBUTOR OF FLUIDIZED-BED," Journal of Chemical Engineering of Japan, 13(2), pp. 137-142.

[77] Filla, M., Massimilla, L., and Vaccaro, S., 1983, "Gas jets in fluidized beds: The influence of particle size, shape and density on gas and solids entrainment," International Journal of Multiphase Flow, 9(3), pp. 259-267.

[78] Freychet, N., Briens, C. L., Bergougnou, M. A., and Large, J. F., 1989, "A new approach to jet phenomena gas entrainment and recirculation in a bidimensional spouted fluidized bed," The Canadian Journal of Chemical Engineering, 67(2), pp. 191-199.

[79] Kim, S., and Cho, S., 1991, "Particle velocity and circulation rate in liquid spouted beds," Korean Journal of Chemical Engineering, 8(3), pp. 131-136.

[80] Yang, W.-C., and Keairns, D. L., "Solid entrainment rate into gas and gas--solid, two-phase jets in a fluidized bed," Powder Technology, 33(1), pp. 89-94.

[81] Benkrid, A., and Caram, H. S., 1989, "Solid flow in the annular region of a spouted bed," Aiche Journal, 35(8), pp. 1328-1336.

[82] Uemaki, O., and Tsuji, T., 1992, "Particle velocity and solids circulation rate in a jet-spouted bed," The Canadian Journal of Chemical Engineering, 70(5), pp. 925-929.

[83] San José, M. J., Olazar, M., Alvarez, S., Izquierdo, M. A., and Bilbao, J., 1998, "Solid cross-flow into the spout and particle trajectories in conical spouted beds," Chemical Engineering Science, 53(20), pp. 3561-3570.

[84] Olazar, M., San José, M. J., Alvarez, S., Morales, A., and Bilbao, J., 1998, "Measurement of Particle Velocities in Conical Spouted Beds Using an Optical Fiber Probe," Industrial & Engineering Chemistry Research, 37(11), pp. 4520-4527.

[85] Pianarosa, D. L., Freitas, L. A. P., Lim, C. J., Grace, J. R., and Dogan, O. M., 2000, "Voidage and particle velocity profiles in a spout-fluid bed," The Canadian Journal of Chemical Engineering, 78(1), pp. 132-142.

[86] San José, M. J., Alvarez, S., Morales, A., Olazar, M., and Bilbao, J., 2006, "Solid Cross-Flow into the Spout and Particle Trajectories in Conical Spouted Beds Consisting of Solids of Different Density and Shape," Chemical Engineering Research and Design, 84(6), pp. 487-494.

[87] Kececioglu, I., Yang, W.-C., and Keairns, D. L., 1984, "Fate of solids fed pneumatically through a jet into a fluidized bed," Aiche Journal, 30(1), pp. 99-110.

[88] Kececioglu, I., and Keairns, D. L., 1989, "Computation of solid circulation rates in a fluidized bed from tracer particle concentration distributions," The Canadian Journal of Chemical Engineering, 67(2), pp. 290-300.

[89] Hulet, C., Briens, C., Berruti, F., and Chan, E. W., 2008, "Effect of a shroud on entrainment into a submerged jet within a fluidized bed," Chemical Engineering and Processing: Process Intensification, 47(9-10), pp. 1435-1450.

[90] Seo, Y. C., and Gidaspow, D., 1987, "An x-ray-.gamma.-ray method of measurement of binary solids concentrations and voids in fluidized beds," Industrial & Engineering Chemistry Research, 26(8), pp. 1622-1628.

[91] Stein, M., Seville, J. P. K., and Parker, D. J., 1998, "Attrition of porous glass particles in a fluidised bed," Powder Technology, 100(2-3), pp. 242-250.

[92] Yee S, W., 2006, "Particle motion in relatively thin fluidised bed models," Chemical Engineering Science, 61(18), pp. 6234-6238.

[93] Chen, L., and Weinstein, H., 1993, "Shape and extent of the void formed by a horizontal jet in a fluidized bed," Aiche Journal, 39(12), pp. 1901-1909.

[94] Franka, N. P., and Heindel, T. J., 2009, "Local time-averaged gas holdup in a fluidized bed with side air injection using X-ray computed tomography," Powder Technology, 193(1), pp. 69-78.

[95] Link, J., Zeilstra, C., Deen, N., and Kuipers, H., 2004, "Validation of a discrete particle model in a 2D spout-fluid bed using non-intrusive optical measuring techniques," Canadian Journal of Chemical Engineering, 82(1), pp. 30-36.

[96] Link, J. M., Cuypers, L. A., Deen, N. G., and Kuipers, J. A. M., 2005, "Flow regimes in a spout-fluid bed: A combined experimental and simulation study," Chemical Engineering Science, 60(13), pp. 3425-3442.

[97] Laverman, J. A., Roghair, I., Annaland, M. V., and Kuipers, H., 2008, "Investigation into the hydrodynamics of gas-solid fluidized beds using particle image velocimetry coupled with digital image analysis," Canadian Journal of Chemical Engineering, 86(3), pp. 523-535.

[98] van Buijtenen, M. S., Börner, M., Deen, N. G., Heinrich, S., Antonyuk, S., and Kuipers, J. A. M., 2011, "An experimental study of the effect of collision properties on spout fluidized bed dynamics," Powder Technology, 206(1-2), pp. 139-148.

[99] Liu, G. Q., Li, S. Q., Zhao, X. L., and Yao, Q., 2008, "Experimental studies of particle flow dynamics in a two-dimensional spouted bed," Chemical Engineering Science, 63(4), pp. 1131-1141.

[100] Gryczka, O., Heinrich, S., Miteva, V., Deen, N. G., Kuipers, J. A. M., Jacob, M., and Mörl, L., 2008, "Characterization of the pneumatic behavior of a novel spouted bed apparatus with two adjustable gas inlets," Chemical Engineering Science, 63(3), pp. 791-814.

[101] Agarwal, G., Lattimer, B., Ekkad, S., and Vandsburger, U., 2011, "Influence of multiple gas inlet jets on fluidized bed hydrodynamics using Particle Image Velocimetry and Digital Image Analysis," Powder Technology, 214(1), pp. 122-134.

[102] Agarwal, G., Lattimer, B., Ekkad, S., and Vandsburger, U., 2011, "Experimental study on solid circulation in a multiple jet fluidized bed," Aiche Journal, pp. n/a, In Press, DOI: 10.1002/aic.13703.

[103] Chodak, J., 2010, "Pyrolysis and hydrodynamics of fluidized bed media," http://scholar.lib.vt.edu/theses/available/etd-05172010-091509/.

[104] Rees, A. C., Davidson, J. F., Dennis, J. S., Fennell, P. S., Gladden, L. F., Hayhurst, A. N., Mantle, M. D., Muller, C. R., and Sederman, A. J., 2006, "The nature of the flow just above the perforated plate distributor of a gas-fluidised bed, as imaged using magnetic resonance," Chemical Engineering Science, 61(18), pp. 6002-6015.

[105] B. Patrose, and Caram, H. S., 1984, "The mechanics of particle motion in a grid jet," AIChE symposium series; no. 241, G. E. Klinzing, ed., New York, N.Y. : American Institute of Chemical Engineers, San Francisco, pp. 48-56.

[106] Hong, R. Y., Guo, Q. J., Luo, G. H., Zhang, J. Y., and Ding, J., 2003, "On the jet penetration height in fluidized beds with two vertical jets," Powder Technology, 133(1-3), pp. 216-227.

[107] Poletto, M., Bai, R., and Joseph, D. D., 1995, "Propagation of voidage waves in a two-dimensional liquid-fluidized bed," International Journal of Multiphase Flow, 21(2), pp. 223-239.

[108] Boerefijn, R., and Ghadiri, M., 1998, "High speed video image analysis of flow of fine particles in fluidized bed jets," Advanced Powder Technology, 9(3), pp. 229-243.

[109] Merry, J. M. D., 1975, "PENETRATION OF VERTICAL JETS INTO FLUIDIZED-BEDS," Aiche Journal, 21(3), pp. 507-510.

[110] Müller, C. R., Holland, D. J., Davidson, J. F., Dennis, J. S., Gladden, L. F., Hayhurst, A. N., Mantle, M. D., and Sederman, A. J., 2009, "Geometrical and hydrodynamical study of gas jets in packed and fluidized beds using magnetic resonance," The Canadian Journal of Chemical Engineering, 87(4), pp. 517-525.

[111] Heffels, C., Willemse, A., and Scarlett, B., 1996, "Possibilities of near backward light scattering for characterizing dense particle systems," Powder Technology, 86(1), pp. 127-135.

[112] Wornat, M. J., Hurt, R. H., Yang, N. Y. C., and Headley, T. J., 1995, "Structural and compositional transformations of biomass chars during combustion," Combustion and Flame, 100(1–2), pp. 131-143.

[113] Biagini, E., Narducci, P., and Tognotti, L., 2008, "Size and structural characterization of lignin-cellulosic fuels after the rapid devolatilization," Fuel, 87(2), pp. 177-186.

[114] C, v. A., 2007, "Automated mineralogical analysis of coal and ash products – Challenges and requirements," Minerals Engineering, 20(5), pp. 496-505.

[115] Zolin, A., Jensen, A., Jensen, P. A., Frandsen, F., and Dam-Johansen, K., 2001, "The Influence of Inorganic Materials on the Thermal Deactivation of Fuel Chars," Energy & Fuels, 15(5), pp. 1110-1122.

[116] Sonobe, T., and Worasuwannarak, N., 2008, "Kinetic analyses of biomass pyrolysis using the distributed activation energy model," Fuel, 87(3), pp. 414-421.

[117] Janse, A. M. C., Westerhout, R. W. J., and Prins, W., 2000, "Modelling of flash pyrolysis of a single wood particle," Chemical Engineering and Processing: Process Intensification, 39(3), pp. 239-252.

[118] Manyà, J. J., Velo, E., and Puigjaner, L., 2002, "Kinetics of Biomass Pyrolysis: a Reformulated Three-Parallel-Reactions Model," Industrial & Engineering Chemistry Research, 42(3), pp. 434-441.

[119] Teng, H., and Wei, Y.-C., 1998, "Thermogravimetric Studies on the Kinetics of Rice Hull Pyrolysis and the Influence of Water Treatment," Industrial & Engineering Chemistry Research, 37(10), pp. 3806-3811.

[120] Várhegyi, G., Grønli, M. G., and Di Blasi, C., 2004, "Effects of Sample Origin, Extraction, and Hot-Water Washing on the Devolatilization Kinetics of Chestnut Wood," Industrial & Engineering Chemistry Research, 43(10), pp. 2356-2367.

[121] Giuntoli, J., Arvelakis, S., Spliethoff, H., de Jong, W., and Verkooijen, A. H. M., 2009, "Quantitative and Kinetic Thermogravimetric Fourier Transform Infrared (TG-FTIR) Study of

Pyrolysis of Agricultural Residues: Influence of Different Pretreatments," Energy & Fuels, 23(11), pp. 5695-5706.

[122] Hurt, R. H., Davis, K. A., Yang, N. Y. C., Headley, T. J., and Mitchell, G. D., 1995, "Residual carbon from pulverized-coal-fired boilers. 2. Morphology and physicochemical properties," Fuel, 74(9), pp. 1297-1306.

[123] Ravindra K, A., 1985, "On the use of the arrhenius equation to describe cellulose and wood pyrolysis," Thermochimica Acta, 91(0), pp. 343-349.

[124] D.J, B., 1982, "The questionable use of the Arrhenius equation to describe cellulose and wood pyrolysis," Thermochimica Acta, 54(3), pp. 377-379.

[125] Biagini, E., Fantei, A., and Tognotti, L., 2008, "Effect of the heating rate on the devolatilization of biomass residues," Thermochimica Acta, 472(1–2), pp. 55-63.

[126] Kansa, E. J., Perlee, H. E., and Chaiken, R. F., 1977, "Mathematical model of wood pyrolysis including internal forced convection," Combustion and Flame, 29(0), pp. 311-324.

[127] Colomba, D. B., 1993, "Modeling and simulation of combustion processes of charring and non-charring solid fuels," Progress in Energy and Combustion Science, 19(1), pp. 71-104.

[128] Pyle, D. L., and Zaror, C. A., 1984, "Heat transfer and kinetics in the low temperature pyrolysis of solids," Chemical Engineering Science, 39(1), pp. 147-158.

[129] Agrawal, R. K., 1992, "Analysis of non-isothermal reaction kinetics:: Part 1. Simple reactions," Thermochimica Acta, 203, p. 93.

[130] Alan K, B., 2000, "Computational aspects of kinetic analysis.: Part D: The ICTAC kinetics project — multi-thermal–history model-fitting methods and their relation to isoconversional methods," Thermochimica Acta, 355(1–2), pp. 165-170.

[131] B, R., 2000, "Computational aspects of kinetic analysis.: Part E: The ICTAC Kinetics Project—numerical techniques and kinetics of solid state processes," Thermochimica Acta, 355(1–2), pp. 171-180.

[132] Brown, M. E., Maciejewski, M., Vyazovkin, S., Nomen, R., Sempere, J., Burnham, A., Opfermann, J., Strey, R., Anderson, H. L., Kemmler, A., Keuleers, R., Janssens, J., Desseyn, H. O., Li, C.-R., Tang, T. B., Roduit, B., Malek, J., and Mitsuhashi, T., 2000, "Computational aspects of kinetic analysis: Part A: The ICTAC kinetics project-data, methods and results," Thermochimica Acta, 355(1–2), pp. 125-143.

[133] Marek, M., 2000, "Computational aspects of kinetic analysis.: Part B: The ICTAC Kinetics Project — the decomposition kinetics of calcium carbonate revisited, or some tips on survival in the kinetic minefield," Thermochimica Acta, 355(1–2), pp. 145-154.

[134] Sergey, V., 2000, "Computational aspects of kinetic analysis.: Part C. The ICTAC Kinetics Project — the light at the end of the tunnel?," Thermochimica Acta, 355(1–2), pp. 155-163.

[135] Opfermann, J. R., Kaisersberger, E., and Flammersheim, H. J., 2002, "Model-free analysis of thermoanalytical data-advantages and limitations," Thermochimica Acta, 391(1–2), pp. 119-127.

[136] Opfermann, J., 2000, "Kinetic Analysis Using Multivariate Non-linear Regression. I. Basic concepts," Journal of Thermal Analysis and Calorimetry, 60(2), pp. 641-658.

[137] Völker, S., and Rieckmann, T., 2002, "Thermokinetic investigation of cellulose pyrolysis — impact of initial and final mass on kinetic results," Journal of Analytical and Applied Pyrolysis, 62(2), pp. 165-177.

[138] Becidan, M., Várhegyi, G., Hustad, J. E., and Skreiberg, Ø., 2007, "Thermal Decomposition of Biomass Wastes. A Kinetic Study," Industrial & Engineering Chemistry Research, 46(8), pp. 2428-2437.

[139] Li, Z., Liu, C., Chen, Z., Qian, J., Zhao, W., and Zhu, Q., 2009, "Analysis of coals and biomass pyrolysis using the distributed activation energy model," Bioresource Technology, 100(2), pp. 948-952.

[140] Li, C., and Suzuki, K., 2009, "Kinetic analyses of biomass tar pyrolysis using the distributed activation energy model by TG/DTA technique," Journal of Thermal Analysis and Calorimetry, 98(1), pp. 261-266.

[141] Navarro, M. V., Murillo, R., Mastral, A. M., Puy, N., and Bartroli, J., 2009, "Application of the distributed activation energy model to biomass and biomass constituents devolatilization," AIChE Journal, 55(10), pp. 2700-2715.

[142] Várhegyi, G. b., Bobály, B. z., Jakab, E., and Chen, H., 2010, "Thermogravimetric Study of Biomass Pyrolysis Kinetics. A Distributed Activation Energy Model with Prediction Tests," Energy & Fuels, 25(1), pp. 24-32.

[143] Shen, D. K., Gu, S., Jin, B., and Fang, M. X., 2011, "Thermal degradation mechanisms of wood under inert and oxidative environments using DAEM methods," Bioresource Technology, 102(2), pp. 2047-2052.

[144] Cai, J., Jin, C., Yang, S., and Chen, Y., 2011, "Logistic distributed activation energy model – Part 1: Derivation and numerical parametric study," Bioresource Technology, 102(2), pp. 1556-1561.

[145] Mészáros, E., Várhegyi, G., Jakab, E., and Marosvölgyi, B., 2004, "Thermogravimetric and Reaction Kinetic Analysis of Biomass Samples from an Energy Plantation," Energy & Fuels, 18(2), pp. 497-507.

[146] Radmanesh, R., Courbariaux, Y., Chaouki, J., and Guy, C., 2006, "A unified lumped approach in kinetic modeling of biomass pyrolysis," Fuel, 85(9), pp. 1211-1220.

[147] Saddawi, A., Jones, J. M., Williams, A., and Wójtowicz, M. A., 2009, "Kinetics of the Thermal Decomposition of Biomass," Energy & Fuels, 24(2), pp. 1274-1282.

[148] Milosavljevic, I., and Suuberg, E. M., 1995, "Cellulose Thermal Decomposition Kinetics: Global Mass Loss Kinetics," Industrial & Engineering Chemistry Research, 34(4), pp. 1081-1091.

[149] A.F, R., 1970, "A review of kinetics data for the pyrolysis of wood and related substances," Combustion and Flame, 14(2), pp. 261-272.

[150] Seo, D. K., Park, S. S., Hwang, J., and Yu, T.-U., 2010, "Study of the pyrolysis of biomass using thermo-gravimetric analysis (TGA) and concentration measurements of the evolved species," Journal of Analytical and Applied Pyrolysis, 89(1), pp. 66-73.

[151] F, S., 1968, "Pyrolysis and Combustion of Cellulosic Materials," Advances in Carbohydrate Chemistry, L. W. Melville, and R. S. Tipson, eds., Academic Press, pp. 419-474.

[152] Kanury, A. M., and Blackshear, P. L., 1970, "Some Considerations Pertaining to the Problem of Wood-Burning," Combustion Science and Technology, 1(5), pp. 339-356.

[153] Biagini, E., and Tognotti, L., 2006, "Comparison of Devolatilization/Char Oxidation and Direct Oxidation of Solid Fuels at Low Heating Rate," Energy & Fuels, 20(3), pp. 986-992.

[154] Ulloa, C. A., Gordon, A. L., and García, X. A., 2009, "Thermogravimetric study of interactions in the pyrolysis of blends of coal with radiata pine sawdust," Fuel Processing Technology, 90(4), pp. 583-590.

[155] Agarwal, G., and Lattimer, B., 2012, "Method for measuring the standard heat of decomposition of materials," Thermochimica Acta, 545(0), pp. 34-47.

[156] Koufopanos, C. A., Lucchesi, A., and Maschio, G., 1989, "Kinetic modelling of the pyrolysis of biomass and biomass components," The Canadian Journal of Chemical Engineering, 67(1), pp. 75-84.

[157] Lyon, R. E., and Walters, R. N., 2004, "Pyrolysis combustion flow calorimetry," Journal of Analytical and Applied Pyrolysis, 71(1), pp. 27-46.

[158] International, A., 2011, "Standard Test Method for Determining Flammability Characteristics of Plastics and Other Solid Materials Using Microscale Combustion Calorimetry," ASTM Standard D7309 - 11West Conshohocken, PA

[159] Rath, J., Wolfinger, M. G., Steiner, G., Krammer, G., Barontini, F., and Cozzani, V., 2003, "Heat of wood pyrolysis," Fuel, 82(1), pp. 81-91.

[160] Strezov, V., Lucas, J., and Strezov, L., 2000, "Quantifying the heats of coal devolatilization," Metallurgical and Materials Transactions B, 31(5), pp. 1125-1131.

[161] Strezov, V., Moghtaderi, B., and Lucas, J. A., 2004, "Computational calorimetric investigation of the reactions during thermal conversion of wood biomass," Biomass and Bioenergy, 27(5), pp. 459-465.

[162] Yu, B., Till, V., and Thomas, K., 2007, "Modeling of thermo-physical properties for FRP composites under elevated and high temperature," Composites Science and Technology, 67(15-16), pp. 3098-3109.

[163] Henderson, J. B., and Emmerich, W. D., 1991, "Measurement of specific heat and energetic characterization of materials up to high temperatures," Journal of Thermal Analysis and Calorimetry, 37(8), pp. 1979-1985.

[164] Henderson, J. B., Wiebelt, J. A., Tant, M. R., and Moore, G. R., 1982, "A method for the determination of the specific heat and heat of decomposition of composite materials," Thermochimica Acta, 57(2), pp. 161-171.

[165] Frederick, W. J., and Mentzer, C. C., 1975, "Determination of heats of volatilization for polymers by differential scanning calorimetry," Journal of Applied Polymer Science, 19(7), pp. 1799-1804.

[166] Stoliarov, S. I., and Walters, R. N., 2008, "Determination of the heats of gasification of polymers using differential scanning calorimetry," Polymer Degradation and Stability, 93(2), pp. 422-427.

[167] Lyon, R. E., 2000, "Heat release kinetics," Fire and Materials, 24(4), pp. 179-186.

[168] Yun, Y., and Suuberg, E. M., 1993, "New applications of differential scanning calorimetry and solvent swelling for studies of coal structure: Prepyrolysis structural relaxation," Fuel, 72(8), pp. 1245-1254.

[169] Manara, P., and Zabaniotou, A., 2013, "Co-pyrolysis of biodiesel-derived glycerol with Greek lignite: A laboratory study," Journal of Analytical and Applied Pyrolysis, 100(0), pp. 166-172.

[170] Muthuraman, M., Namioka, T., and Yoshikawa, K., 2010, "A comparative study on co-combustion performance of municipal solid waste and Indonesian coal with high ash Indian coal: A thermogravimetric analysis," Fuel Processing Technology, 91(5), pp. 550-558.

[171] Heikkinen, J. M., Hordijk, J. C., de Jong, W., and Spliethoff, H., 2004, "Thermogravimetry as a tool to classify waste components to be used for energy generation," Journal of Analytical and Applied Pyrolysis, 71(2), pp. 883-900.

[172] Sharma, S., and Ghoshal, A. K., 2010, "Study of kinetics of co-pyrolysis of coal and waste LDPE blends under argon atmosphere," Fuel, 89(12), pp. 3943-3951.

[173] Loulou, T., Salvador, S., and Dirion, J. L., 2003, "Determination of Reaction Parameters for Cardboard Thermal Degradation Using Experimental Data," Chemical Engineering Research and Design, 81(9), pp. 1265-1270.

[174] Sheng, C., and Azevedo, J. L. T., 2005, "Estimating the higher heating value of biomass fuels from basic analysis data," Biomass and Bioenergy, 28(5), pp. 499-507.

[175] Demirbaş, A., 1997, "Calculation of higher heating values of biomass fuels," Fuel, 76(5), pp. 431-434.

[176] Parikh, J., Channiwala, S. A., and Ghosal, G. K., 2005, "A correlation for calculating HHV from proximate analysis of solid fuels," Fuel, 84(5), pp. 487-494.

[177] Raveendran, K., and Ganesh, A., 1996, "Heating value of biomass and biomass pyrolysis products," Fuel, 75(15), pp. 1715-1720.

[178] Naik, S., Goud, V. V., Rout, P. K., Jacobson, K., and Dalai, A. K., 2010, "Characterization of Canadian biomass for alternative renewable biofuel," Renewable Energy, 35(8), pp. 1624-1631.

[179] Barneto, A. n. G. a., Carmona, J. A., Alfonso, J. E. M. n., and Ferrer, J. A. C., 2009, "Use of Thermogravimetry/Mass Spectrometry Analysis to Explain the Origin of Volatiles Produced during Biomass Pyrolysis," Industrial & Engineering Chemistry Research, 48(15), pp. 7430-7436.

[180] Agarwal, G., Lattimer, B. Y., and Liu, G., "Pyrolysis and combustion characterization of coal-biomass fuel blends," Proc. Proceedings of the ASME 2013 Power Conference.

[181] Jenkins, B. M., Baxter, L. L., Miles Jr, T. R., and Miles, T. R., 1998, "Combustion properties of biomass," Fuel Processing Technology, 54(1–3), pp. 17-46.

[182] Gil, M. V., Oulego, P., Casal, M. D., Pevida, C., Pis, J. J., and Rubiera, F., 2010, "Mechanical durability and combustion characteristics of pellets from biomass blends," Bioresource Technology, 101(22), pp. 8859-8867.

[183] Peksa, M., Dolzan, P., Grassi, A., Heinimö, J., Junginger, H., Ranta, T.-M., and Walter, A., 2007, "Global Wood Pellets Markets and Industry: Policy Drivers, Market Status and Raw Material Potential."

[184] Samuelsson, R., Thyrel, M., Sjöström, M., and Lestander, T. A., 2009, "Effect of biomaterial characteristics on pelletizing properties and biofuel pellet quality," Fuel Processing Technology, 90(9), pp. 1129-1134.

[185] Larsson, S. H., Thyrel, M., Geladi, P., and Lestander, T. A., 2008, "High quality biofuel pellet production from pre-compacted low density raw materials," Bioresource Technology, 99(15), pp. 7176-7182.

[186] Spliethoff, H., and Hein, K. R. G., 1998, "Effect of co-combustion of biomass on emissions in pulverized fuel furnaces," Fuel Processing Technology, 54(1–3), pp. 189-205.

[187] Bratton, R., Luttrell, G., Kasindorf, H., McGraw, G., and Robbins, R., 2010, "Evaluation of a Novel Fine Coal Dry Cleaning Process at Greenfields Coal Company," International Journal of Coal Preparation & Utilization, 30(2-5), pp. 145-153.

[188] Luttrell, G. H., Kohmuench, J. N., and Yoon, R.-H., 2000, "An evaluation of coal preparation technologies for controlling trace element emissions," Fuel Processing Technology, 65–66(0), pp. 407-422.

[189] Bratton, R., Luttrell, G., Kasindorf, H., Christensen, P., and McAllister, M., 2010, "Evaluation of a Novel Fine Coal Briquetting Process at GreenFields Coal Company," 16th, International Coal Preparation Congress, Society for Mining, Metallurgy and Exploration Inc. , Littleton, Co. , pp. 904-911

[190] Wang, C., Wang, F., Yang, Q., and Liang, R., 2009, "Thermogravimetric studies of the behavior of wheat straw with added coal during combustion," Biomass and Bioenergy, 33(1), pp. 50-56.

[191] Rhén, C., Öhman, M., Gref, R., and Wästerlund, I., 2007, "Effect of raw material composition in woody biomass pellets on combustion characteristics," Biomass and Bioenergy, 31(1), pp. 66-72.

[192] Nussbaumer, T., 2003, "Combustion and Co-combustion of Biomass: Fundamentals, Technologies, and Primary Measures for Emission Reduction†," Energy & Fuels, 17(6), pp. 1510-1521.

[193] Vamvuka, D., and Sfakiotakis, S., 2011, "Combustion behaviour of biomass fuels and their blends with lignite," Thermochimica Acta, 526(1–2), pp. 192-199.

[194] Zhang, Y., McKechnie, J., Cormier, D., Lyng, R., Mabee, W., Ogino, A., and MacLean, H. L., 2009, "Life Cycle Emissions and Cost of Producing Electricity from Coal, Natural Gas, and Wood Pellets in Ontario, Canada," Environmental Science & Technology, 44(1), pp. 538-544.

[195] Dohm D, E., Luttrell H, G., Karmis E, M., and Ripepi S, N., "Optimization of binderless briquetting coal-biomass mixtures," Proc. 6th International Conference on Clean Coal Technologies.

[196] International, A., 2013, "Standard Test Method for Heat and Visible Smoke Release Rates for Materials and Products Using an Oxygen Consumption Calorimeter," ASTM Standard E1354, 2013West Conshohocken, PA

[197] Sun, C. L., and Koziński, J. A., 2000, "Ignition behaviour of pulp and paper combustible wastes," Fuel, 79(13), pp. 1587-1593.

[198] Huang, Y. F., Kuan, W. H., Chiueh, P. T., and Lo, S. L., 2011, "Pyrolysis of biomass by thermal analysis–mass spectrometry (TA–MS)," Bioresource Technology, 102(3), pp. 3527-3534.

[199] Worasuwannarak, N., Sonobe, T., and Tanthapanichakoon, W., 2007, "Pyrolysis behaviors of rice straw, rice husk, and corncob by TG-MS technique," Journal of Analytical and Applied Pyrolysis, 78(2), pp. 265-271.

[200] Branca, C., Giudicianni, P., and Di Blasi, C., 2003, "GC/MS Characterization of Liquids Generated from Low-Temperature Pyrolysis of Wood," Industrial & Engineering Chemistry Research, 42(14), pp. 3190-3202.

[201] Staggs, J. E. J., 2005, "Savitzky–Golay smoothing and numerical differentiation of cone calorimeter mass data," Fire Safety Journal, 40(6), pp. 493-505.

[202] Turns, S. R., 1996, An introduction to combustion, McGraw-Hill New York.